Numerical Models for Scoring Failures of Flexible Metal to Metal Face Seals

by

Jinchul Hong

B.S., Mechanical Engineering
Korea Advanced Institute of Science and Technology, 1998

S.M., Mechanical Engineering
Massachusetts Institute of Technology, 2000

Submitted to the Department of Mechanical Engineering
in Partial Fulfillment of the Requirements for
the Degree of Doctor of Philosophy

at the

Massachusetts Institute of Technology

February 2005

Signature of Author .....
Department of Mechanical engineering
September, 2004

Certified by .....
Douglas P. Hart
Associate Professor, Department of Mechanical Engineering
Committee Chair

Certified by .....
Tian Tian
Lecturer, Department of Mechanical Engineering
Thesis Supervisor

Accepted by .....
Lallit Anand
Chairman, Committee on Graduate Studies

Numerical Models for Scoring Failures of Flexible Metal to Metal Face Seals

by

Jinchul Hong

Submitted to the Department of Mechanical Engineering
on September, 2004 in Partial Fulfillment of the Requirements for
the Degree of Doctor of Philosophy

ABSTRACT

The flexible metal to metal face seals (FMMFS) has unique features including much more flexibility in the circumferential direction than in the radial direction, identical rotating and stationary seals, and a loading mechanism using elastomeric rings. This thesis work is the first attempt to explain scoring failures of this unique type of mechanical face seal.

Numerical models and new scoring failure criteria were developed to explain different scoring failures of the FMMFS. The numerical models consider interactions among seal surface deflections, lubrication in the sealing band and thermal effects simultaneously. The numerical models were validated from comparisons with experiments and applied to scoring failure tests. The new scoring failure criterion successfully predicted the likelihood of scoring failures for each seal pair at given loads and speeds.

From in-depth analysis of the seal pairs with low and high scoring failure speeds, it has been shown that discontinuous contact patterns can increase scoring resistance of the seal pair. These discontinuous contact patterns are created by irregular surface profiles of the sealing band. Irregular surface profiles can decrease high temperature regions by reducing superposition of temperatures and thermal conduction resistance, and finally delay scoring failures.

Thesis Supervisor:

Tian Tian
Lecturer, Department of Mechanical Engineering

Douglas P. Hart
Associate Professor, Department of Mechanical Engineering

ACKNOWLEDGEMENT

When I think of my past 6 years at MIT, I remember some difficult times. However, I'm surprised that I had much more thankful and precious moments and people around me.

First, I would like to thank my advisor, Dr. Tian Tian for his guidance through last 4 years of doctoral study. I learned a lot from him not only solving difficult engineering problems, but also balancing between personal and professional life. I want to express him my deepest appreciation and respects. I also would like to thank Prof. Douglas P. Hart. He has been my academic advisor since when I first came to MIT. I'm appreciated with his kindness and advice during my stay at MIT. I want to show my sincere thanks to Prof. Ain A. Sonin for being my committee member and serving more than 20 years as graduate officer of our department. Furthermore, I would like to thank to Prof. Borivoje Mikic for accepting part of the committee and teaching me advanced heat transfer course.

I gratefully acknowledge good memories in the Sloan Automotive Laboratory. Special thanks to Morgan Andreae for his careful corrections in this thesis. I also would like to thank Liang Liu, Yong Li, Mohammad Rassuli, Yeunwoo Cho, Fiona McClure, Dongkun Lee, Jungik Kim, Adam Vokac, Ertan Yilmaz, Oscar Lopez and Yuetao Zhang. I have been happy to be a member of KGSAME, Korean Graduate Student Association in Mechanical Engineering. I will remember their supports and concerns through my stays at MIT. Especially, I want to thank for following Korean students at MIT for making my life more enjoyable: Taekyun Chung, Junmo Kim, Seongmoo Heo, Seonghwan Cho, Heejin Lee and Jaehyuk Choi. Outside MIT, I was blessed to be in a community of First Korean Church in Cambridge. Especially, I would like to thank every member of our bible study group, CJN2, for all their prayers and precious moments we had.

I would like to express most sincere thanks to my family from my heart. Their support and concerns always have been the source of strength during my past years. I was blessed to have Heeyoung as my lovely wife. Through all the highs and lows since we met together, she always have shown unchanging supports and love to me. I thank my precious daughter, Seeun, for giving me wonderful experience to become her farther. I also would like to thank for my parents for their love, sacrifice and prayers.

Finally, I thank God for all his guidance through my life. Since I meet Jesus Christ personally in my life one year ago, my life has been never the same as before. More than anything, I want to love God above all things and my neighbors as myself. What a pleasant surprise… everything happened in my life had its meaning and purpose.

1 Introduction

1.1 Motivation

Mechanical face seals aim to minimize lubricant leakage and to delay the wear of mechanical parts through proper lubrication. These seals are used in lubricating and sealing various mechanical parts including lubricated joints, axles of trucks and other rotating housings.

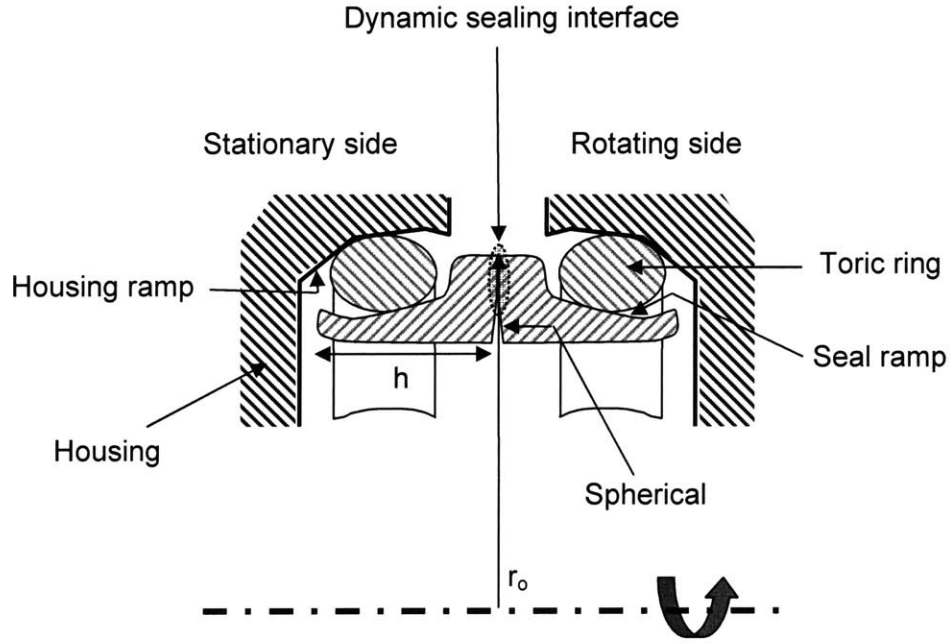

Figure 1.1 Radial cross sections of the FMMFS

The seal that is investigated in this thesis is a unique type of the mechanical face seal (see Figure 1.1). The seal has a small cross section area with a large diameter. The length of the inside seal surface (h) is at least one order of magnitude shorter than the outside diameter of the seal ring ($2*r_o$). The outside diameter varies from several hundreds millimeters to several meters. Because of this geometric feature, the seal is much more flexible in the circumferential direction than in the radial direction. Although the outside diameter of the seal changes, the dimension of the radial cross section does

not change significantly. Thus, the seal becomes more flexible along the circumference as the outside diameter increases. Because of the flexibility along the circumference, and because the seal materials are made of metal, the seal is called the flexible metal to metal face seal (FMMFS).

The design of the FMMFS is simple, although the operation mechanism is still unknown. As shown in Figure 1.1, two seals are compressed against each other and form a dynamic sealing interface where a thin lubricant film exists. During operation, one seal rotates while the other seal is stationary. The sealing interface prevents leakage of inside oil and contamination by outside environment sources such as soils and dirt.

It is noteworthy that a pair of the FMMFS consists of two identical seals while a pair of common mechanical face seals consists of two different materials and design. In addition, loading mechanisms use rubber rings to transfer axial loads and allow the two seals to close tightly with self-alignments during rotations. The FMMFS is known to be specially designed for unique applications [1].

Two kinds of failure modes, excessive leakage and scoring failure, exist for the FMMFS. Excessive leakage represents continuous leakage of an unacceptable amount of the lubricant. For scoring failures, the seal pair works well without any visible signs of leakage until friction and temperatures start to increase suddenly. Then, the seal pair fails due to excessive friction and temperature rise accompanied with damages to the sealing interface.

Figure 1.2 shows an example of failure speeds with corresponding initial axial loading for leakage and scoring failure tests. Failure speeds are defined as linear speeds in the middle of the sealing band. Measured failure speeds and loads are normalized by 10 m/s and 433 N, respectively in Figure 1.2. Differences in initial loads and failure speeds are significant, especially in failure speeds. These results mean that performances of FMMFS are inconsistent although all seal pairs used in failure tests satisfy manufacturing specifications.

Early failure of the FMMFS means not only replacements of seals themselves, but also a loss in productivity in the seal application due to down time and the cost of labor. Thus, improvements in seal design for extended seal lives would bring tremendous economic benefits.

For improvements in seal design, understanding of fundamental operating and failure mechanisms of the FMMFS is essential. However, there has been little understanding of operating and failure mechanisms of this type of mechanical face seal with flexibility and self-alignment along the circumference. The first objective of this thesis work is to investigate operating mechanisms such as lubricant transport, heat transfer process, and contact patterns by developing numerical models. An appropriate scoring failure criterion using results of the numerical models could be developed. This criterion would be useful for evaluating scoring resistant design of the FMMFS. Finding such a scoring failure criterion is the second main objective of the thesis work. Better understanding of seal operation and an appropriate failure criterion will lead to better seal design and performance.

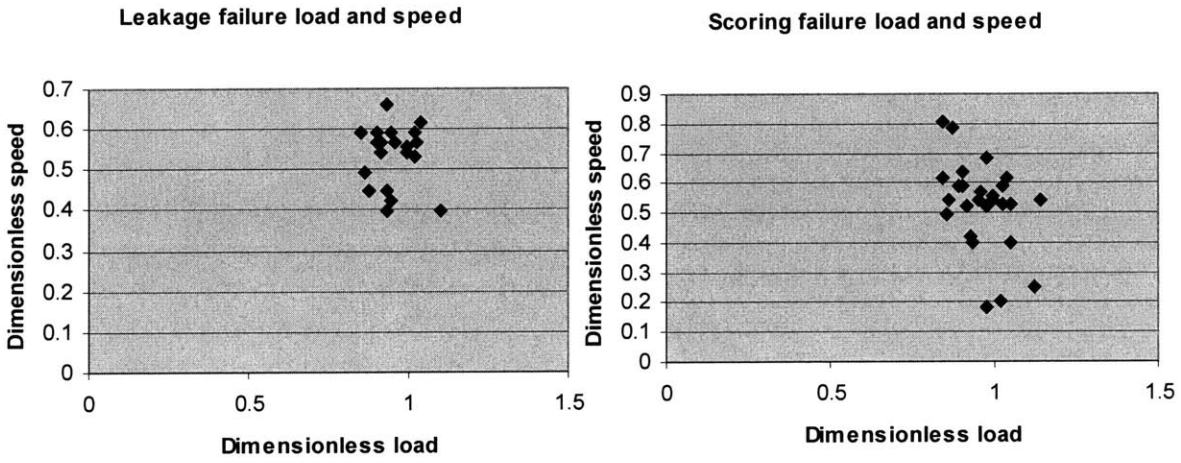

Figure 1.2 Two failure modes - leakage and scoring failure

1.2 Backgrounds

1.2.1 The geometry of the metal to metal face seal

Recall that two FMMFS are pressed against each other as shown in Figure 1.1. The surface geometry of the sealing interface where actual sealing occurs strongly affects the seal performance. The surface geometry, on a macro and a micro scale of the sealing surface, will be described in this section.

The surface geometry of the sealing interface on the macro scale is shown in Figure 1.3. The overview of the sealing interface is shown in Figure 1.3 (a)[1], while a radial seal profile is shown in Figure 1.3 (b). Figure 1.3 (a) shows circumferential variations in the surface heights of the sealing band. These variations, called waviness, are a consequence of many different manufacturing processes such as uneven lapping process.

A sealing band where actual sealing occurs consists of two parts as shown in Figure 1.3 (b): a transition and a flat part. The width of the sealing band is usually a few millimeters. The region inside the sealing band is called a spherical region. The transition part connects the flat part and the spherical region with a curvature. The ends of the inside and the outside of the sealing band are defined as the inside (ID) and the outside diameter (OD), respectively.

Figure 1.4 shows the micro geometry of surface roughness on the sealing band. Each lateral dimension of the small area in Figure 1.4 (b) is several tens of microns, while the root mean square of the surface roughness is on the order of 0.1 microns. The polishing process of the sealing band is responsible for the longitudinal surface roughness in the circumferential direction.

It is evident that all of the geometrical features on the macro and micro scale play an important role in the performances of the FMMFS.

[1] Note that the radial position of the sealing band is normalized by the outer radius.

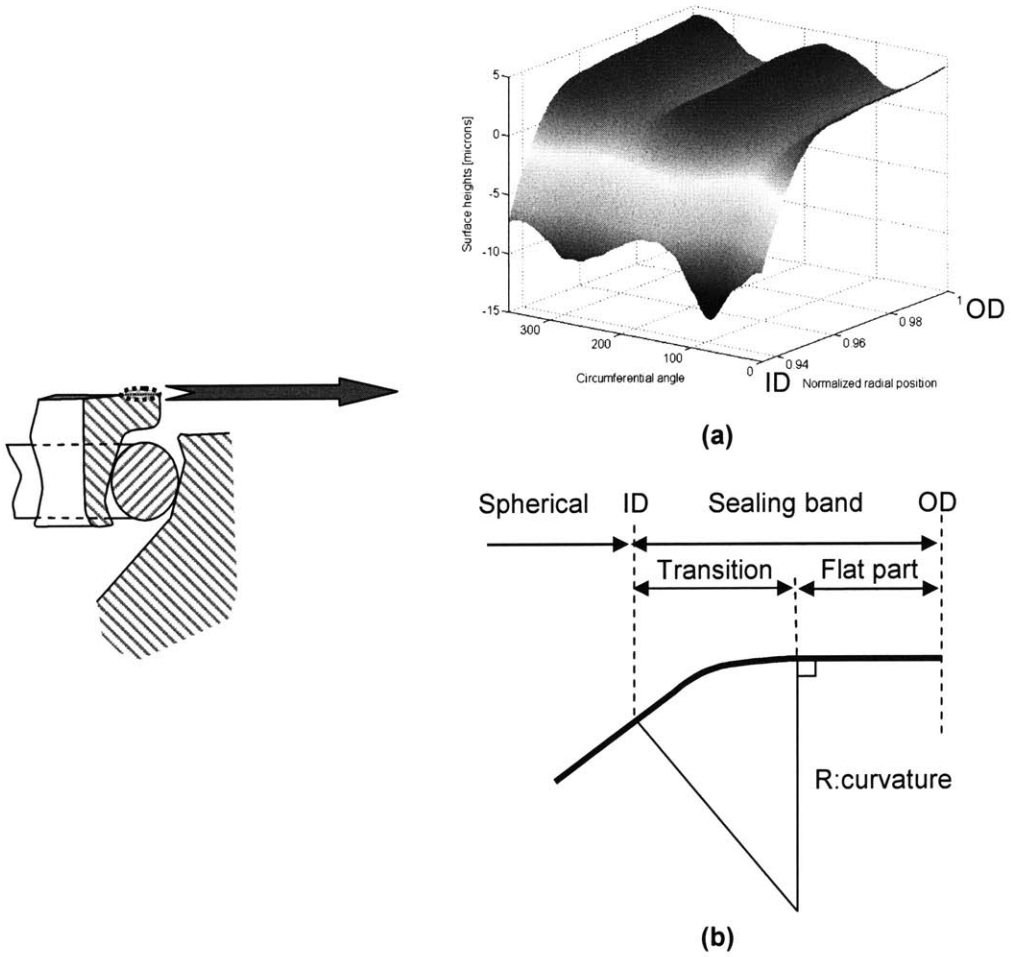

Figure 1.3 (a) The overview and (b) the radial cross section of the sealing band

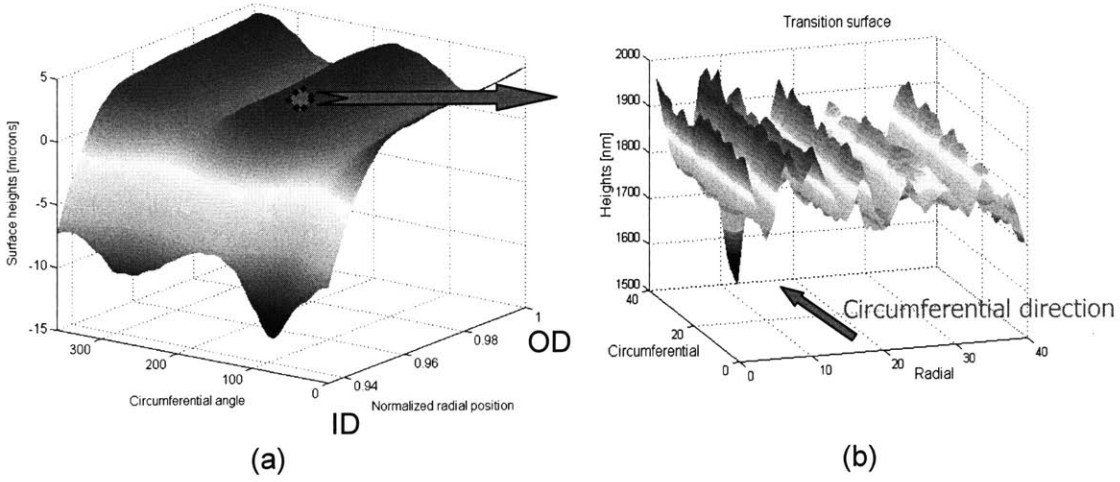

Figure 1.4 Surface geometry on micro scale in the sealing band

1.2.2 Scoring mechanisms

Scoring failure is a sudden and severe mode of lubrication failure manifested by unstable friction and temperatures [2]. It is known that asperities on nascent surfaces can be easily bonded together. Bonding between the nascent metal surfaces is so strong that it can lead to instant seizures. Several mechanisms related to the exposure of the nascent surfaces can contribute to scoring failures, although their contributions and interactions are still unknown. These mechanisms are the catalytic decomposition of entrained lubricant, the removal of protective oxide layers on contacting surfaces, and the desorption of an adsorbed lubricant film.

The first scoring failure mechanism is called the catalytic decomposition of the entrained lubricant. When a hydrodynamic lubrication film breaks down, asperity contacts between seal surfaces lead to wear of the seal surfaces. Nascent surfaces are exposed by this mechanical wear process. It is known that nascent surfaces catalyze decomposition reactions of organic compounds in the lubricant film and degradation of the lubricant occurs [3]. If sufficient nascent surfaces are exposed, the rate of the degradation of the lubricant exceeds the replenishment rate of fresh oil. With the degradation of the lubricant, the lubricant can not sustain a high shear rate anymore. The loss of lubrication capacity by the catalytic decomposition can lead to the increased exposure of the nascent surfaces due to more asperity contacts, and finally to scoring failure.

The second scoring failure mechanism is the removal of protective oxide layers on the contacting surfaces. The presence of oxygen in lubricant oil or the atmosphere can lead to the formation of oxide layers on seal surfaces. It is known that these protective oxide layers provide the first line of defense against mechanical wear by asperity contacts and delay the exposure of nascent surfaces [4]. Removal of the protective oxide layers can lead to the exposure of the nascent surfaces which initiates scoring failures. The oxide formation and removal rates depend on temperatures. Above some critical temperatures, the oxide removal rate would exceed the oxide formation rate and so initiates scoring failures.

The third scoring failure mechanism, the desorption of an adsorbed lubricant film also is also related to the exposure of nascent asperities. Even after the breakdown of a hydrodynamic lubrication film, the adsorbed thin lubricant film prevents direct contacts between the nascent asperities. This thin film forms a low shear interface between the opposing asperities in the mixed or boundary lubrication regime. When the desorption rate exceeds the adsorption rate of the thin lubricant film on the surfaces, the nascent surfaces are exposed and direct contacts between the asperities lead to scoring failures. The desorption rate is most sensitive to temperatures, but also depends on pressures, sliding speeds, and oil composition [5].

All of these scoring mechanisms are interdependent and interactions are still unknown. However, it is clear that temperatures play an important role in scoring failures. First, the breakdown of a hydrodynamic lubrication film usually occurs at high temperatures. The viscosity of the oil decreases exponentially with the increase of temperatures. As the viscosity decreases, a hydrodynamic lift force is reduced. With a decrease of the hydrodynamic lift force, the oil film thickness reduces until asperity contacts occur to sustain the required lift force. Secondly, the catalytic decomposition of the entrained lubricant highly depends on temperatures. Reaction rate between nascent surfaces and the lubricant increases with temperatures and results in faster decomposition activities. Lastly, the desorption rate of the lubricant film also are accelerated with the increase of temperatures in the similar way. Therefore, many researchers have attempted to predict scoring failures with temperature distributions from thermal models.

1.2.3 Thermal models

Contact temperatures of two sliding surfaces are the sum of nominal surface temperatures and local temperatures [6]. Figure 1.5 shows the steady state temperature profile along the line AA' across a contacting area. Note that the magnified view near the contacting interface shows that real contact areas are much smaller than nominal contact areas. For steady state conduction, a temperature drop within the contacting body is linear except near the contacting interface. This linear temperature profile is called the nominal temperature. Near the contacting interface, a sudden non-linear temperature drop occurs

due to dramatic decrease of contacting areas. This non-linear temperature change is called the local temperature rise. Boundary conditions on macro scales such as convection to surrounding flows are important for the calculations of the nominal temperature distribution. On the contrary, the local temperature distribution is not affected by such large scale boundary conditions.

Several numerical models to calculate the nominal temperature distribution in the mechanical face seals considering the viscosity dependence of oil on temperature have been developed. Such numerical models are called thermo-hydrodynamic models. Knoll developed a three-dimensional numerical simulation using finite element method which accounted for waviness effects [7]. Person used a finite difference method considering the effects of waviness and misalignment [8]. Tournerie included the heat transfer through both a stationary and a rotating seal while Person's model considered heat transfer through the rotating seal only [9].

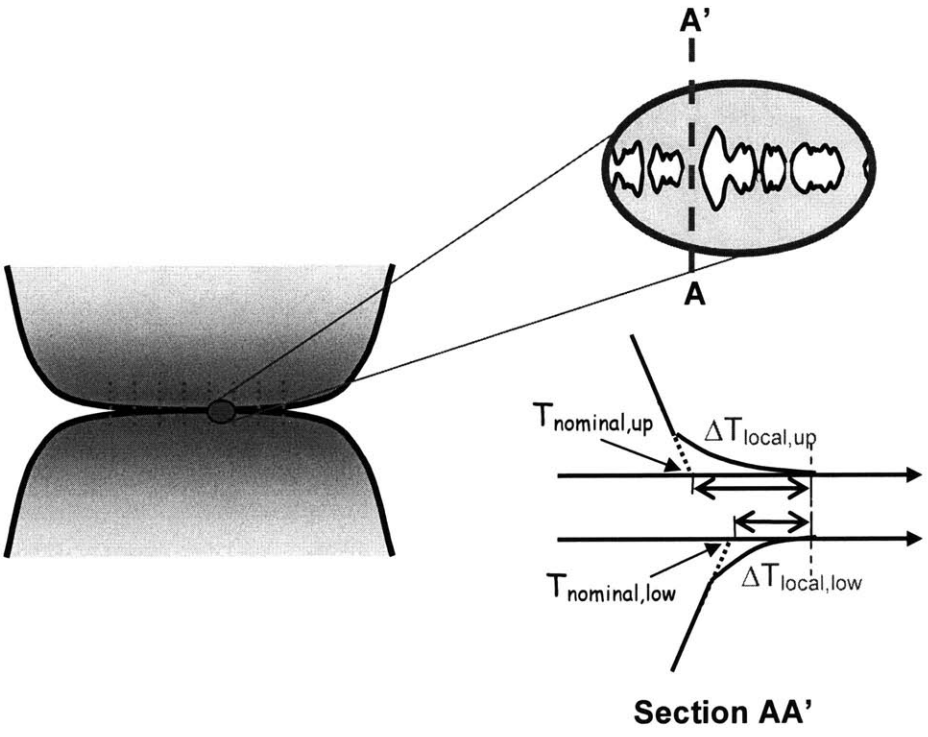

Figure 1.5 Nominal surface and local temperature rise

These published numerical models [7, 8, 9] of the nominal temperature distribution assume that mechanical face seals operate in the hydrodynamic lubrication regime without asperity contacts and cavitation effects. However, it will be shown that the metal to metal face seal operates in the boundary lubrication regime with negligible hydrodynamic effects in terms of load support (see section 3.4.2). Cavitation effects are important for the calculations of the frictional heat flux distribution in the sealing band (see section 2.5.4). Thus, those models are not suitable for this particular application, FMMFS.

The local temperature rise can be estimated using the solution of a semi-infinite body subjected to a single or multiple heat sources. Blok's classical model calculated the surface temperatures of a semi-infinite body subject to a single concentrated heat source [10]. Jaeger formulated the surface temperature distribution of a semi-infinite body due to a moving heat source of various shape [11]. Ling and Pu considered random changes of heat source distribution in space and time [12]. Tian and Kennedy studied the analytical solution of the surface temperatures for different moving heat sources over the entire Peclet number range [13]. Lai extended Ling and Pu's approach to consider more realistic changes of heat flux distribution using computer- generated rough surfaces and asperity contact models [14]. Liang and Cheng developed the temperature simulation of real sliding rough surfaces in a mixed lubricated condition with more efficient numerical methods [15].

The above thermal models [10-15] calculate the local temperature rise only. These models neglect the nominal temperature rise assuming the local temperature rise is much higher. This assumption is valid when the nominal temperature rise is relatively low due to the large heat capacity of sliding bodies and relatively low total friction. However, this assumption is questionable in many sliding bodies with a finite thickness under moderate or severe friction. For the FMMFS, the nominal temperature rise is comparable with the local temperature rise (see appendix A). Thus, both temperature rises need to be considered together for the scoring failures of the FMMFS. The nominal temperature distribution of the FMMFS system is directly calculated from the thermal model. On the other hand, the effects of the local temperature rise are taken into account by considering

the heat flux magnitudes at the high nominal temperature regions. For details, see section 4.3.

1.2.4 Scoring failure criteria

Two criteria, the critical temperature and the frictional power intensity, have been widely used for prediction of scoring failures [2]. The critical temperature criterion by Blok postulates that scoring starts when the total surface temperature reaches the critical temperature. According to Blok's postulation, this critical temperature is constant for each combination of the lubricant and sliding materials, and it is independent of other variables. This postulation was supported by some experiments [16]. However, many workers have found the critical temperature varies in a complicated manner with many parameters such as sliding speeds, total load and oil additives [5].

It should be noted that the total critical temperature is the sum of the nominal and local temperature rise. When the local temperature is comparable to the nominal temperature, the thermal model needs to resolve large scale heat transfer as well as small scale heat transfer. The macro scale thermal model calculates the nominal temperature distribution with macro scale boundary conditions. Then, areas near contact surfaces are divided into small sliding surfaces to calculate the local temperature rise with micro scale heat transfer models. The size of the small rough surface is usually several orders of magnitude smaller than the total contact areas. Thus, the calculations of the total temperatures require tremendous computation costs due to a large number of divided rough surfaces. This is why most of contact temperature models neglect the nominal temperatures. However, recall that the nominal temperature distribution can not be neglected for the FMMFS. Thus, it is clear that the critical temperature criterion based on the local temperature rise only is not directly applicable to scoring failures of the FMMFS.

The other widely used criterion is the frictional power intensity (FPI). This criterion postulates that scuffing occurs when frictional heat exceeds a certain critical value. The FPI is defined as dividing total frictional heat input by total contact areas [17]. The critical frictional power intensity also varies with many variables. Some studies show that the FPI criterion predicts scoring failures better than the critical temperature criterion [2].

However, the FPI criterion only considers the amount of frictional heat. Different temperature distribution is possible for the same total frictional heat with different heat flux distribution. Distribution of heat flux is proved to be important and finally can lead to different scoring failure conditions. These effects will be discussed in detail in chapter 4.

In summary, a more appropriate criterion needs to be developed for FMMFS. The new scoring failure criterion needs to consider both the nominal and the local temperatures because they are comparable in operating conditions.

1.3 Thesis outline

In this chapter, the objectives of the project and the background of previous scoring models have been described. The FMMFS has unique features such as the flexibility along the circumference, same material for the rotating and the stationary seal, geometry variations on macro and micro scale, and a loading mechanism using the rubber ring. For typical ranges of operating loads and speeds, the seal operates in the boundary lubrication regime, where asperity contacts occur at the sealing interface. It also has been shown that the nominal temperatures are comparable with the local temperature rise under typical operating conditions. Thus, both temperature effects on scoring failures need to be considered. Considering these unique features and operating conditions, it is necessary to develop new types of numerical models and scoring criteria.

The next chapter will describe details in developments of the current numerical models. The numerical models consist of three major programs: the 3D contact model, the cavitation model, and the 3D thermal model. Each program will be explained with its inputs, outputs and assumptions. These numerical models are validated by comparisons with experimental results in chapter 3. Then, the numerical models are applied to scoring failure tests with the new scoring failure criterion in the next chapter. Results show good prediction abilities for scoring failure tests. Physical explanations for difference in scoring failure speeds are also addressed in the same chapter. Conclusions of thesis work and suggestions for future works will follow in chapter 5.

2 Numerical models

2.1 Structure of numerical models

The difficulty in modeling of mechanical face seals is due to coupled interactions of various mechanisms. When two seals are pressed against each other, sealing surfaces deflect and generate the axial force from asperity contacts. When the seal operates, the axial force is supported by the asperity contacts of sealing surfaces and the hydrodynamic forces generated by lubricant film at the sealing interface. These hydrodynamic forces deflect sealing surfaces. At the same time, a significant amount of frictional heat is generated from asperity contacts and viscous shearing of the oil film. Frictional heat leads to thermal distortion of seal faces, which affects the asperity contacts and the hydrodynamic force at the sealing interface. Furthermore, the increase of temperatures from friction in the oil film generally reduces not only the friction due to shearing of the oil film, but also the hydrodynamic force. This decrease of the hydrodynamic force results in more contacts of the small asperities on the seal faces to support the deficient loads.

As a result, the numerical model of mechanical face seal needs to couple lubrication, heat transfer and surface deflections. These models need to be solved iteratively to consider mutual interactions. However, solving all three models simultaneously requires tremendous computation costs. In addition, all interactions, such as deflections of the surfaces and heat transfer process, are unsteady with rotations for the pair of the FMMFS because it consists of two identical seals. These unsteady effects add computation costs significantly.

Difficulties due to expensive computation costs can be overcome by simplifying assumptions for each numerical model. At the same time, numerical models should capture underlying physics with these assumptions. This chapter will describe each numerical model in detail with corresponding assumptions and their validations. The flow chart of numerical models is shown in Figure 2.1 below.

The most important simplification comes from the circumferential flexibility of FMMFS. The FMMFS is much more flexible in the circumferential direction than in the

radial direction. Therefore, initial waviness along the circumference can be flattened out above a certain axial loads. Because initial waviness is the main source of generating hydrodynamic pressures of the lubricant, effects of hydrodynamic pressures on the total axial lift force would be negligible. In this case, the interactions between solid deflections and hydrodynamic pressures of the lubricant can be decoupled and greatly reduces computation costs. Figure 2.1 shows such decoupling of the iteration loop between the 3D contact model and the cavitation model.

The program starts from reading surface profiles, which can be imported from measurements data. Alternatively, artificial surface profiles can be generated by defining some important geometric parameters, such as a waviness, a concavity, and a radius of curvature. For more details in generating artificial surface profiles, see appendix B.

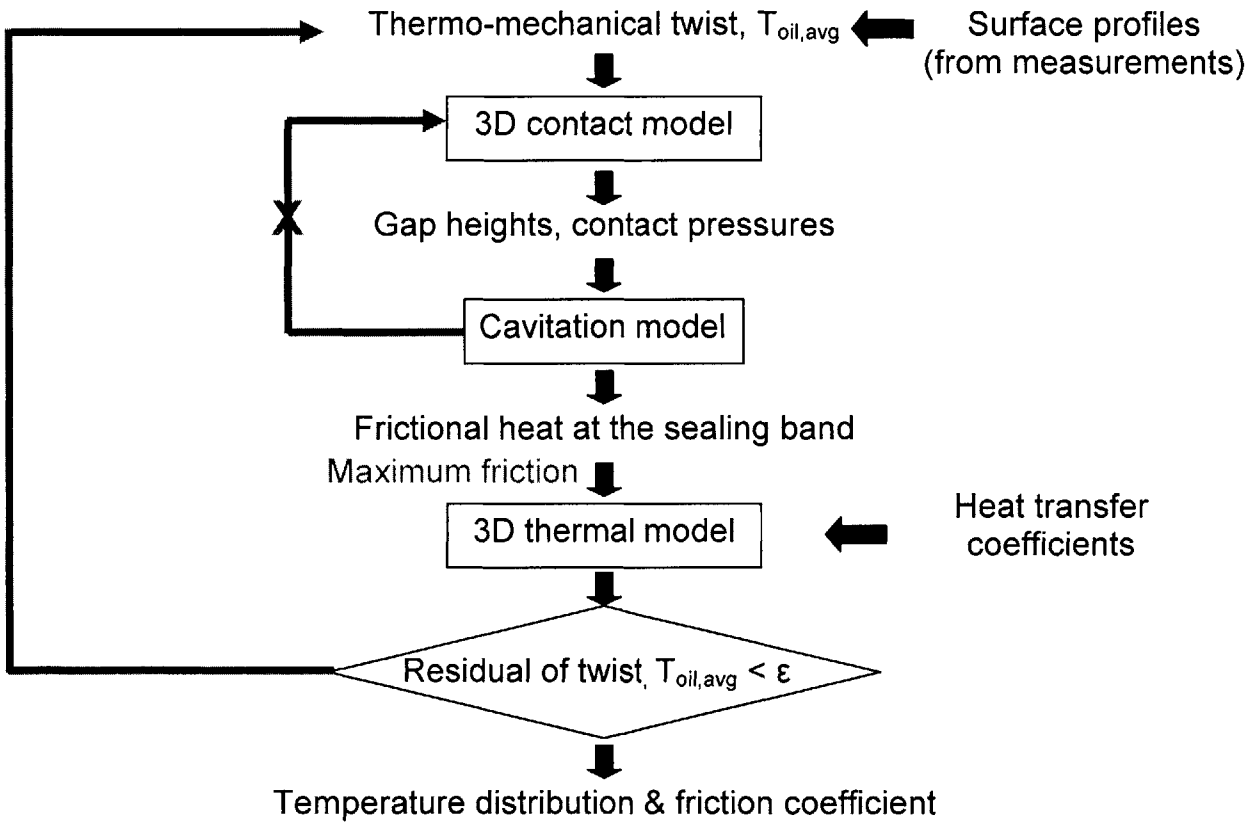

Figure 2.1 The flow chart of numerical models

After importing surface profiles of the one seal pair, the 3D contact model generates final gap heights and contact pressures under a certain axial load. Final gap heights are used for the cavitation model to calculate cavitation regions and the average density of oil in the sealing band. With contact pressures and oil distributions, frictional heat flux on the sealing band and friction coefficients can be calculated.

Friction coefficients would vary with rotation due to changes in contact areas, contact pressures, and oil distribution. For temperature calculations, the program captures the moment when maximum friction occurs. With frictional heat distribution at the moment of maximum friction, the 3D thermal model calculates temperature distribution of the oil film, the rotating seal, and the stationary seal. Note that the 3D thermal model calculates upper bound temperature distribution.

All of above procedures are repeated until solid deflections, oil pressure, and temperature distribution converge.

2.2 *Importing surface profiles*

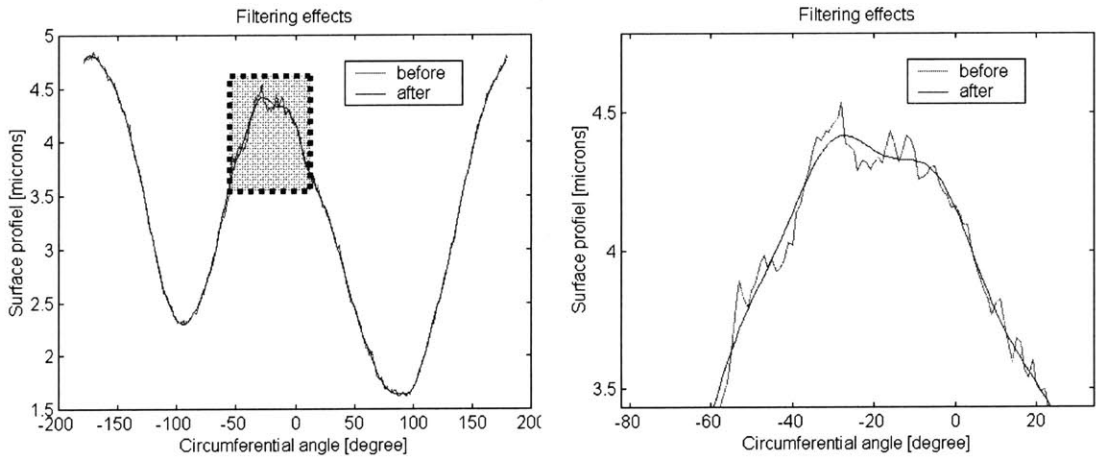

Figure 2.2 Surface profiles before and after filtering (right: magnified view)

As the first step, surface profiles of the seal pair needs to be imported to the program. These surface profiles are measured using an interferometer from Zygo, Inc. The interferometer generates surface data files of the sealing band in the rectangular

coordinates. Transformation of data points to the cylindrical coordinates is necessary for the future use in the program. Moreover, the optical measurement has the following limitations: high frequency profiles and limited measurement capacity.

One of the measured surface profiles along the circumference is shown in Figure 2.2 . The same profile is also plotted after filtering out the high frequency components. Note that high frequency profiles have the same order of magnitude as the surface roughness, and thus may represent the variations of the surface roughness. To obtain the surface profiles on macro scale, high frequency profiles are filtered. The cut-off frequency for filtering is 15.

The optical surface measurement can not measure large variations of surface heights. When the surface heights change abruptly in the transition regions with a curvature, the optical measurements can not generate surface data files. Inside the transition regions, gap heights change rapidly with the curvature (see Figure 2.3) and can not be measured. However, it will be shown that these regions near ID are important for calculations of contact areas, especially under a high load and speed (see section 4.5.2). Thus, the extrapolation from the transition regions to the inside diameter is necessary to include inside areas of the sealing band into calculation domains.

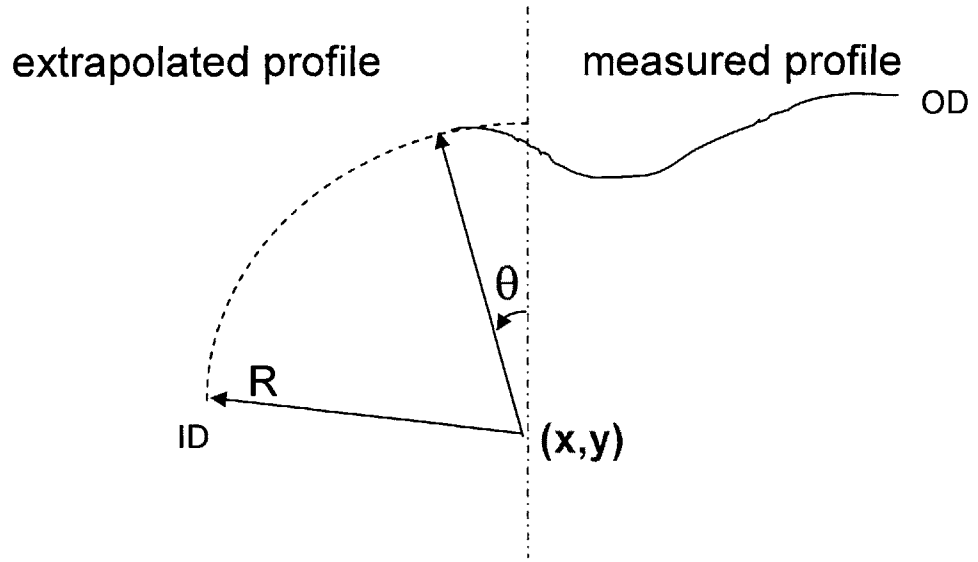

Figure 2.3 Extrapolation of the radial profile

It is found that the curvatures are almost constant along the circumference. Assuming constant curvature along the circumference, three unknown variables need to be solved: the coordinates of the curvature center (x,y), and the start of the curvature (θ). These three variables can be solved using the continuity of the surface profile and its slope. Figure 2.4 shows the surface profile before (left) and after (right) the extrapolation. This extrapolation process is repeated for each measured radial profile along the whole circumference.

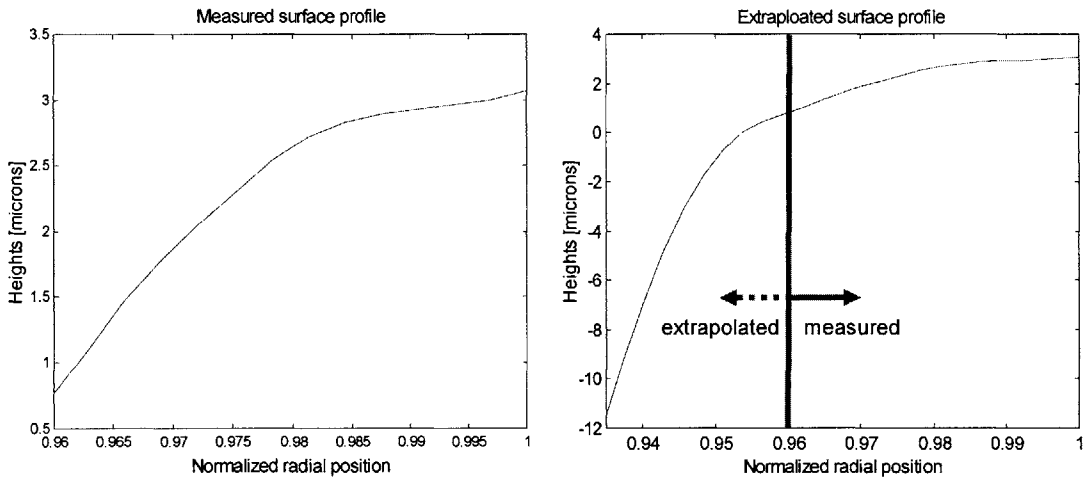

Figure 2.4 Surface profile measured (left) and after (right) extrapolation

2.3 The 3D contact model

2.3.1 Assumptions for the 3D contact model

An important simplification is made for the 3D contact model as mentioned earlier. It is found that the FMMFS is much more flexible in the circumferential direction than in the radial direction. To verify this simplification, we calculated deflections of the seal surface under uniform loadings of 1 N/mm^2, which is less than a typical supporting load. Each curve in Figure 2.5 represents the deflections at ID or OD of the seal surface

[2] 'N/mm' means the force per unit length along the circumference of the sealing band. For instance, total axial force is about 300N for the FMMFS with 92 mm in diameter.

when sinusoidal forces with the total magnitude of 1 N/mm are imposed on the ID or OD, respectively. Because the amplitude of a waviness of the FMMFS is usually less than few microns, deflection is one order of magnitude larger than the amplitude of waviness. This means seal surfaces are so flexible in the circumferential direction that circumferential surface variations due to the initial waviness do not matter after deformation even under relatively low loading condition. When the initial waviness and rigidity in the circumferential direction can be neglected, only surface profiles and rigidity in the radial direction are important. Then, it is necessary to solve the 2D contact problem in each radial cross section instead of solving the 3D contact problem.

The other assumption is that the total axial force is supported solely by the asperity contacts of the seal surfaces. This assumption implies that the hydrodynamic force generated from the lubricant film is negligible compared to the total axial force. In other words, the FMMFS operate in the boundary lubrication regime where hydrodynamic effects are negligible. With negligible hydrodynamic effects, the deflections of seal surfaces are independent of the lubricant pressures at the sealing interface. Thus, the interactions between the deflections of seal surfaces and the lubricant pressures can be decoupled and reduce computation costs significantly. This assumption is validated by comparisons with experiments over the wide range of axial loads (see section 3.4.2).

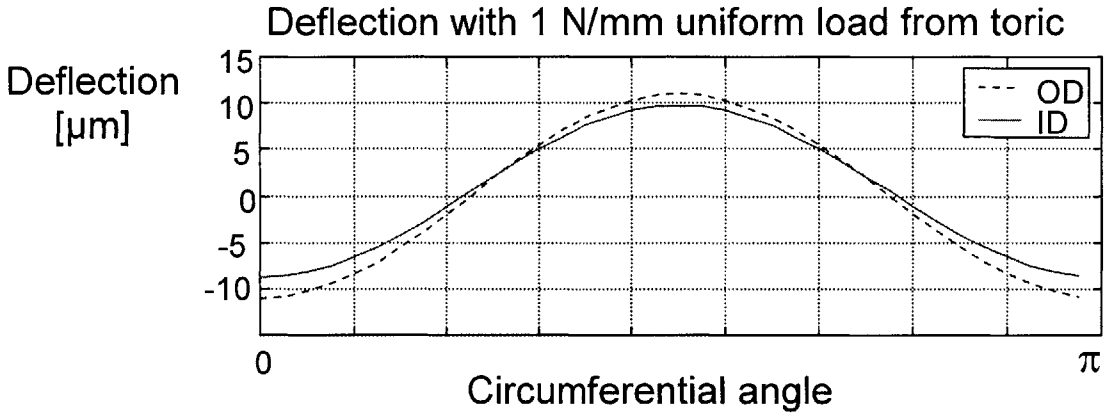

Figure 2.5 Deflections of the seal surface under 1 N/mm load

In addition, it was also assumed that loading from toric rings are uniformly distributed. This assumption implies that each radial cross section supports the same amount of distributed load.

2.3.2 Calculations of twist angles

For each radial cross section, the contact model requires surface profiles of the seal pair and twist angles as inputs (see Figure 2.6). Twist angles (θ_{sta} for the stationary seal and θ_{rot} for the rotating seal) in Figure 2.6 are due to pressure loadings from toric rings and thermal expansions from temperature gradients. These twist angles will be referred as mechanical twist and thermal twist angles, respectively. Note that contact areas tend to move radially inward with increasing twist angles.

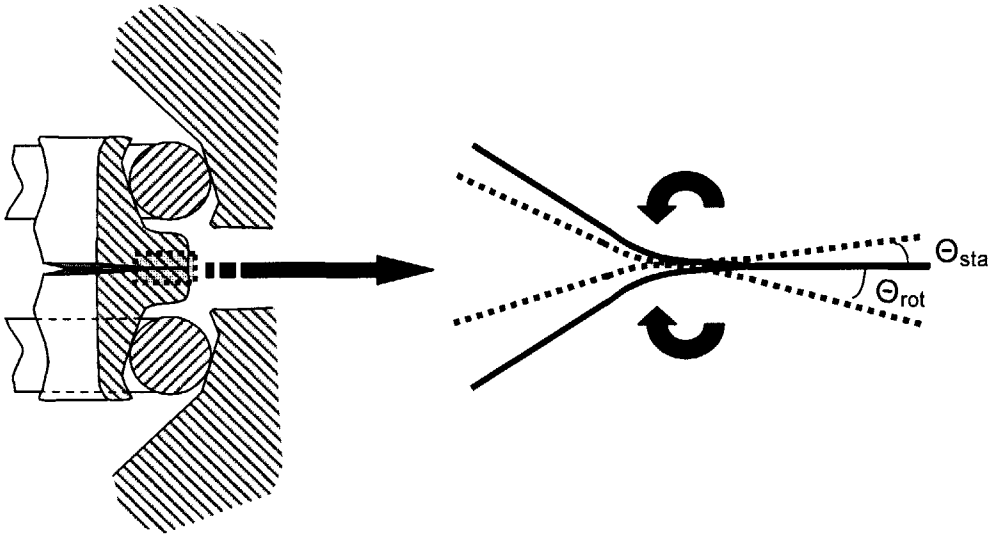

Figure 2.6 Mechanical and thermal twist angles

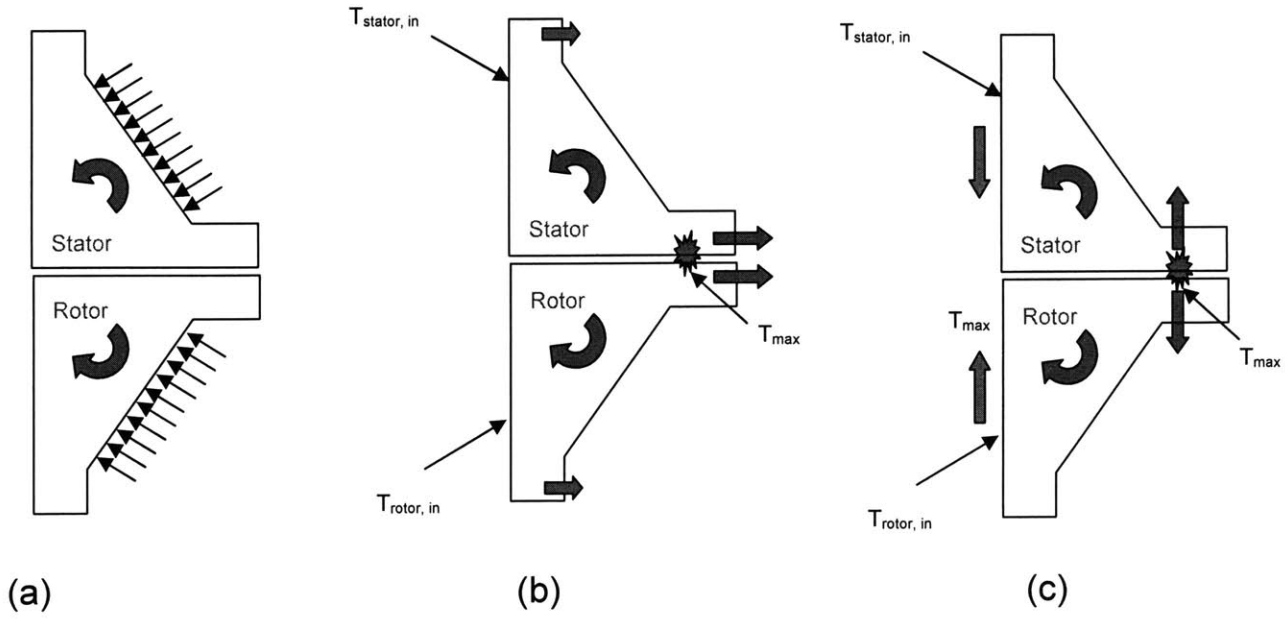

Figure 2.7 Mechanical (a) vs. thermal twist angles (b) and (c)

Twist mechanisms are shown in Figure 2.7. Pressure loading from toric rings imposes torques on each seal to rotate, and results in mechanical twist angles (see Figure 2.7 (a)). On the other hand, temperature differences lead to different thermal expansions near the sealing interface and inside seal surfaces. Temperatures decrease from the sealing interface to inside seal surfaces, where convection to oil flow occurs. These temperature differences induce more radial (Figure 2.7 (b)) and axial (Figure 2.7 (c)) thermal expansions near the sealing interface and result in rotation of the seal pair.

Each kind of twist angles are calculated from the axis-symmetric solid contact model. The commercial finite element package, ADINA, is used for twist angle calculations. The solid contact model requires temperature distributions to consider thermal expansion effects. The axis-symmetric thermal model is used for temperature calculations. This thermal model will be explained in more detail for heat transfer coefficients calculations (see section 3.2.3).

The axis-symmetric solid contact model is shown in Figure 2.8. Uniform pressure loading from toric rings is imposed as shown in the left side of Figure 2.8. Meshes are refined until band plots of contact pressures are continuous along boundaries of elements. Each band in Figure 2.8 represents 10% of maximum contact pressures. Continuous band

plots across the element boundary show satisfactory local equilibrium between elements [18].

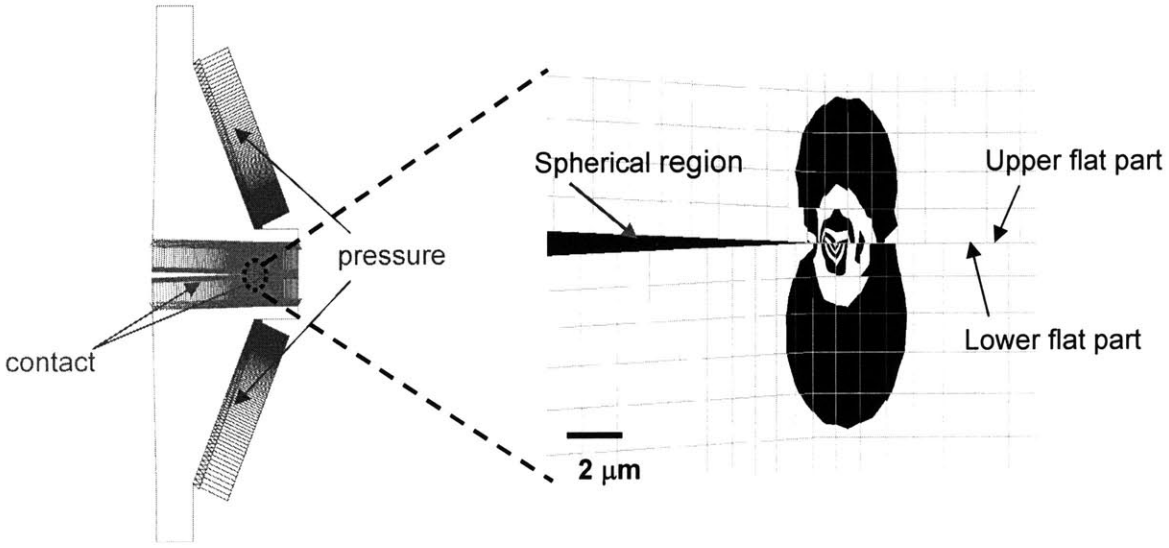

Figure 2.8 The finite element contact model and the band plot of contact pressures

Mechanical twist angles are obtained from the 2D contact model when temperatures of the seal pair are the same at room temperatures. Normalized axial loadings are increased from 0.5 to 2.5 by 0.5. Then, mechanical twist angles are linearly fitted to the corresponding axial loading.

Thermal twist angles are obtained in the same way, while total heat flux inputs in the axis-symmetric thermal model are 70, 94, 114, 136, 160 and 300W. At the same time, normalized axial loadings change from 0.5 to 2.5 by 0.5, then maintained 2.5 for 300W. From twist angles calculations, mechanical twist angles are subtracted to exclude the effects of pressure loading.

To calculate characteristic temperature differences, maximum temperatures at the sealing interface and averaged temperatures at inside seal surfaces are selected. Then, each thermal twist angle of the stationary and the rotating seal should be proportional to T_{max}-$T_{stator,in}$ and T_{max}-$T_{rotor,in}$, respectively (see Figure 2.7). Thermal twist angles are lineary fitted to the sum of these temperature differences, $dT_{tot} = (T_{\max} - T_{sta,in}) + (T_{\max} - T_{rot,in})$.

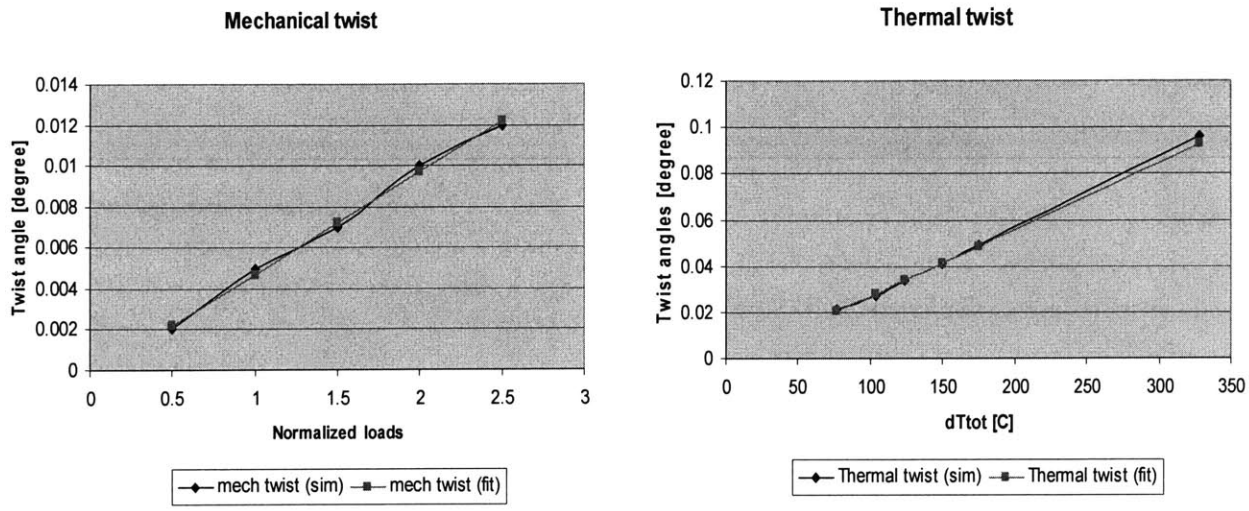

Figure 2.9 Mechanical (left) and thermal (right) twist angles and linear fittings

Mechanical and thermal twist angles with linear fittings are shown in Figure 2.9. Note that mechanical twist angles are much smaller than those from thermal twist, especially for high total frictional heat input. In addition, linear fitting seems to be precise enough to calculate twist angles over a wide range of pressure loadings and frictional heat flux input. The linear-fitting equations for mechanical and thermal twist angles are expressed as,

$$Mechanical\ \ twist\ angles\ [Degree\ ] = 5.0 * 10^{-3} * Loads\ [N / mm\ ] - 3.0 * 10^{-4},$$

$$Thermal\ \ twist\ angles\ [Degree\ ] = 2.874 * 10^{-4} * \Delta T_{tot} - 1.739 * 10^{-3},$$

$$\text{where } dT_{tot} = (T_{\max} - T_{sta,in}) + (T_{\max} - T_{rot,in}).$$

With the axial loadings and temperature distributions, the program can calculate total twist angles, which are the sum of mechanical and thermal twist angles. Note that these total twist angles generally vary along the circumference due to circumferential variations in T_{max}.

2.3.3 Finding the minimum film thickness

In reality, real contacts occur at a small fraction of nominal contact areas due to a surface roughness. The surface roughness also creates finite gap heights among real contact areas. As a result, averaged gap heights are not zero in nominal contact areas. An equation which relates the average load to the average gap between two rough surfaces is developed by Lee and Cheng [19]. This equation is valid for contacting surfaces with a purely longitudinal roughness. It is known that FMMFS has approximately longitudinal roughness generated from the manufacturing process. Therefore, Lee and Cheng's equation was adapted to describe the relation between asperity contact pressure and gap heights. The non-dimensional equation of the averaged load and the average gap height is as follows:

$$\frac{4 p_{avg} L}{E' \sigma \pi} = e^{f(H)} \qquad (2.1)$$

where

$$f(H) = 3.01002 - 3.04431\,H - 1.54827\,H^2 + 2.56951\,H^3 - 0.920266\,H^4 \qquad (2.2)$$

p_{avg}: average contact pressure,

L: the profile segment length,

E`: equivalent Young's modulus $E' = 2\left[\frac{1-\nu_1^2}{E_1} + \frac{1-\nu_2^2}{E_2}\right]^{-1}$,

ν: Poisson's ratio,

σ: composite rms roughness,

H: surface heights normalized by σ.

Once average gap heights are known, average contact pressures can be calculated, and vice versa. In addition to twist angles, the 3D contact model adjusts a minimum

height to satisfy the required load for each radial cross section as shown in Figure 2.10. These procedures are repeated for all radial cross sections along the circumference. Finally, the 3D contact model calculates final gap heights and contact pressures for given load and speed.

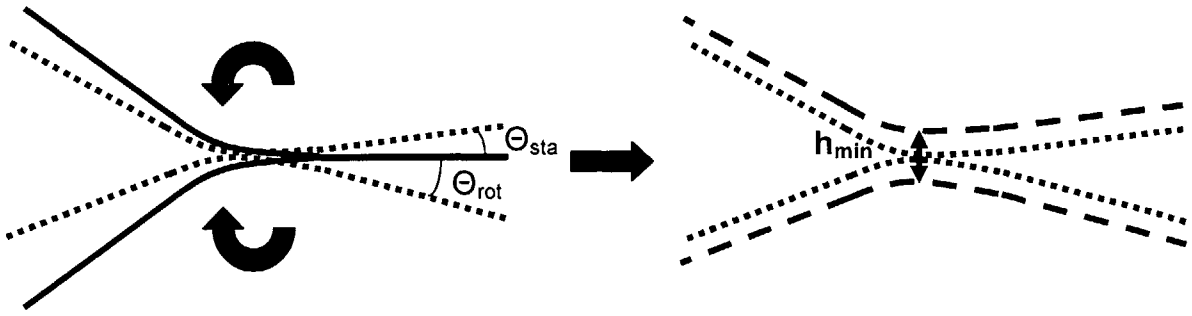

Figure 2.10 Finding minimum film thickness after adding twist angles

2.4 The cavitation model

2.4.1 Backgrounds for cavitation

Cavitation refers to the disruption of a liquid film by the presence of a gas or vapor [20]. Figure 2.11 shows an infinite bearing with symmetric gap heights along the center. If cavitation does not occur, the pressure distribution would also be symmetric, and no net hydrodynamic lift force would be generated. However, it is known that the emission of air or gas dissolved in the liquid occurs at the saturation pressure. This pressure is called the cavitation pressure, and is usually determined by experiments. Typically, the cavitatation pressure of oil which contains dissolved air is close to atmospheric pressure. With cavitation effects, pressure distribution in the cavitation zone will be constant at the cavitation pressure as shown in Figure 2.11. From the asymmetry of pressure distributions, net lift force can be generated with cavitaion effects.

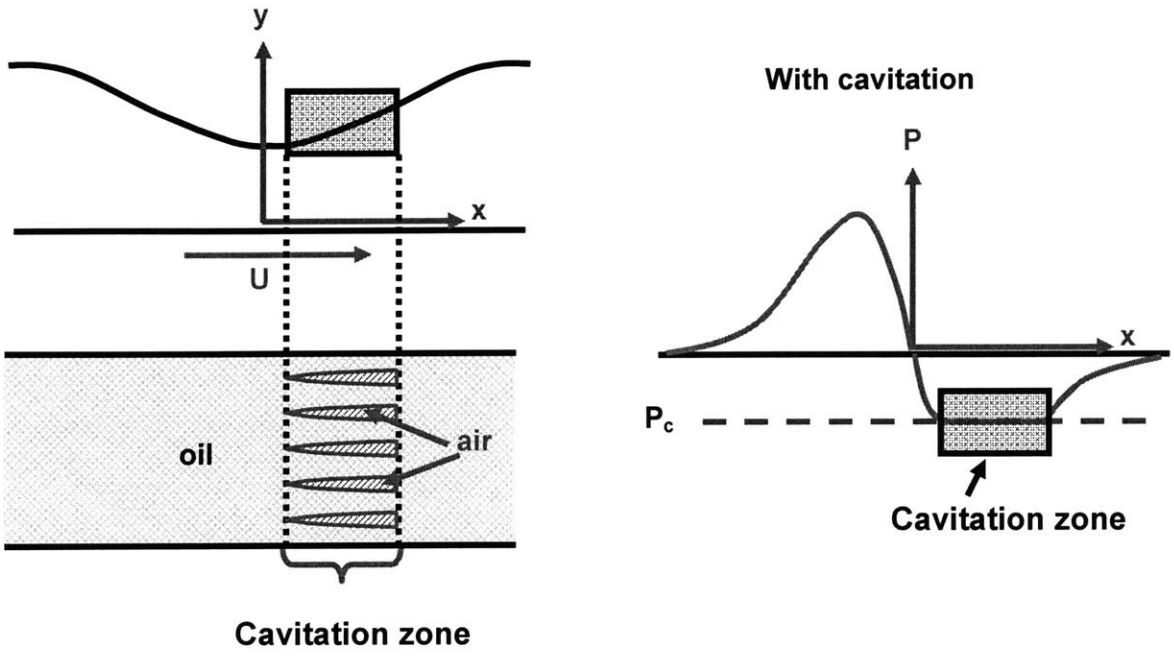

Figure 2.11 The view of cavitation regions and pressure distribution

The cavitation zone is a mixture of air streamers and liquid flows as shown in Figure 2.11. With positive hydrodynamic lift force, cavitation can drive oil into the sealing band due to the low pressure in the cavitation zone. On the other hand, high friction can occur in the cavitation zone if gap heights are so small that some dry contacts occur in air streamers.

2.4.2 The cavitation model

The cavitation model is developed based on Payvar and Salant's work [21]. The cavitation model calculates cavitation areas and the flow field in an oil film from solving the steady unified Reynolds equation with Floberg's boundary condition [22]. This boundary condition of cavitation assumes that all the lubricant flow passes between the air cavities as shown in Figure 2.12 (a). In addition, none of the lubricant flow is carried away under or over the cavitation region by the moving surfaces. Thus, the side view of the lubricant flow in the cavitation zone shows that the region is filled by the lubricant

flow only as shown in Figure 2.12 (b). Similarly, the vertical cross section along a gas streamer is filled by the gas only. These assumptions are used for the frictional heat calculation in section 2.5.4. Floberg's boundary condition of cavitation region was validated from experiments of a lightly loaded rotating cylinder against a stationary plane [20].

The other possible boundary condition at the film rupture due to cavitation is shown in Figure 2.12 (c). In this case, a significant amount of the lubricant flow is carried under the cavitation region by the moving surface. Thus, the cross section of the lubricant flow near the film rupture is filled by gas and lubricant. The effects of this possible boundary condition will be discussed in section 2.5.4.

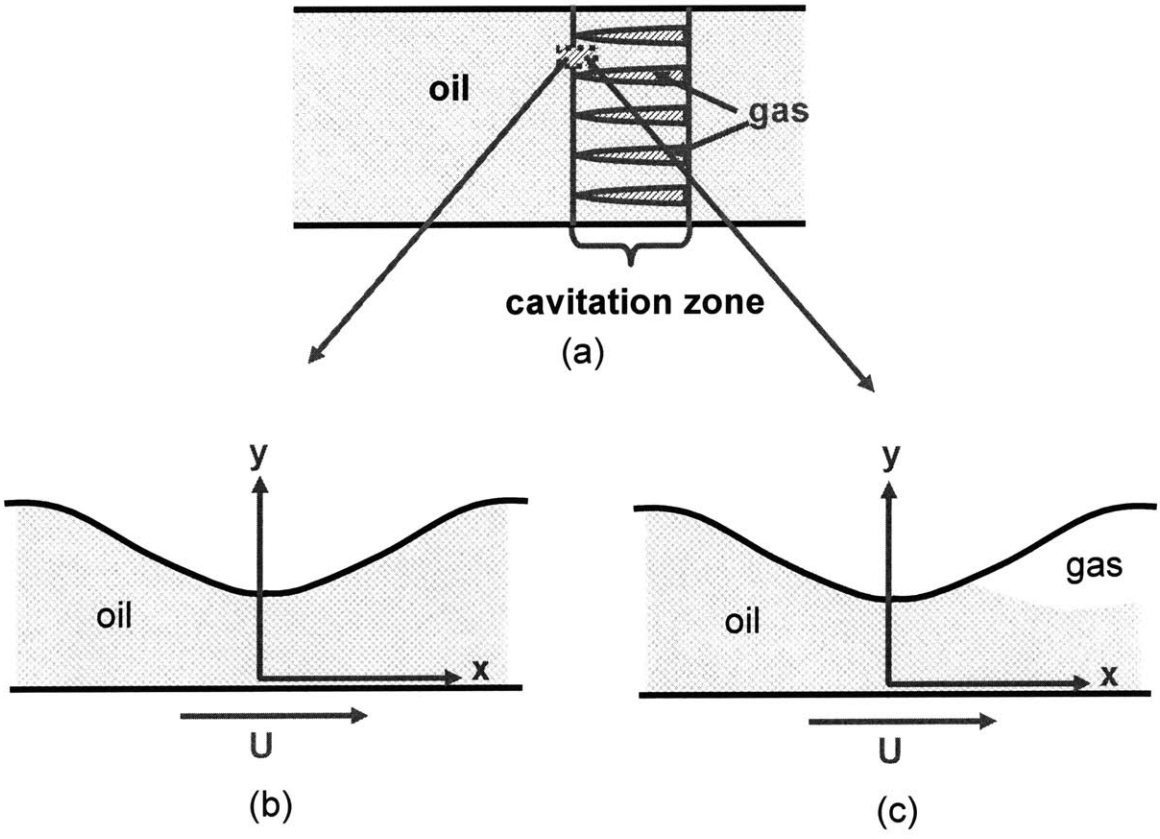

Figure 2.12 (a) The bottom view of the cavitation region (b) Side view along the lubricant flow with a full liquid film (c) Side view along the lubricant flow with a gas-liquid interface

The cavitation model using Floberg's boundary condition needs to solve the following equation

$$\frac{1}{r}\frac{\partial}{\partial r}\left(rh^3\frac{\partial P}{\partial r}\right)+\frac{1}{r}\frac{\partial}{\partial \theta}\left(\frac{h^3}{r}\frac{\partial P}{\partial \theta}\right)=6\mu\omega\frac{\partial h}{\partial \theta} \qquad \textbf{(2.3)}$$

in the oil film zone and the following equation

$$\frac{\partial}{\partial \theta}\left(\frac{\rho}{\rho_c}h\right)=0 \qquad \textbf{(2.4)}$$

in the cavitation zone. Boundary conditions at inside and outside radius are written as,

$P=P_s$ at $r=r_i$ (inside raidus) **(2.5)**

$P=P_a$ at $r=r_o$ (outside radius) **(2.6)**

where P_s is the sealed pressure and P_a is the atmospheric pressure.

The above two equations, (2.3) and (2.4), can be unified to a universal differential equation by introducing a variable ϕ whose definition changes in the oil film and the cavitation zone. Definitions of the variable ϕ and the cavitation index F are as follows,

$$\frac{P-P_C}{P_S-P_C}=F\phi \qquad \textbf{(2.7)},$$

$$\frac{\rho}{\rho_{oil}}=1+(1-F)\phi \qquad \textbf{(2.8)},$$

where F=1 for $\phi>0$ and F=0 for $\phi<0$. From definitions, ϕ represents a dimensionless pressure in the liquid film while $(1+\phi)$ characterizes the ratio of the averaged density to the oil density in the cavitation zone.

With following dimensionless variables,

$$\eta=\frac{r}{r_i}, H=\frac{h}{h_{ref}}, \gamma=\frac{6\mu\omega}{P_S-P_C}\left(\frac{r_i}{h_{ref}}\right)^2,$$

equations (2.3) and (2.4) can be combined as

$$\frac{1}{\eta}\frac{\partial}{\partial\eta}\left(\eta H^3\frac{\partial(F\phi)}{\partial\eta}\right)+\frac{1}{\eta}\frac{\partial}{\partial\theta}\left(\frac{H^3}{\eta}\frac{\partial(F\phi)}{\partial\theta}\right)=\gamma\frac{\partial\left[(1+(1-F)\phi)H\right]}{\partial\theta} \qquad \textbf{(2.9)}$$

with following boundary conditions,

$$\phi=1.0 \quad \text{at} \quad \eta=1 \quad \textbf{(2.10)},$$

$$\text{and} \quad \phi=\frac{P_a-P_c}{P_s-P_c} \quad \text{at} \quad \eta=r_o/r_i \quad \textbf{(2.11)}.$$

Equation (2.9) is solved using the TDMA algorithm with relaxations of ϕ and F to ensure numerical stability. In other words, values of ϕ and F are updated at each iteration step as follows,

$$\phi=\alpha\phi_{new}+(1-\alpha)\phi_{old} \qquad \textbf{(2.12)}$$

$$F=\beta F_{new}+(1-\beta)F_{old} \qquad \textbf{(2.13).}$$

To ensure numerical stability, small values of relaxation coefficients, α and β, are required [21].

The cavitation model generates the oil pressure distribution, the cavitation zone, and the density distribution in the oil film. The density distribution in the cavitation zone is expressed with the partial film content, which is the ratio of the averaged density in the cavitation zone to the density of the lubricant. The partial film content will be used to calculate frictional heat flux and the average properties of the oil film in the cavitation zone.

2.4.3 The quasi-steady cavitation model

When both of the rotating and stationary seal are wavy, the unsteady Reynolds equation needs to be solved instead of the steady one, equation (2.9). Currently, only a steady cavitation model is available with considering different gap heights and contact areas for each rotation step. In other words, the quasi-steady cavitation model, instead of the unsteady cavitation model, is used for the current numerical models.

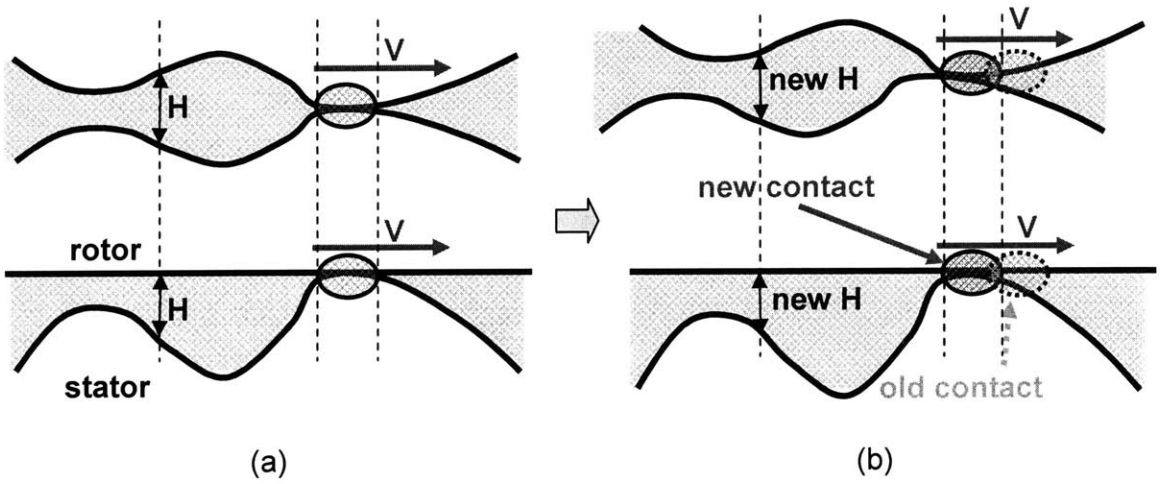

Figure 2.13 Transformations to the smooth rotor and wavy stator surfaces

As shown in Figure 2.13 (a), two wavy surfaces are transformed to the smooth rotor and the wavy stator surface with equivalent gap heights and contact areas. With these transformed surfaces, the lubrication becomes steady, and the steady Reynolds equation can be solved. For next rotation step, gap heights and contact areas would be changed as shown in Figure 2.13 (b). Again, the steady cavitation model with different equivalent gap heights and contact areas generates the oil pressure distribution, the cavitation zone, and the density distribution in the oil film. These procedures are repeated for every rotation step during one revolution.

2.5 Calculation of frictional heat flux in the sealing band

2.5.1 Definitions of contact regions and wet/dry contacts

In this thesis, contact regions do not mean actual contact regions but nominal contact regions. It is well known that actual contact regions are much smaller than nominal contact regions [23]. The rest of areas in the sealing band besides the nominal contact regions are defined as the non contact regions.

Contact regions are further divided into dry and wet contacts depending on the presence of lubricant. For dry contact, friction only comes from contact pressures at contact regions. On the other hand, friction comes from contact pressure and viscous heating of the lubricant for wet contact (see Figure 2.14). Viscous heating of the lubricant can be significant in nominal contact regions due to small gap heights. Details in calculations of frictional heat for different contact conditions are in following sections.

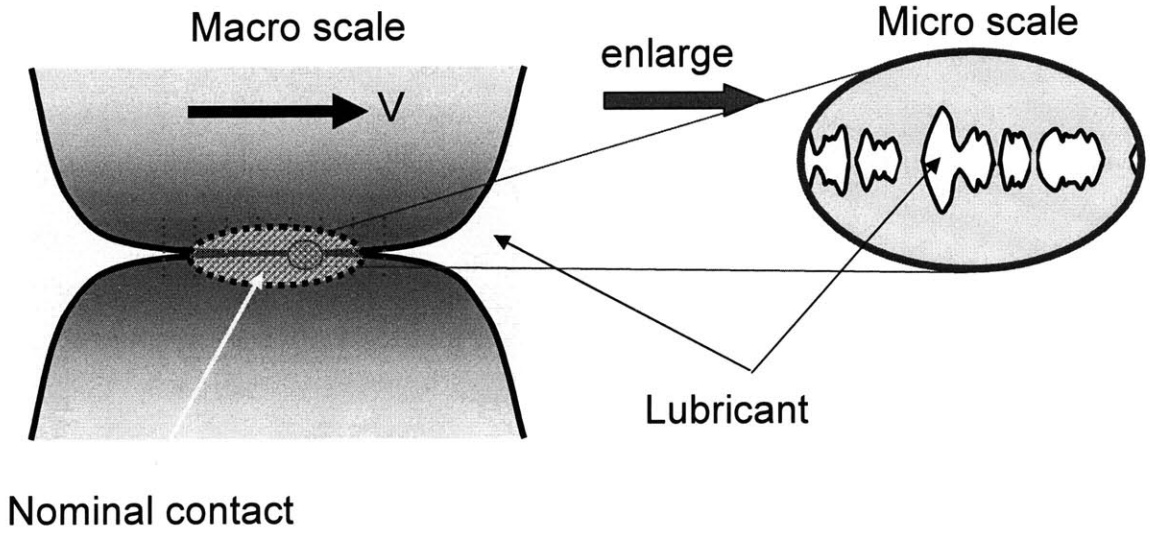

Figure 2.14 Nominal contact vs. real contact regions

2.5.2 Calculation of frictional heat flux in dry condition

In this case, the only source of friction is from contact pressures. Thus, the frictional heat flux for dry contact is obtained from,

$$q_{con} = f_d P_{con} V \quad [\mathrm{W/m^2}] \qquad \textbf{(2.14)},$$

f_d: dry friction coefficient,

P_{con} : contact pressure [Pa],

V : relative sliding velocity [m/s].

On the other hand, no source of friction exists in non contact regions. Thus, the frictional heat flux for non contact regions in the dry condition is zero.

2.5.3 Calculation of frictional heat in wet condition

In the wet condition, friction comes from both contact pressures and viscous heating of the lubricant in nominal contact regions. The frictional heat flux for contact regions is expressed as,

$$q_{con} = f_b P_{con} V + \frac{\mu_{oil}(T_{oil,avg}) V^2}{H} \quad [\mathrm{W/m^2}] \qquad \textbf{(2.15)},$$

where f_b : boundary friction coefficient.

Note that the viscosity of oil depends on the average temperature of the oil film (for definition, see section 2.7).

In non contact regions, the only source of friction is from viscous heating of the lubricant. Thus, the frictional heat flux for non contact regions can be written as,

$$q_{non-con} = \frac{\mu_{oil}(T_{oil,avg}) V^2}{H} \quad [\mathrm{W/m^2}] \qquad \textbf{(2.16)},$$

where $\mu_{oil}(T_{oil,avg})$: the viscosity of the lubricant [N s/m^2],

H : gap height [m].

2.5.4 Calculation of frictional heat considering cavitation effects

The previous section deals with the full lubrication condition without considering cavitation effects. As shown in Figure 2.15, cavitation regions are a mixture of the lubricant and air. The cavitation model calculates the average density of the two phase fluid.

The partial film content, λ_{ij}, is defined as the ratio of the averaged density in element (i,j) to the density of the lubricant. Note that i and j are the index numbers in the x and y direction, respectively. When $\lambda_{ij} = 1$, the the lubricant completely fills in element (i,j). Thus, the properties in this element should be the same as those of the lubricant. If $\lambda_{ij}=0$, it means that the lubricant is vaporized completely, and the element is entirely filled with air.

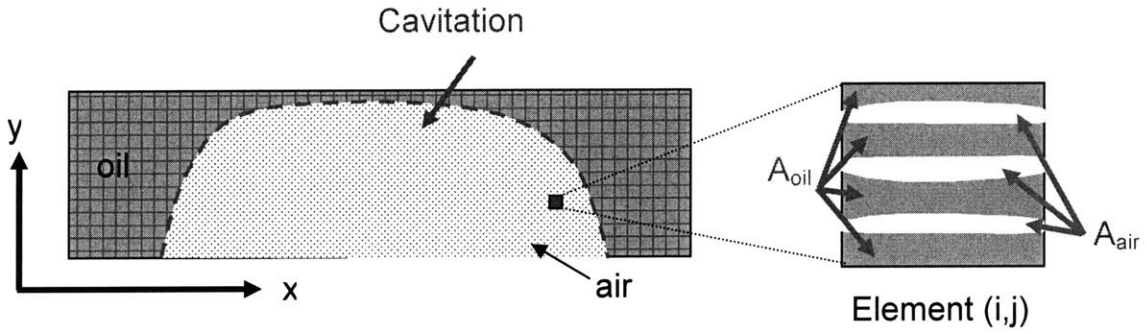

Figure 2.15 The element in the cavitation zone

In this case, the properties in element (i,j) should be the same as those of air. With these two extremes, the average viscosity and conductivity of two phase fluid in element (i,j) can be approximated by using λ_{ij} as follows:

$$\mu_{ij,cav} = \lambda_{ij}\,\mu_{oil}(T_{oil,avg}) + (1-\lambda_{ij})\mu_{air} \approx \lambda_{ij}\mu_{oil}(T_{oil,avg}) \quad [\text{N s/m}^2] \quad \textbf{(2.17)},$$

$$k_{ij,cav} = \lambda_{ij} k_{oil} + (1 - \lambda_{ij}) k_{air} \qquad \text{[W/m K]} \qquad \textbf{(2.18)},$$

where $\lambda_{ij} = \dfrac{\rho_{ij,avg}}{\rho_{oil}}$: partial film content in element (i,j)

and $\rho_{ij,avg}$: the average density of two phase fluid in element (i,j) [kg/m^3].

From the definition of the average density of two phase fluid,

$$\rho_{ij,avg} V_{ij} = \rho_{oil} V_{ij,oil} + \rho_{air} V_{ij,air} \qquad \textbf{(2.19)},$$

where V_{ij}: the total volume in element (i,j) [m^3],

$V_{ij,oil}$: the volume occupied by the lubricant in element (i,j),

$V_{ij,air}$: the volume occupied by air in element (i,j).

From $V_{ij} = V_{ij,oil} + V_{ij,air}$, we can get $\dfrac{\rho_{ij,avg}}{\rho_{oil}} V_{ij} = \lambda_{ij} V_{ij} = V_{ij,oil} + \dfrac{\rho_{air}}{\rho_{oil}} V_{ij,air} \approx V_{ij,oil}$. It is thus possible to write,

$$\frac{V_{ij,oil}}{V_{ij}} = \frac{A_{ij,oil}}{A_{ij}} = \lambda_{ij} \qquad \textbf{(2.20)}$$

where $A_{ij,oil}$: the area occupied by oil in element (i,j) [m^2],

$A_{,ij,air}$: the area occupied by air in element (i,j),

A_{ij}: the total area of element (i,j),

because gap heights in the element are nearly the same if the element size is small enough. In other words, λ_{ij} represents the ratio of the area occupied by the lubricant over the total area of element (i,j).

From heat balance in element (i,j) for contact areas,

$$\left(f_b P_{ij,con} V + \mu_{oil}(T_{oil,avg}) \frac{V^2}{H_{ij}} \right) A_{ij,oil} + f_d P_{ij,con} V A_{ij,air} = q_{ij,con} A_{ij} \qquad \textbf{(2.21)},$$

where $P_{ij,con}$: the contact pressure in element (i,j) [Pa],

H_{ij} : the gap height in element (i,j) [m],

$q_{ij,con}$: the frictional heat flux from element (i,j) in contact areas [W/m^2],

and V: sliding velocity [m/s].

Finally, the frictional heat flux from element (i,j) in contact areas can be written as,

$$q_{ij,con} = (f_b P_{ij,con} V + \frac{\mu_{oil}(T_{oil,avg}) V^2}{H_{ij}})\lambda_{ij} + f_d P_{ij,con} V (1-\lambda_{ij}) \qquad \textbf{(2.22)}.$$

Note that above equation is the same as the frictional heat flux in the contact regions for dry contacts when $\lambda_{ij}=0$. When $\lambda_{ij}=1$, the heat flux is same as the frictional heat flux in the contact regions for wet contacts without cavitation.

On the other hand, the frictional heat flux in non contact regions only considers viscous heating from the lubricant. Thus, it can be written as,

$$q_{ij,non-con} = \frac{\mu_{oil}(T_{oil,avg}) V^2}{H_{ij}} \lambda_{ij} \quad \textbf{(2.23)}$$

where $q_{ij,\text{non-con}}$: the frictional heat flux from element (i,j) in non contact areas [W/m^2].

Note that equations (2.22) and (2.23) assume that only lubricant fills in the vertical gap of A_{oil} with a linear velocity profile. If some proportion of the lubricant flow is carried away under or over the cavitation region by the moving surfaces (see Figure 2.12 (c)), the viscous heating from the lubricant flow will decreases while the conductivity through the gaps of the lubricant flow in the cavitation zone also decreases. In addition, the velocity profile of the lubricant carried by the moving surface is non-linear because the shear stress at the air-lubricant interface is close to zero. Thus,

frictional heat calculations should be modified if other cavitation boundary conditions besides Floberg's boundary condition are used.

2.6 The 3D thermal model

2.6.1 Assumptions of the 3D thermal model

Once the distribution of frictional heat flux in the sealing band is known, the friction coefficient can be calculated from,

$$f = \frac{\sum_{i=1}^{N} \sum_{j=1}^{M} q_{ij} A_{ij}}{Support \quad Load \cdot Sliding \ Speed} \quad \textbf{(2.24)},$$

where q_{ij} : the heat flux in element (i,j) [W/m^2],
A_{ij}: the area of element (i,j) [m^2].

In general, the distribution of frictional heat flux changes with rotation due to changes in contact areas, contact pressure, and cavitation areas. Thus, a friction coefficient also changes for each rotation step as shown in Figure 2.16 (c) below.

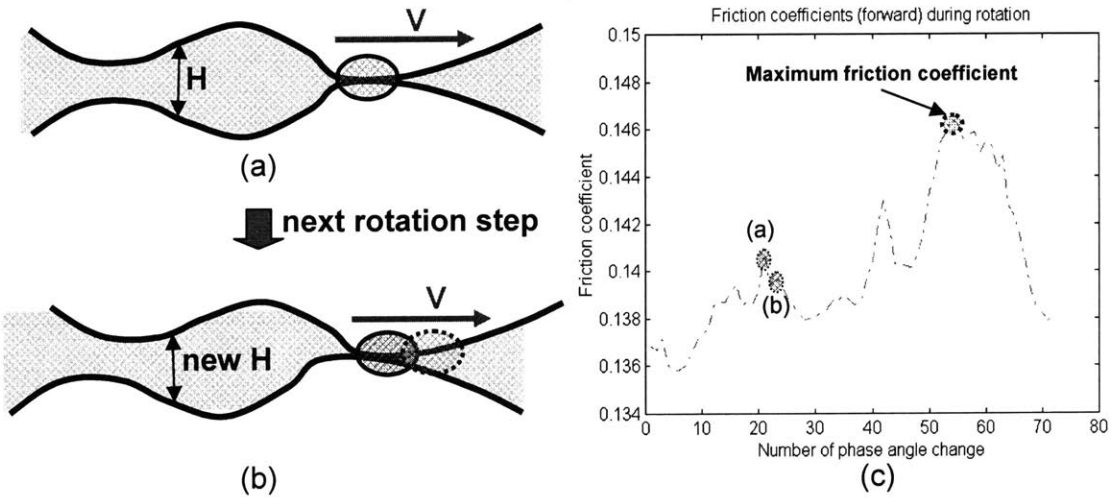

Figure 2.16 Changes of contact areas and friction coefficients during rotation

Recall that friction coefficient calculations come from the quasi-steady cavitation model, which solves the steady unified Reynolds equation with equivalent gap heights for each rotation step. However, the heat transfer process is still unsteady because contact areas of the rotor surface, as well as heat flux to the rotor, change with rotations (see Figure 2.17).

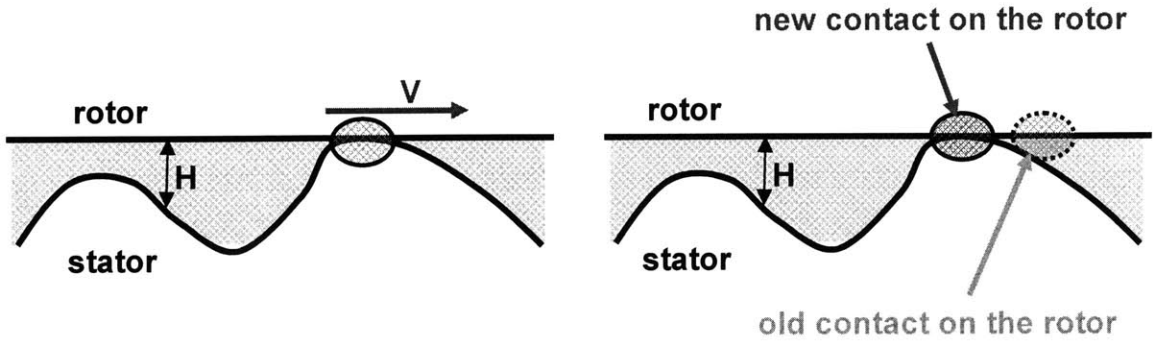

Figure 2.17 Contact changes on the rotor

It is known that circumferential temperature variations due to variations of heat flux are negligible compared to the mean temperature in many seals [24]. These variations are especially small with large thermal inertia and the high rotation velocity of the rotor. In this case, unsteady effects on the rotor due to circumferential variations of heat flux can be neglected.

Circumferential temperature variations due to heat flux variations are roughly estimated for the FMMFS. From the conduction solution of the semi-infinite solid subjected to a periodic heat flux with amplitude of q_0 [25], the amplitude of circumferential temperature variation can be written as,

$$\Delta T \sim \frac{q_0}{k}\left(\frac{\alpha}{\omega}\right)^{1/2} \qquad \textbf{(2.25)}$$

where $q_0 \sim f\ V\ P_{con} \sim O(10^6)$ W/m^2, k(conductivity) ~ O(10) W/mK, α(thermal diffusivity) ~ $O(10^{-6})$ m^2/s, ω(rotation frequency) ~ $O(10^2)$ rad/s for the FMMFS. Then, $\Delta T \sim O(10)$ C while average temperatures of rotor surfaces are $O(10^2)$ C. This rough estimate shows that circumferential temperature variations are one order of magnitude less than average temperatures of the rotating surface. Thus, the assumption of negligible circumferential temperature variations is reasonable.

Using this assumption, the heat transfer process can be simplified as a quasi-steady process at each rotation step. Then, the thermal model needs to solve the 2D steady conduction equation for the rotor, and the steady 3D conduction equation for the stator. However, solving the 3D steady conduction equation for every rotation step still requires tremendous computation costs. Thus, the thermal model computes steady 3D temperature distributions at one moment during the rotation. The most important moment during the rotation is when maximum friction occurs. Temperature distribution would be an upper bound calculation at the maximum friction. One example of the moment of maximum friction during one revolution is indicated in Figure 2.16 (c).

Additional assumptions are made for the 3D thermal model. Frictional heat fluxes are concentrated in the middle of the oil film, and temperature profiles in the oil film are linear. These assumptions are valid when conduction across the oil film dominates convection along the circumference. The FMMFS operate in the boundary lubrication regime where the film thickness is less than the order of micrometers. Under typical operating speed (~O(1m/s)) and scales along the circumference(~O(100mm)) and the radius (~O(1mm)), conduction term across the oil film dominates other terms in the energy equation. These assumptions have been widely used for temperature calculations of the seal system [15, 24].

2.6.2 Boundary conditions of the 3D thermal model

In order to solve conduction equations, distribution of frictional heat flux in the sealing interface at maximum friction is used as one of the boundary conditions. Convection boundary conditions are used at inside seal surfaces and outside seal surfaces (see Figure 2.18). Details in calculating heat transfer coefficients for convection are described in section 3.2. The 3D thermal model imposes adiabatic boundary conditions

on the rest of boundaries. These boundary conditions are validated by comparisons with experiments in the next chapter.

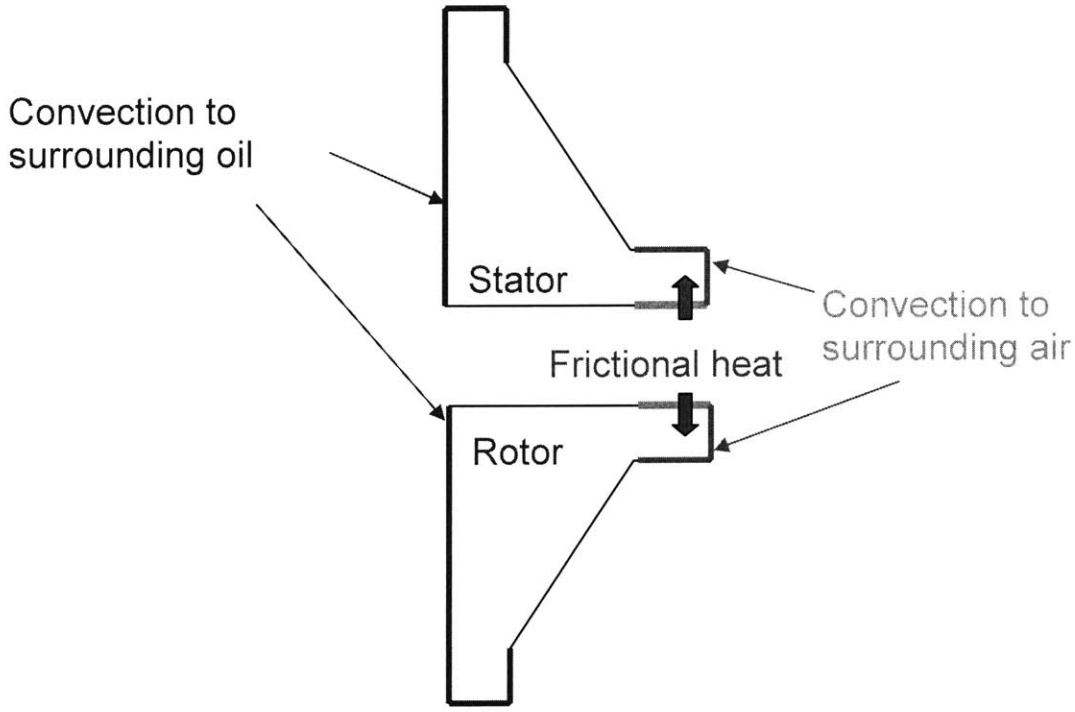

Figure 2.18 Boundary conditions of the 3D thermal model

2.6.3 Temperature calculations of oil film, stator and rotor

A thermal resistance along the indicated line is shown in Figure 2.19 . With concentrated heat flux and linear temperature profile assumptions, heat flux to the rotor ($q_{r,j}$) and heat flux to the stator ($q_{s,ij}$) can be expressed as,

$$q_{r,j} = \left(\sum_{i=1}^{N} k_{oil} \frac{T_{oil,ij} - T_{rotor,j}}{H_{ij}/2}\right) / N \qquad \textbf{(2.26)},$$

and $$q_{s,ij} = k_{oil} \frac{T_{oil,ij} - T_{stator,ij}}{H_{ij}/2} \qquad \textbf{(2.27)}$$

where k_{oil}: the conductivity of the oil [W/m C],

$q_{r,j}$: the average heat flux into rotor element j [W/m^2],

$T_{rotor,j}$: the axis-symmetric temperature on rotor element j [C],

$q_{s,ij}$: the heat flux into stator element (i,j) [W/m^2],

$T_{stator,ij}$: the temperature on stator element (i,j) [C],

$T_{oil,ij}$: the temperature in the middle of the oil film in element (i,j),

N : the number of circumferential nodes.

Note that heat flux to the rotor element ($q_{r,j}$) needs to be averaged along the circumference from the assumption of negligible circumferential temperature variations. Also note that k_{oil} should be replaced with $k_{cav,ij}$ from equation (2.18) in the cavitation zone.

Thus,

$$T_{oil,ij} = \frac{1}{2}\left(T_{rotor,j} + T_{stator,ij} + \frac{(q_{r,j} + q_{s,ij})}{k_{oil}} \frac{H_{ij}}{2} \right) \quad \textbf{(2.28).}$$

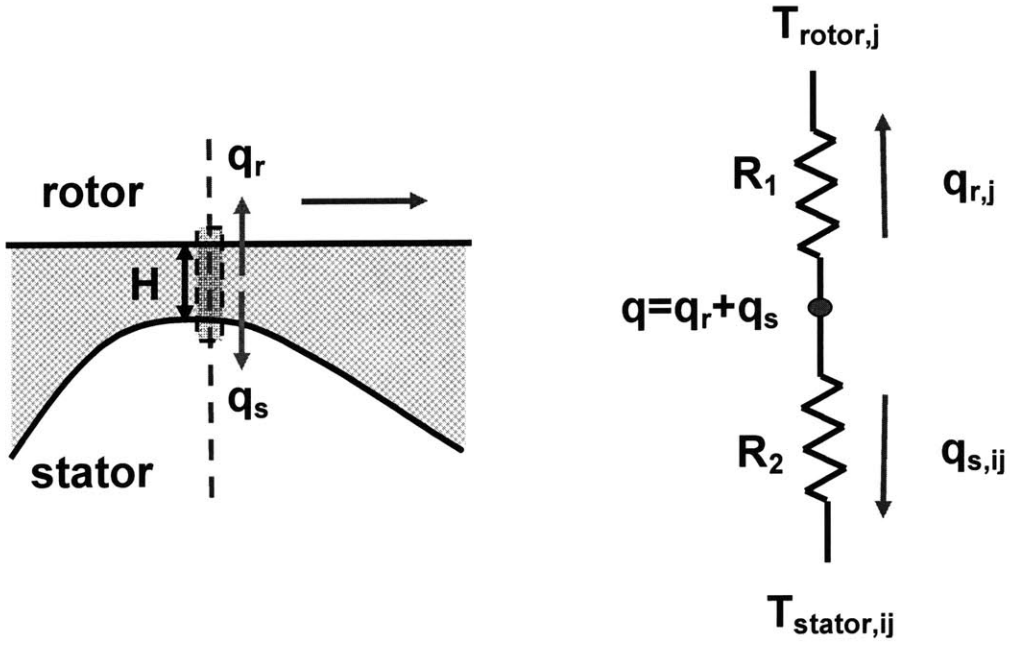

Figure 2.19 Thermal resistances of the oil film and heat divisions

Recall that total frictional heat flux distribution, $q_{r,j}+q_{s,ij}$, is known already. Once temperatures on the rotor and the stator surface are assumed initially, or known afterwards, $T_{oil,ij}$ can be calculated from equation (2.28). Then, the 3D thermal model calculates $q_{r,j}$ and $q_{s,ij}$ from equation (2.26) and (2.27). These heat flux distributions to the rotor and the stator surface are used as boundary conditions for conduction equations.

With the distribution of heat flux to the rotor $q_{r,j}$ and the heat transfer coefficient for rotating convection boundary, following conduction equation is solved for the rotor ,

$$\frac{1}{r}\frac{\partial T}{\partial r}+\frac{\partial^2 T}{\partial r^2}+\frac{\partial^2 T}{\partial z^2}=0 \qquad \textbf{(2.29).}$$

Equation (2.29) is discretized into finite difference equations by applying energy conservation to a control volume of each element. Figure 2.20 shows the heat balance in element (i,j) of the rotor.

Each heat flux into the element can be written as,

$$q_r = k\frac{T_{i-1,j}-T_{i,j}}{dr},\ q_{r+dr} = k\frac{T_{i+1,j}-T_{i,j}}{dr},\ q_z = k\frac{T_{i,j-1}-T_{i,j}}{dz},\ \text{and}\ q_{z+dz} = k\frac{T_{i,j+1}-T_{i,j}}{dz}.$$

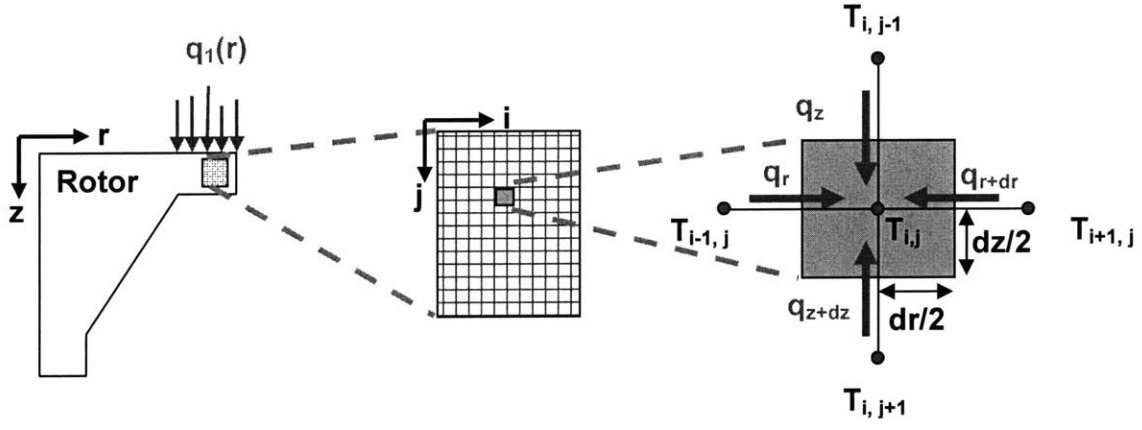

Figure 2.20 The control volume of the element

From applying energy conservation to the control volume,

$$q_r(r-\frac{dr}{2})d\theta dz+q_{r+dr}(r+\frac{dr}{2})d\theta dz+q_z r d\theta dr+q_{z+dz} r d\theta dr=0 \quad \textbf{(2.30).}$$

Finite difference equations can be obtained from plugging each heat flux into equation (2.30). Thus,

$$T_{i-1,j}\frac{k(r-\frac{dr}{2})dz}{dr}+T_{i+1,j}\frac{k(r+\frac{dr}{2})dz}{dr}-T_{i,j}\,2\left(\frac{krdz}{dr}+\frac{krdr}{dz}\right)+T_{i,j-1}\frac{krdr}{dz}+T_{i,j+1}\frac{krdr}{dz}=0 \quad \textbf{(2.31).}$$

According to the boundary condition and shape of the boundary, finite difference equations can vary by applying energy conservation to different control volumes and to the heat flux into them. For instance, at the convection boundary shown in Figure 2.21 below, heat inflows to the control volume of the element are,

$$q_r=h(T_f-T_{i,j}),\ q_{r+dr}=k\frac{T_{i+1,j}-T_{i,j}}{dr},\ q_z=k\frac{T_{i,j-1}-T_{i,j}}{dz},\ \text{and}\ q_{z+dz}=k\frac{T_{i,j+1}-T_{i,j}}{dz}.$$

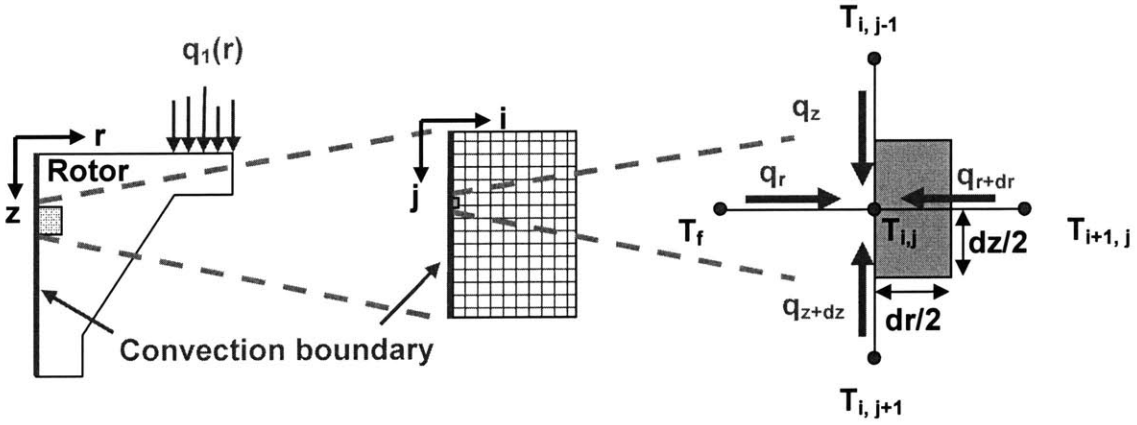

Figure 2.21 The control volume of the boundary element

From energy conservation,

$$q_r r\,d\theta dz + q_{r+dr}(r+\frac{dr}{2})d\theta dz + q_z(r+\frac{dr}{4})d\theta\frac{dr}{2} + q_{z+dz}(r+\frac{dr}{4})d\theta\frac{dr}{2} = 0 \qquad \textbf{(2.32).}$$

Finally,

$$T_f hrdz + T_{i+1,j}\frac{k(r+\frac{dr}{2})dz}{dr} - T_{i,j}\left(hrdz + \frac{k(r+\frac{dr}{2})dz}{dr} + \frac{k(r+\frac{dr}{4})dr}{dz}\right) + T_{i,j-1}\frac{k(r+\frac{dr}{4})\frac{dr}{2}}{dz} + T_{i,j+1}\frac{k(r+\frac{dr}{4})\frac{dr}{2}}{dz} = 0 \qquad \textbf{(2.33).}$$

In the same way, the 3D thermal model calculates temperature distribution of the stator with the distribution of $q_{s,ij}$ and heat transfer coefficients. For the stator, the following steady 3D conduction equation should be solved,

$$\frac{1}{r}\frac{\partial T}{\partial r} + \frac{\partial^2 T}{\partial r^2} + \frac{1}{r^2}\frac{\partial^2 T}{\partial \theta^2} + \frac{\partial^2 T}{\partial z^2} = 0 \qquad \textbf{(2.34).}$$

Compared to the rotor case, adding circumferential heat inflows to each control volume is necessary to obtain finite difference equations.

After obtaining finite difference equations, the Gauss-Seidel iteration scheme is used to solve these algebraic equations. For each iteration step, temperatures of the stator and the rotor change. These changes lead to a different oil temperature distribution ($T_{oil,ij}$) from equation (2.28), then result in changes in $q_{r,j}$ and $q_{s,ij}$ from equation (2.26) and (2.27). For each iteration, the relaxation coefficient (relax_q) are used to update values of $q_{r,j}$ and $q_{s,ij}$ to avoid numerical instability. Thus, for each iteration step,

$$q_{r,j} = (relax\_q) * q_{r,j,new} + (1 - relax\_q) * q_{r,j,old} \qquad \textbf{(2.35),}$$

$$q_{s,ij} = (relax\_q) * q_{s,ij,new} + (1 - relax\_q) * q_{s,ij,old} \quad \textbf{(2.36)},$$

where $q_{r,j,new}$: the updated value of heat flux into rotor element j,

$q_{r,j,old}$: the previous value of heat flux into rotor element j,

$q_{s,ij,new}$: the updated value of heat flux into stator element (i,j),

$q_{s,ij,old}$: the previous value of heat flux into stator element (i,j).

Iterations are continued until temperature distributions of the oil film, the stator, and the rotor converge.

2.7 Iterations of the 3D contact model, the cavitation model, and the 3D thermal model

After calculating the temperature distribution, the program calculates the residuals of the averaged oil temperature ($T_{oil,avg}$) and twist angles. $T_{oil,avg}$ is defined as,

$$T_{oil,avg} = \frac{\sum_{i=1}^{N}\sum_{j=1}^{M} T_{oil,ij}}{(N \cdot M)} \quad \textbf{(2.37)}$$

where $T_{oil,ij}$: the temperature of oil in element (i,j),

N: the number of circumferential nodes,

and M: the number of radial nodes.

The residual of $T_{oil,avg}$ is written as,

$$residual\ of\ T_{oil,avg} = \frac{T_{oil,avg}^{new} - T_{oil,avg}^{old}}{T_{oil,avg}^{old}} \quad \textbf{(2.38)},$$

where $T_{oil,avg}^{new}$: the updated average temperature of oil,

$T_{oil,avg}^{old}$: the previous average temperature of oil.

On the other hand, the residual of twist angles is expressed as,

$$residual\ of\ twist\ angles = \frac{\sum_{i=1}^{N}(twist\ angle_i^{new} - twist\ angle_i^{old})}{\sum_{i=1}^{N} twist\ angle_i^{old}} \qquad \textbf{(2.39)},$$

where $twist\ angle_i^{new}$: the updated twist angle at radial cross section i,

$twist\ angle_i^{old}$: the previous twist angle at radial cross section i.

The program continues until sufficient convergences of $T_{oil,avg}$ and twist angles are reached. Final outputs are contact pressures, final gap heights with twist angles, cavitation index, partial film contents, frictional heat flux to the stator and the rotor, friction coefficients, and temperatures of whole seal system.

3 Validations of numerical models

Once numerical models have been developed, they need validation to justify the underlying assumptions and to check the accuracy of final results. This chapter describes the validation process for numerical models that have been developed in the last chapter.

3.1 Experimental setup

For validations of numerical models, the model results are compared with two measurable quantities: temperatures and friction coefficients. The experiment was conducted in a separte effort by the project sponsor. Experimental procedures are shown in Figure 3.1.

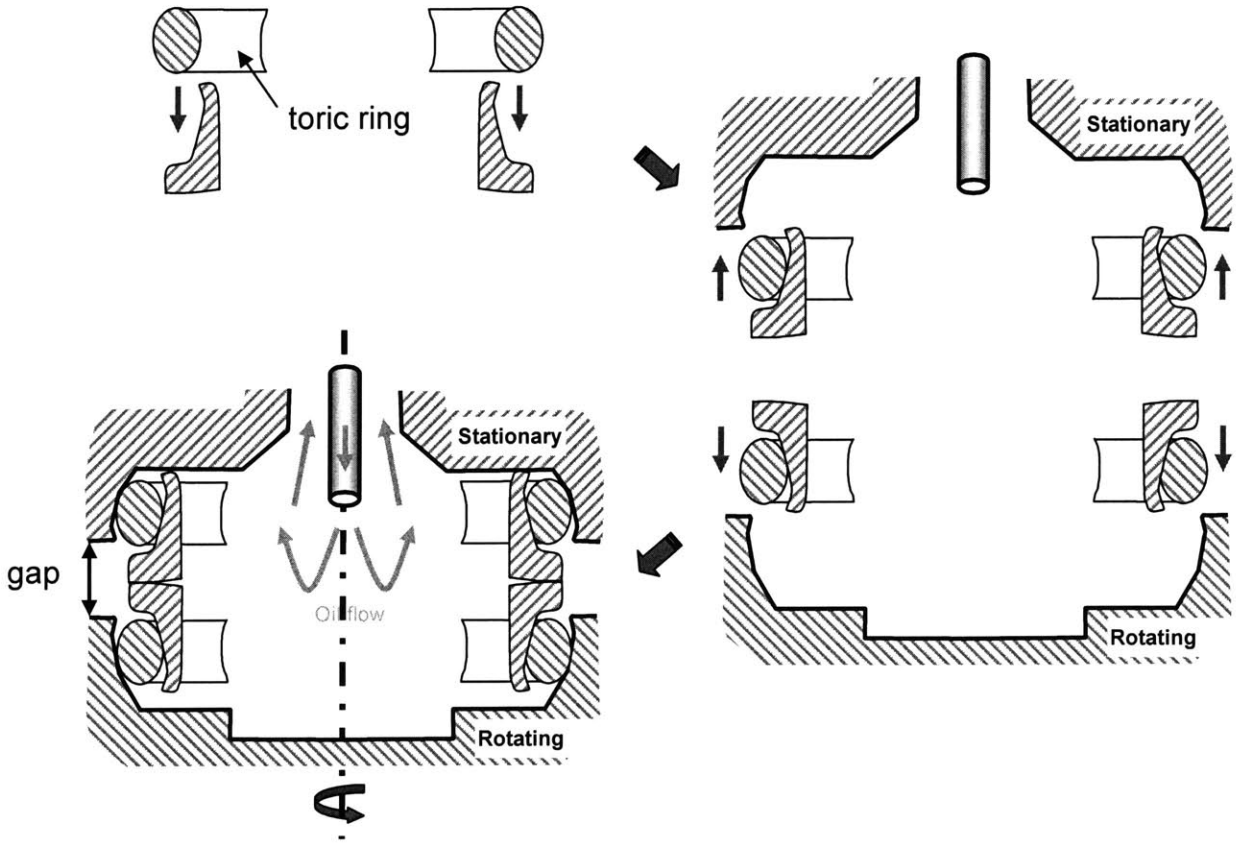

Figure 3.1 Experimental procedures

As a first step, an elastomeric toric ring is pushed into the back surface of the seal. The seal pair with the toric ring is inserted into two separate fixtures; one remains stationary while the other rotates. Before inserting the ring into the fixture, a small amount of oil is spread on the sealing interface to prevent initial dry contacts. The inserted seal with the rotating fixture moves upward and presses the other seal up to the desired vertical load. Then, the oil flow comes into the cavity through the pipe in the middle of the stationary fixture. The oil flow bounces back to the annular tube between the pipe in the middle and the inside surface of the stationary fixture. After that, the rotating fixture with the inserted seal starts to rotate and to increase speed gradually. The vertical load, rotating speed, oil flow rate, and the pressure in the cavity can be programmed in advance.

Torque is measured so that friction coefficients can be calculated with rotating speeds and vertical load. In addition, temperature in the middle of the flange at the outer diameter of the stationary seal is measured using thermocouples as shown in Figure 3.2.

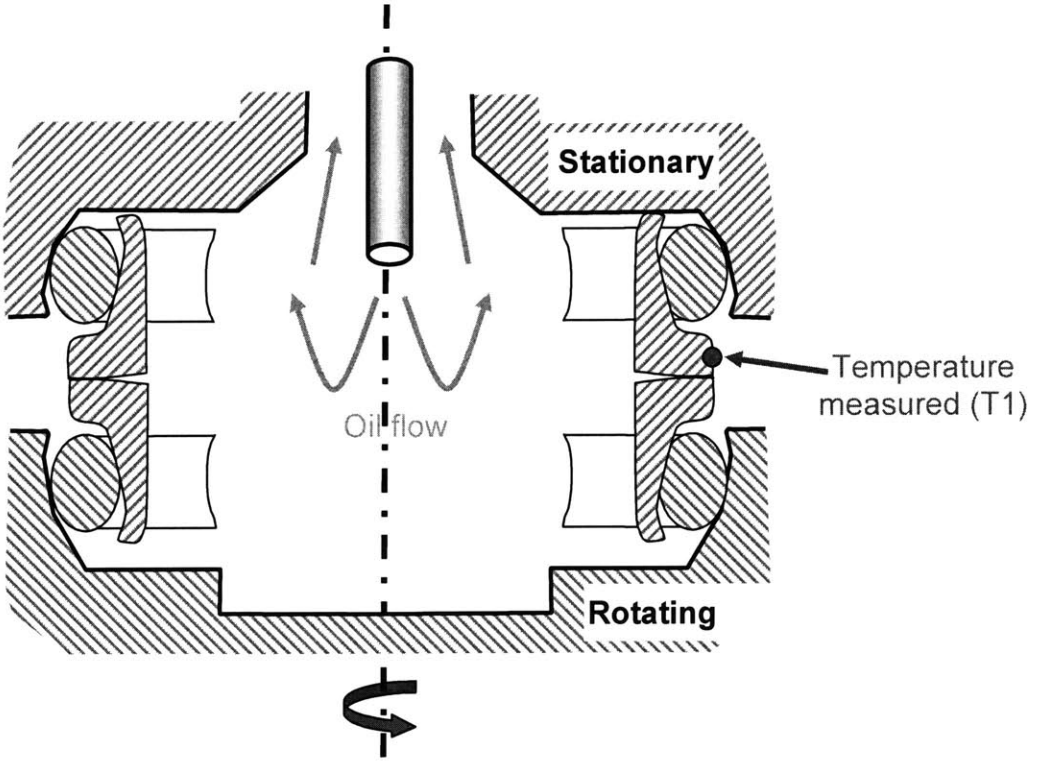

Figure 3.2 Temperature measurement at the outer diameter

Sometimes two thermocouples are attached at different circumferential locations to check possible circumferential temperature variations. In this case, one thermocouple is attached at the peak position of the measured waviness of the stationary seal, while the other thermocouple is attached at the valley of the waviness.

3.2 Estimations of heat transfer coefficients

Heat transfer coefficients to the surrounding oil flow are important input parameters for the 3D thermal model. Heat transfer coefficients for inside surfaces of the rotor and the stator are used as convection boundary conditions (see section 2.6.2).

Prior to this thesis work, heat transfer coefficients were obtained from correlations of the rotating cylinder [26, 27], or adjustments by trials and error to match temperature measurements. However, the former method is not applicable to a complex flow such as one in the current experimental setup (see Figure 3.2). The latter method is useful to determine heat divisions to the stator and the rotor, but it can not predict changes of heat transfer coefficients with different oil flows and speed changes. Thus, estimations of heat transfer coefficients from CFD simulations would be beneficial.

The fluid motion in the current experimental setup is complicated due to its three dimensional features. Once the scheme for finding heat transfer coefficients for this complex flow has been developed, the same scheme would be easily applicable to other simpler flows.

3.2.1 New scheme for calculations of heat transfer coefficients

The surrounding oil is the main heat sink for the frictional heat generated at the interface. The fluid motion of oil is inherently three dimensional and requires extensive CFD analysis. The most direct approach is to simulate the heat transfer process by considering the oil flow model and the thermal model of the seal pair together. This approach should solve fluid motion, heat transfer of the oil flow, and conduction of the

seal pair simultaneously. Such a procedure might be possible, but the computation cost would be tremendous and beyond our computation capability.

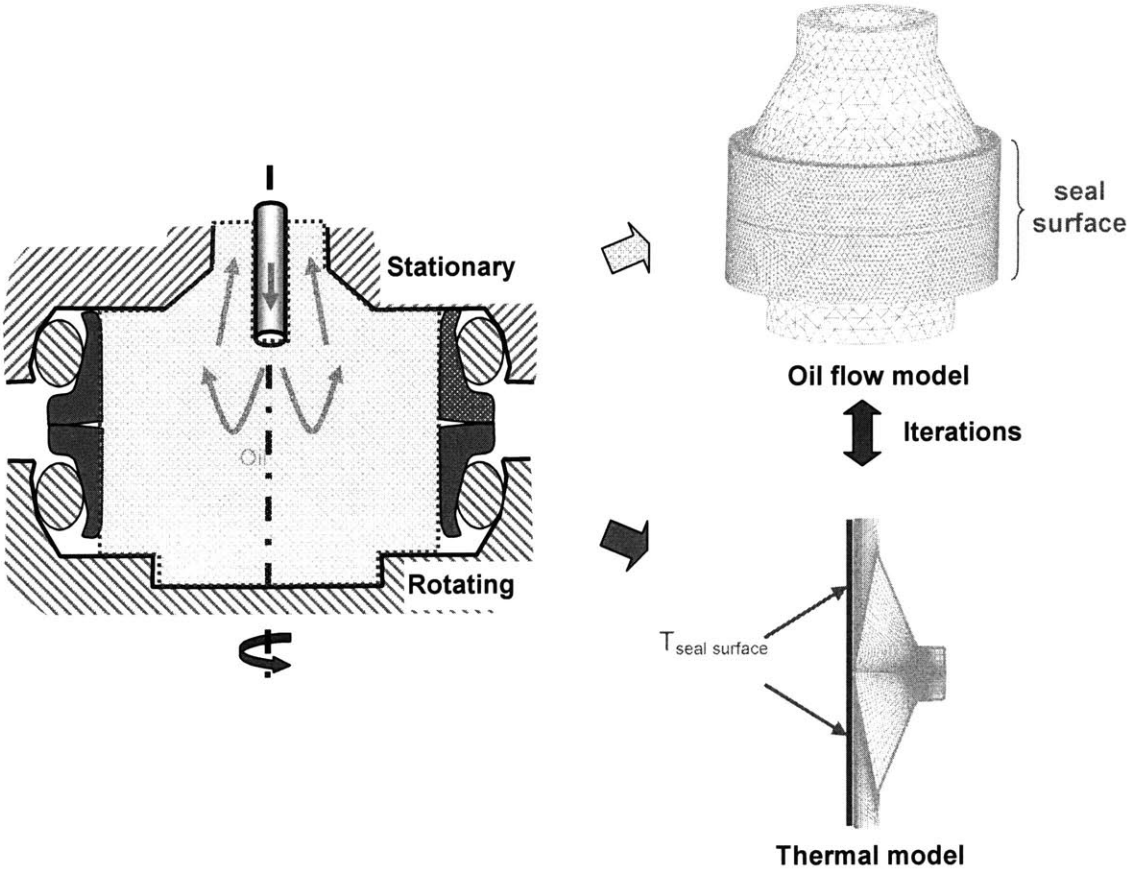

Figure 3.3 New scheme for calculations of heat transfer coefficients

Therefore, the new scheme for finding heat transfer coefficients is devised. The oil flow model and the thermal model of the seal pair are separated as shown in Figure 3.3. At first, the oil flow model calculates heat transfer coefficients and the thermal model uses them as convection boundary conditions. After calculating the temperatures of the seal pair from the thermal model, the oil flow model uses seal surface temperatures as temperature boundary conditions. Such iterations are repeated until heat transfer coefficients and temperatures converge (see Figure 3.4). More details of the two models and the iteration procedures are described in following sections.

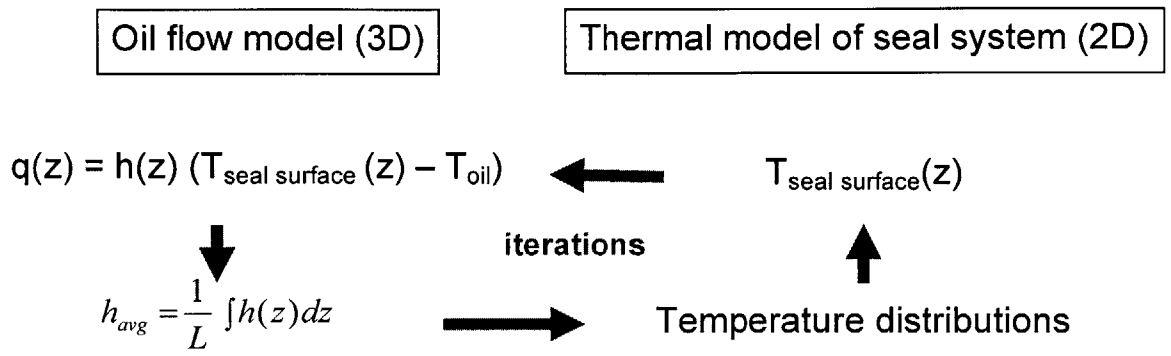

Figure 3.4 Iterations between two models

3.2.2 3D oil flow model

The commercial finite element package, ADINA™, is used for the 3D oil flow model. For the 3D oil flow model, ADINA-F™ with heat transfer is used to solve the fluid motion of oil flows with heat transfer. Tetrahedral 4-node elements are used due to the relatively high Reynolds number of the oil flow. Still, Reynolds numbers for the rotating seal surface based on seal radius are less than 2000 until operating speed reaches to 2 m/s, thus oil flows are still laminar. This laminar assumption is questionable for higher speeds and a turbulent flow model would be more adequate for speeds higher than 2.5 m/s. Much finer meshes are used near seal surfaces to deal with high velocity and temperature gradients (see Figure 3.3).

Figure 3.5 shows fluid and thermal boundary conditions of the oil flow model. For the inlet and outlet of the cavity, fully developed velocity profiles are imposed. Rotating velocity conditions are applied to the lower fixture and seal surface, while no slip boundary conditions are applied to the rest of surfaces in the cavity. Prescribed temperature boundary conditions are also imposed on the inlet and both inside seal surfaces as thermal boundary conditions.

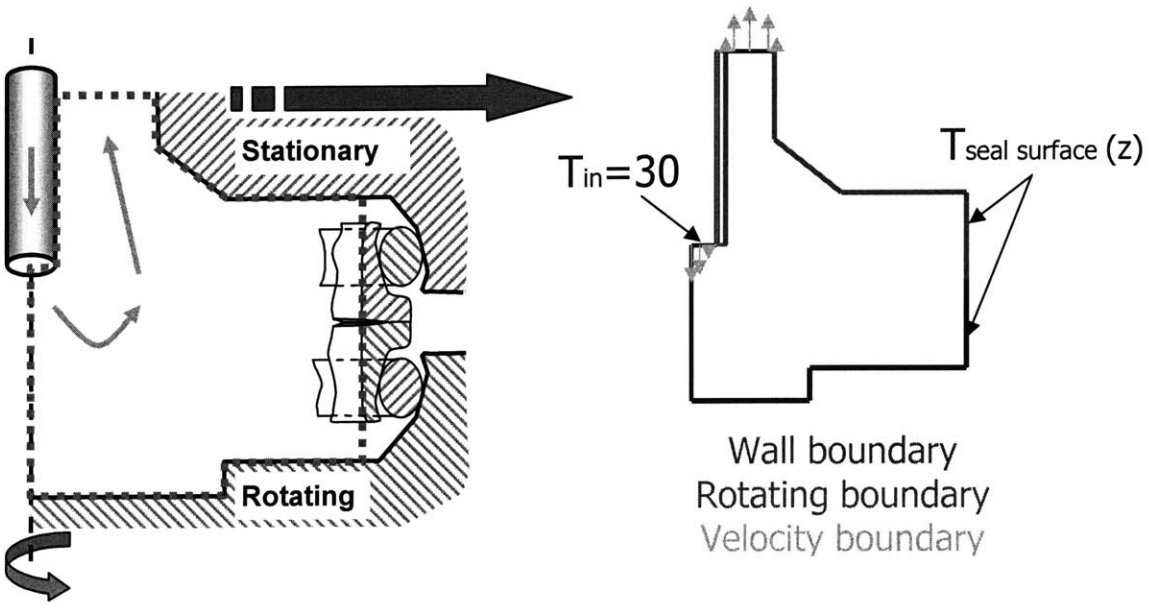

Figure 3.5 Boundary conditions of the oil flow model

It is known that the viscosity of oil (SAE 10W) depends highly on temperature. From the Vogel equation [28], the relation between low shear kinematic viscosity and temperature is expressed as,

$$\nu_0 = k\exp(\frac{\theta_1}{\theta_2 + T}),$$

where ν_0 : the kinematic viscosity of the low shear rate oil in cSt

k(cSt), θ_1(°C) and θ_2(°C) : correlation constants for an oil

T (°C) : oil temperature.

For accurate calculations of fluid motion and heat transfer of the oil flow, changes of the viscosity with temperatures need to be considered.

Non-linear temperature dependence of the viscosity results in solving non-linear finite element equations. For convergence of solutions, the equations are solved in several time steps with incremental loading boundary conditions (see Figure 3.6). From the initial time step to the time step N_1, only fluid boundary conditions increase gradually without

changes in heat transfer boundary conditions. Then, from the time step N_1+1 to the last time step N_2, thermal loadings gradually increase while fluid boundary conditions are held costant. Between each time step, the Newton-Raphson iteration scheme is used to calculate solutions. The solutions in the previous time step are used as initial guesses for the next time step to ensure convergence of the Newton-Raphson iteration at each time step.

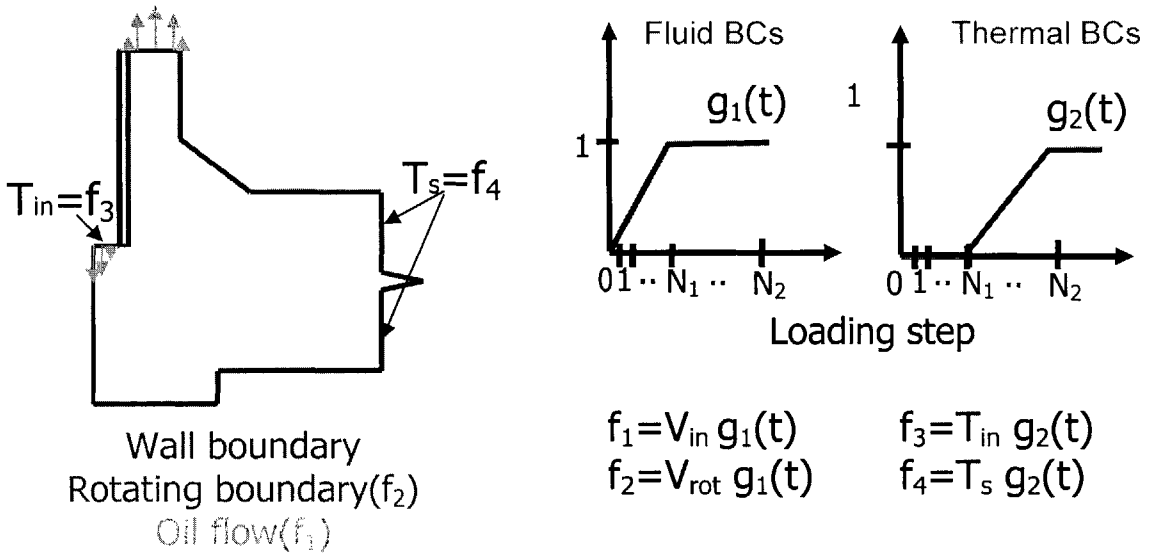

Figure 3.6 Incremental loadings of fluid and thermal BCs

3.2.3 2D thermal model

The oil flow model requires seal surface temperatures as thermal boundary conditions. These temperatures on the inside seal surface are nearly axis-symmetric because inside seal surfaces are far from the sealing band, the source of friction. This fact allows use of the axis-symmetric thermal model to calculate temperatures on the inside seal surface. Figure 3.7 shows finite element meshes with convection boundary conditions and concentrated heat flux at ID. The amount of concentrated frictional heat

flux comes from the torque sensor of the experimental setup. Adiabatic boundary conditions are used for the rest of boundaries.

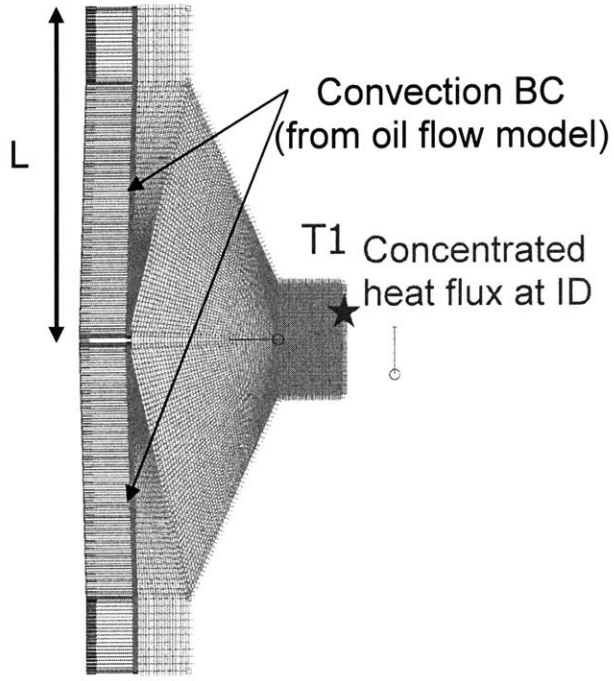

Figure 3.7 The 2D thermal model

3.2.4 Iterations between two models

The oil flow model starts with uniform inside seal surface temperatures. After convergence, heat flux magnitudes at several nodes on the seal surface are calculated. Heat transfer coefficients at each node are obtained from dividing this heat flux magnitude by the temperature difference between the temperature on the seal surface and the average oil flow temperature in the cavity. These heat transfer coefficients at different nodes are averaged for the rotating and the stationary seal surface using

$h_{avg} = \frac{1}{L}\int_z h(z)\,dz$ where L is the vertical length of inside seal serface (see Figure 3.7). Averaged heat transfer coefficients for both seals are used as convection boundary conditions for the 2D thermal model. After calculations, temperatures on the inside seal

surfaces are known and used as thermal boundary conditions of the oil flow model. The oil flow model starts computations with new temperature boundary conditions, then new heat transfer coefficients are obtained. Figure 3.8 shows the changes in temperatures and in the heat transfer coefficients of the stationary seal during these iterations. The rotating speed is 1.8m/s while normalized axial loads are 2.0[3] and 2.5, respectively.

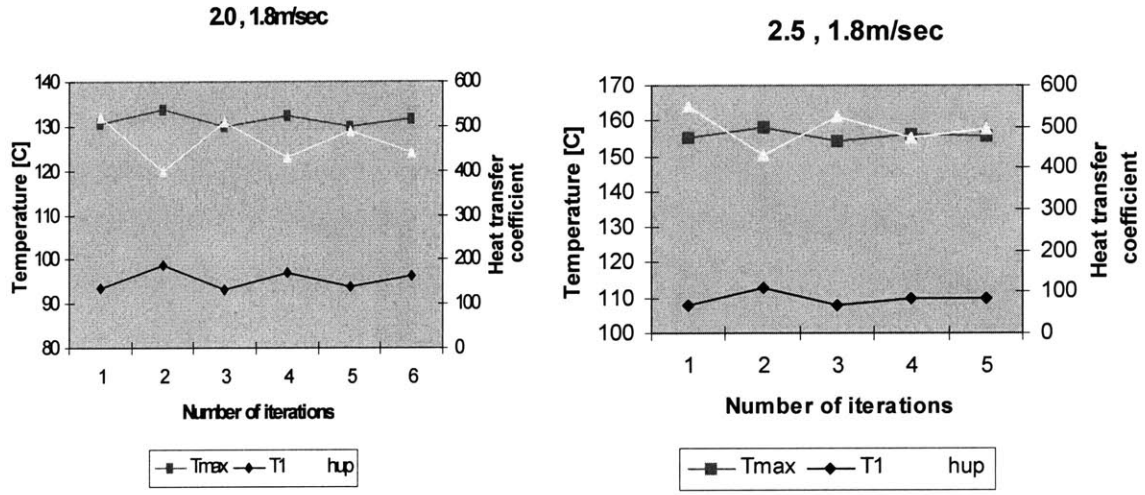

Figure 3.8 Changes of some variables during iterations

Results show that heat transfer coefficients and temperatures tend to converge within several iteration steps. 5-6 iterations are typical to estimate heat transfer coefficients while each iteration step usually takes 3-4 hours.

3.3 Numerical results

In this section, numerical results from each part of the models in a particular operating condition will be described. Figure 3.9 shows the surface profiles of the

[3] Total axial forces are normalized by 289 N in this thesis.

rotating and the stationary seal which are used in the experiments. Numerical results under the normalized axial force of 2.5 and the rotating speed of 1.8 m/s will be presented.

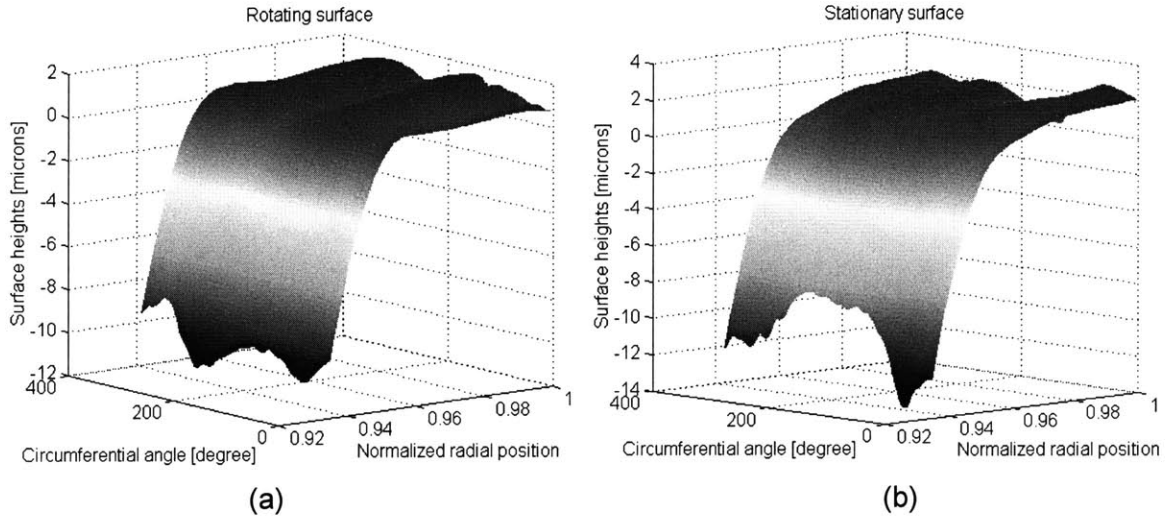

Figure 3.9 Surface profiles of (a) the rotating and (b) the stationary seal

3.3.1 Numerical results from the contact model

From the contact model, the final outputs are final gap heights after deformations and contact pressures. These numerical results from the 3D contact model are shown in Figure 3.10 (a) and (b), respectively.

Note the discontinuities in contact pressures around 40-140 degrees in circumferential angle shown in **Figure 3.11** (a). The radial surface profiles of the stationary surface around these regions with discontinuous contact pressures are shown in **Figure 3.11** (b). It is clearly shown that contact patterns depend on the radial surface profiles. Where the contacts occur near the outside diameter, the radial surface profiles increase with radial positions near the outside diameter. On the contrary, the radial surface profiles decrease near the outside diameter where the contacts occur inside

regions. Such different contact patterns, depending on the radial surface profiles, will lead to different distributions of frictional heat flux and temperatures.

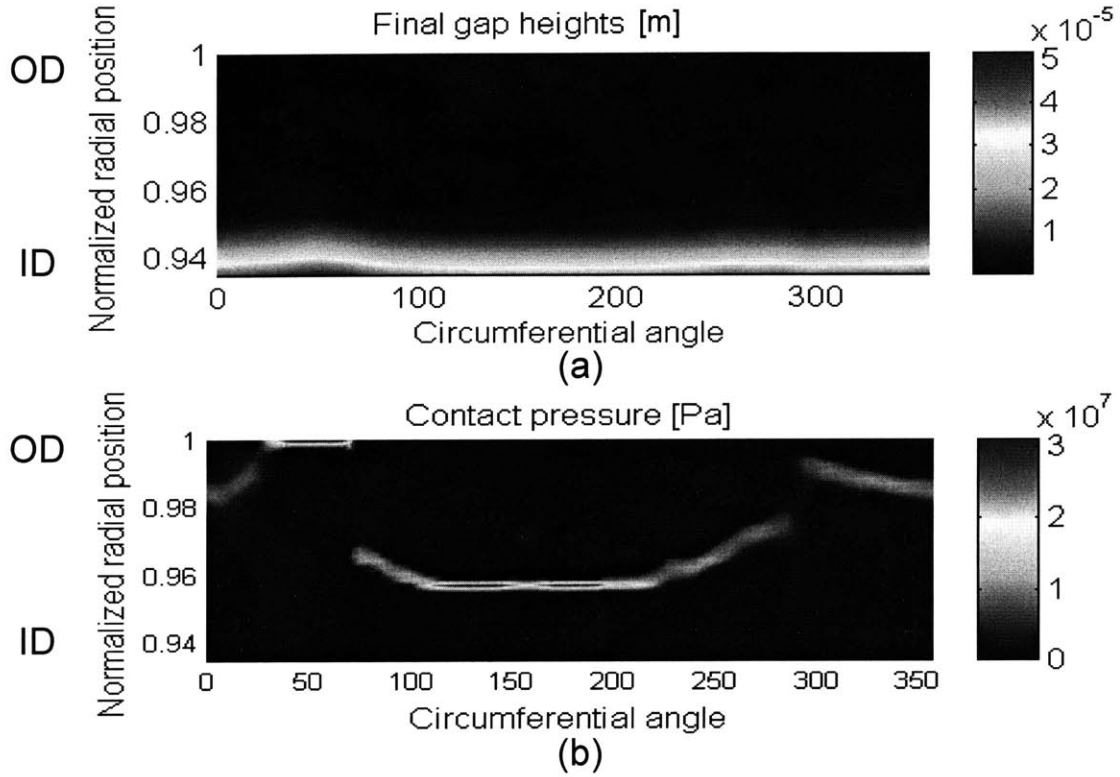

Figure 3.10 Distribution of final gap heights and contact pressures

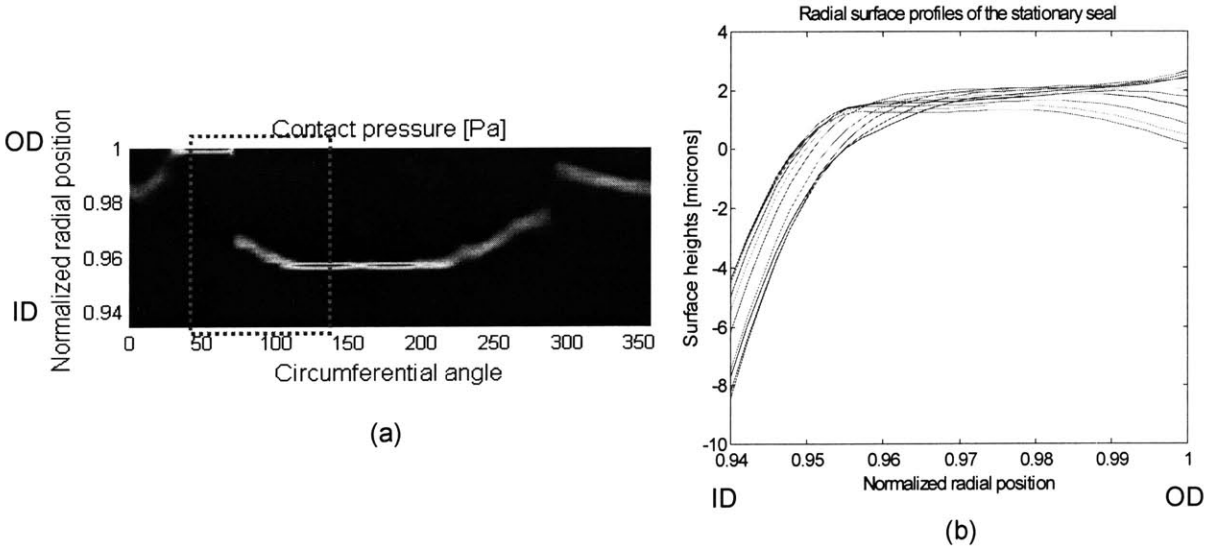

Figure 3.11 (a) Distribution of contact pressures (b) radial surface profiles of the stationary seal

Figure 3.12 shows the final gap heights and contact pressures at OD along the circumference. Along the circumference at OD, the contacts occur around 25-75 degrees as shown in Figure 3.12 (b). It is clearly shown that these contact regions correspond to those regions with the minimum final gap heights.

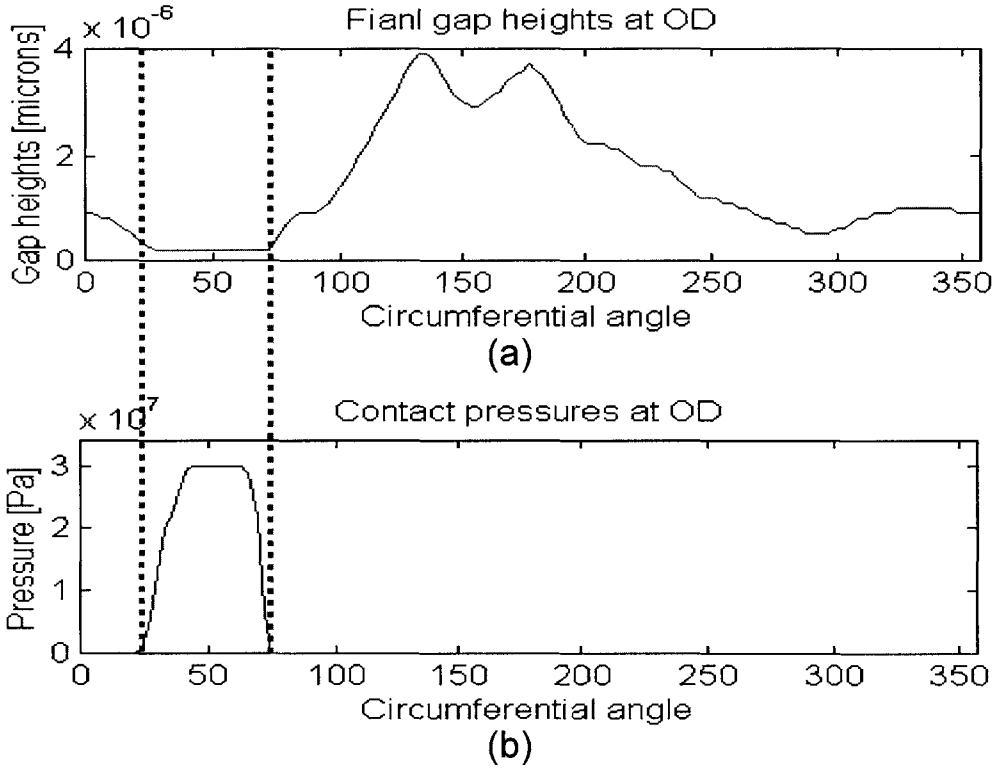

Figure 3.12 The final gap heights and contact pressures at OD

Figure 3.13 shows gap heights before and after deformations. Each figure represents contour plots of the same gap heights. It is clearly shown that initial gap heights are flattened out along the circumference after deformations except the middle parts near the OD. These facts confirm the simplification of the 3D contact model as well as that of negligible hydrodynamic effects on load supports.

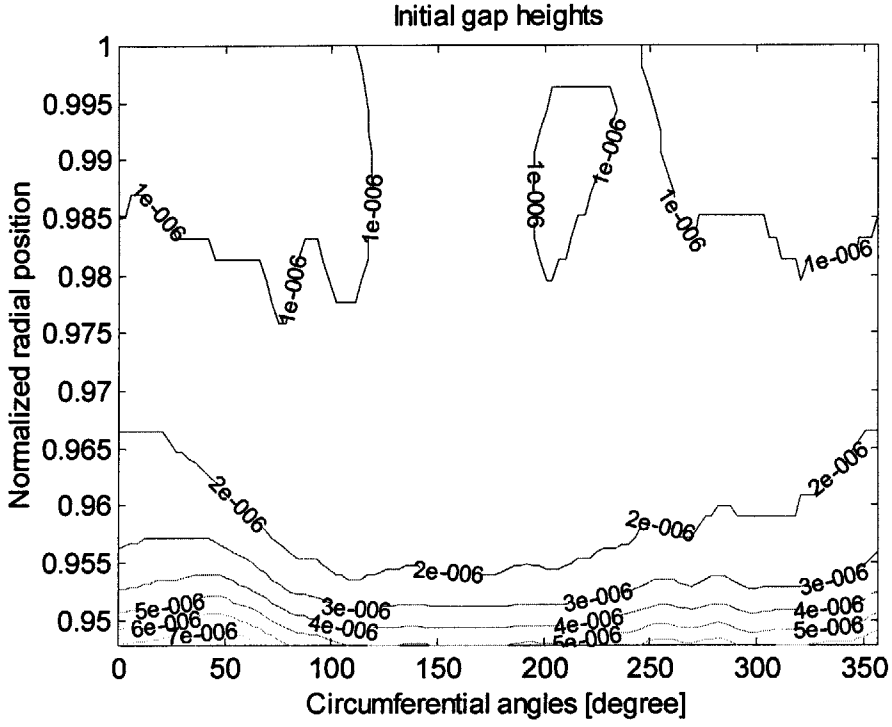

(a)

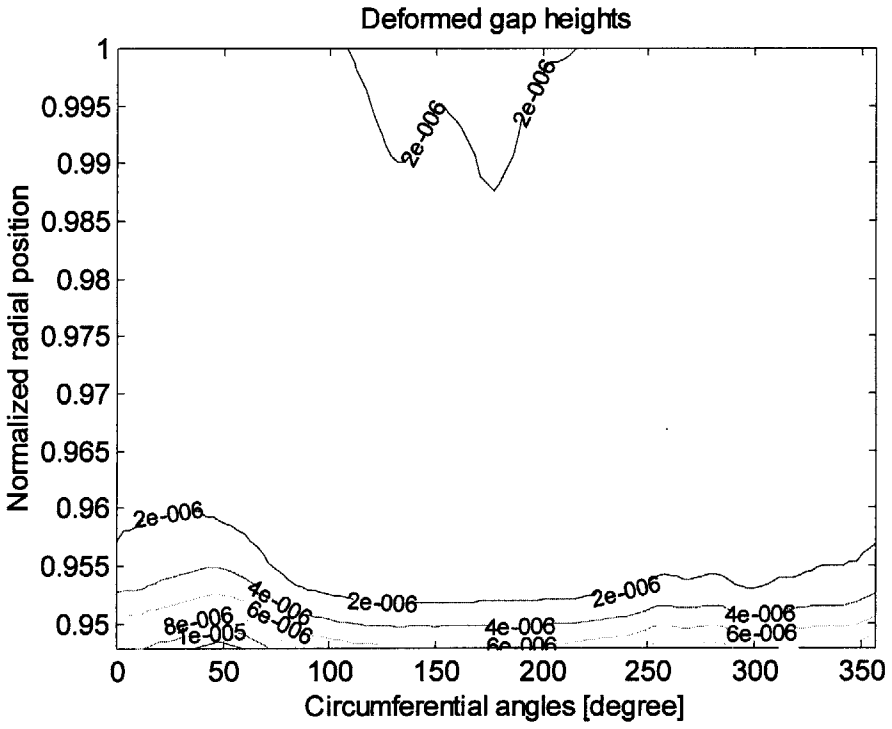

(b)

Figure 3.13 Initial gap heights (a) vs. deformed gap heights (b)

3.3.2 Numerical results from the cavitation model

With the final gap heights obtained previously, the cavitation model calculates cavitation regions and the average density of two phase fluid. Figure 3.14 (a) shows the distribution of the cavitation index. In the cavitation areas the partial film content, the ratio of average density over the lubricant density, is less than one as shown in Figure 3.14 (b) because the cavitation areas are a mixture of the lubricant and the air streamers. Subsequently, the distribution of the partial film content is used for frictional heat calculations.

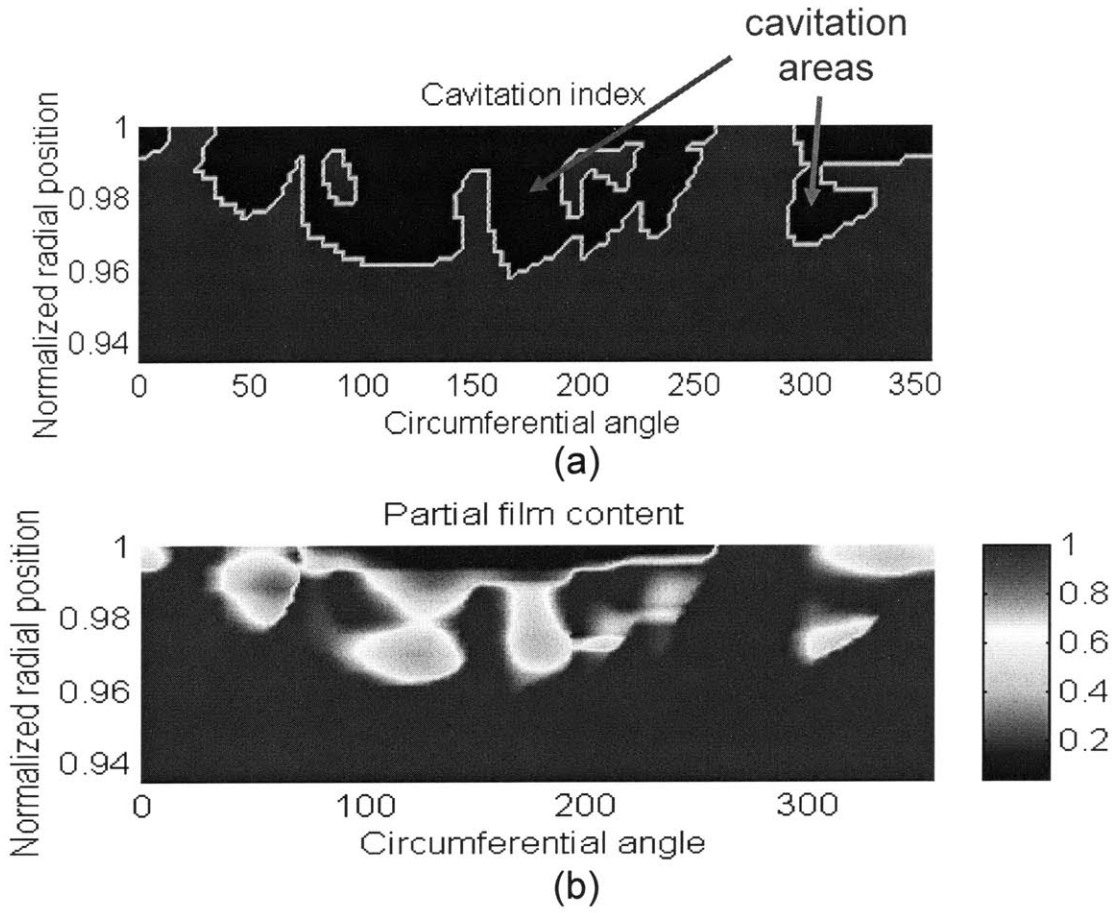

Figure 3.14 Distribution of (a) cavitation index and (b) partial film content

3.3.3 Numerical results from the thermal model

Distributions of the contact pressures and the partial film content are used for frictional heat calculations. The distribution of frictional heat flux into the stator surface is shown in Figure 3.15 (b). The distribution of frictional heat flux corresponds to that of the contact pressures in Figure 3.15 (a), because contact pressures are main sources of friction.

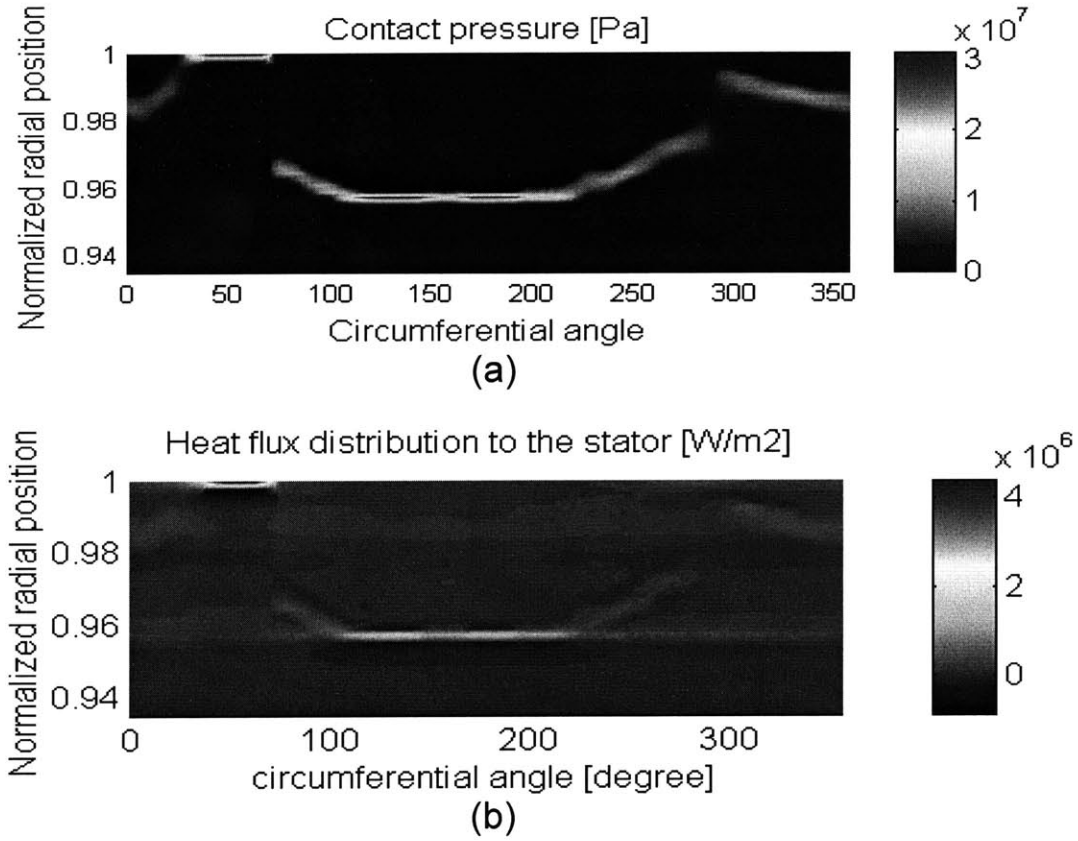

Figure 3.15 Distributions of (a) contact pressures and (b) frictional heat flux to the stator

Temperatures on the stator surface at the sealing interface are shown in Figure 3.16. As shown in Figure 3.16, the distribution of temperatures on the stator surface corresponds to that of the frictional heat flux into the stator surface.

The factors which lead to high heat flux regions shown in Figure 3.17 (c) are investigated. This high frictional heat flux is believed to come from high contact pressures in dry contact regions. Dry contact areas shown in Figure 3.17 (b) represent the

contact areas where the average density is less than 0.8. Figure 3.17 shows that the areas with high frictional heat flux are under high contact pressures and have the low average density. Dry contacts are more likely to occur in low average density regions than in high average density regions due to existence of more air streamers in low average density regions. Thus, high contact pressures in low average density regions result in high frictional heat flux.

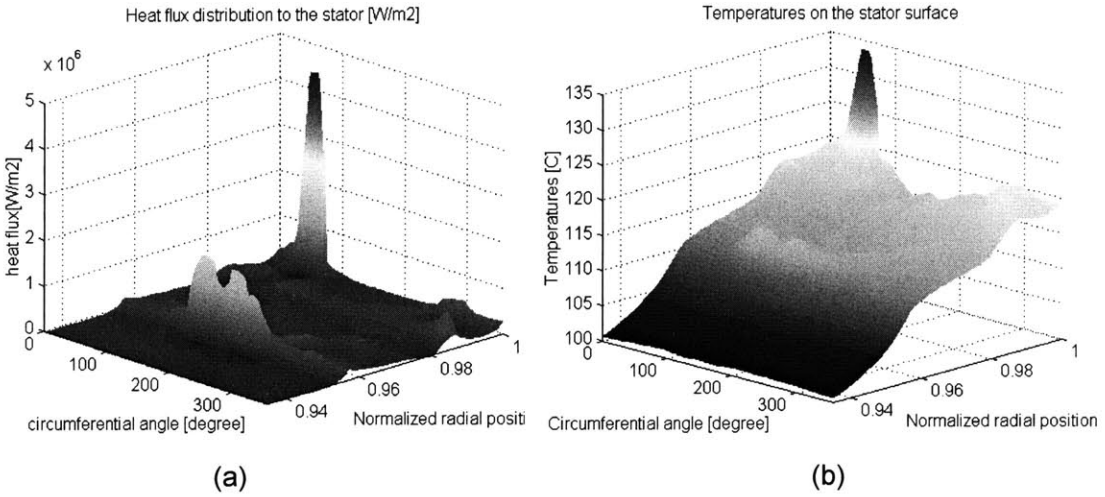

Figure 3.16 Distribution of (a) frictional heat flux and (b) temperatures on the stator surface

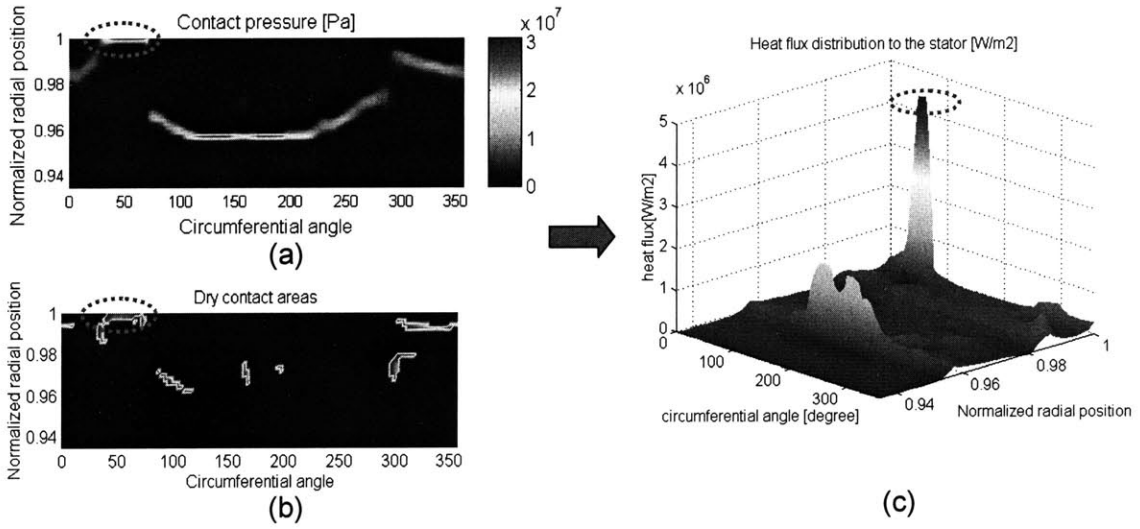

Figure 3.17 High frictional heat regions due to high contact pressures and dry contacts

3.4 Comparisons with experiments

Two measurable quantities from experiments, temperature and friction coefficient with different axial loads are compared with simulation results. The rotating speed increases from zero to 1.8 m/s gradually, then stays at 1.8 m/s until friction and temperature measurements become steady. After measurements, the rotating fixture stops and is cooled down until the whole system reaches to the room temperature. The same procedures are repeated with an increase in the normalized axial load of 0.5.

3.4.1 Comparisons of temperature measurements

Figure 3.18 shows comparisons of T1 (see Figure 3.2) when the axial load increases from 0.5 to 2.5. Note that simulation results overestimate T1 because the 3D thermal model calculates upper bound temperature distribution. Simulation results at the moment of minimum friction underestimate T1. However, differences between simulation results and actual measurements are within reasonable ranges with good agreements in trends.

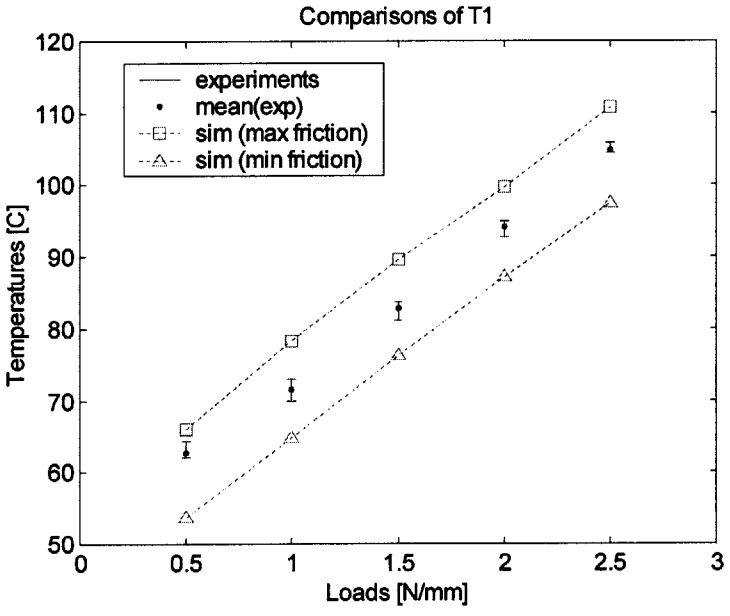

Figure 3.18 Comparisons of T1

Circumferential temperature variations of T1 are also compared as shown in Figure 3.19. Recall that the 3D model overestimates circumferential temperature variations due to steady contact patterns and frictional heat flux while contact patterns change for each rotation step. Such unsteady contact patterns during the rotation tend to distribute frictional heat flux so that decrease circumferential temperature variations, which are not considered in the 3D thermal model. Despite of these factors, simulation results give reasonable agreements and trends.

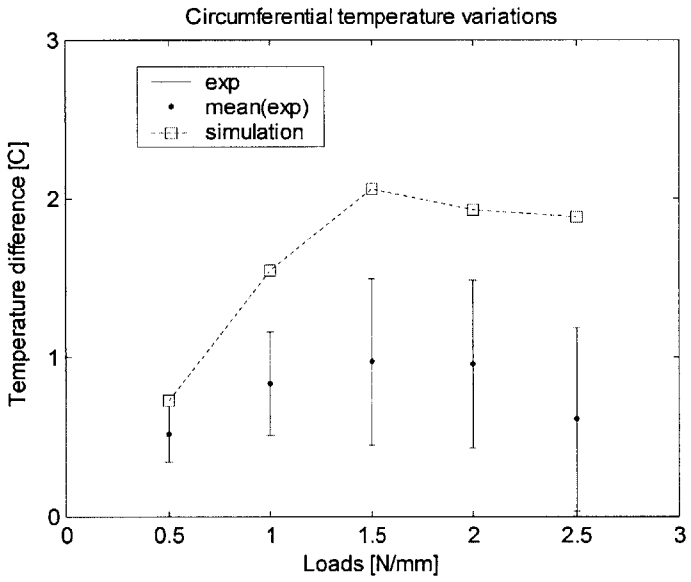

Figure 3.19 Circumferential temperature variations of T1

3.4.2 Comparisons of friction coefficients

Comparisons of friction coefficients are shown in Figure 3.20. Recall that friction coefficients vary during the rotation due to changes of contact areas and cavitation regions. Friction coefficients shown in Figure 3.20 are averaged during one revolution. Note that estimation of the boundary friction coefficient (f_b) is necessary to calculate friction coefficients. The minimum friction coefficient from experiments at low speeds is

used for the estimated value of f_b (See Figure 3.20). Averaged friction coefficients with changes of axial loads also show good agreements with measurements.

Figure 3.21 (a) shows each friction coefficient from three different friction sources, viscous shearing of the lubricant, boundary friction, and dry friction. From Figure 3.21 (a), it is clear that the changes of total friction coefficients with increasing load are mainly due to the changes of the friction coefficients from viscous shearing of the lubricant. As the axial load increases, temperatures of the lubricant film increase and reduce the viscosity of the lubricant. Thus, the friction coefficients from viscous shearing decrease and result in reductions of the total friction coefficients with an increase in the axial load. The ratios of each friction coefficient to the total friction coefficients are shown in Figure 3.21 (b).

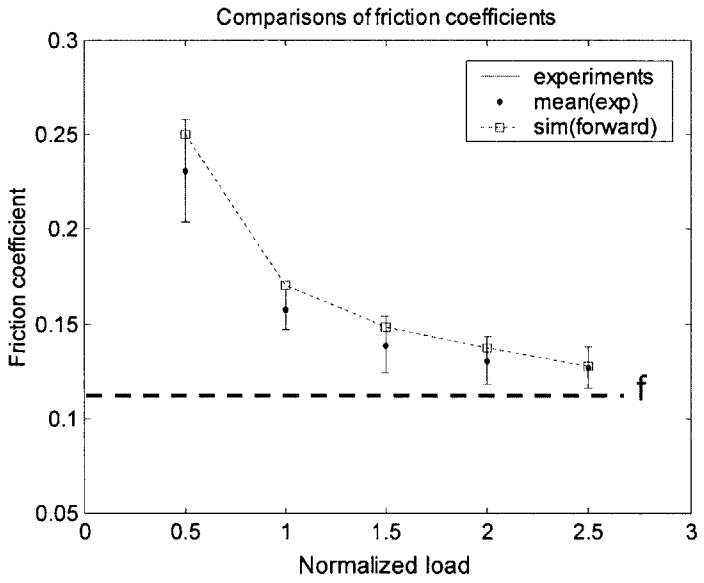

Figure 3.20 Comparisons of friction coefficients

Recall that the 3D contact model assumes the hydrodynamic force generated from the lubricant is negligible. Thus all axial support loads come from contacts between two seal surfaces. In other words, current metal to metal face seals operate in the boundary lubrication regime, where hydrodynamic effects on load support are negligible. Good agreements strongly support the underlying assumption. This fact is important because

the scoring failure mechanisms discussed in section 1.2.2 are valid in the boundary lubrication regime where hydrodynamic lubrication film breaks down [5].

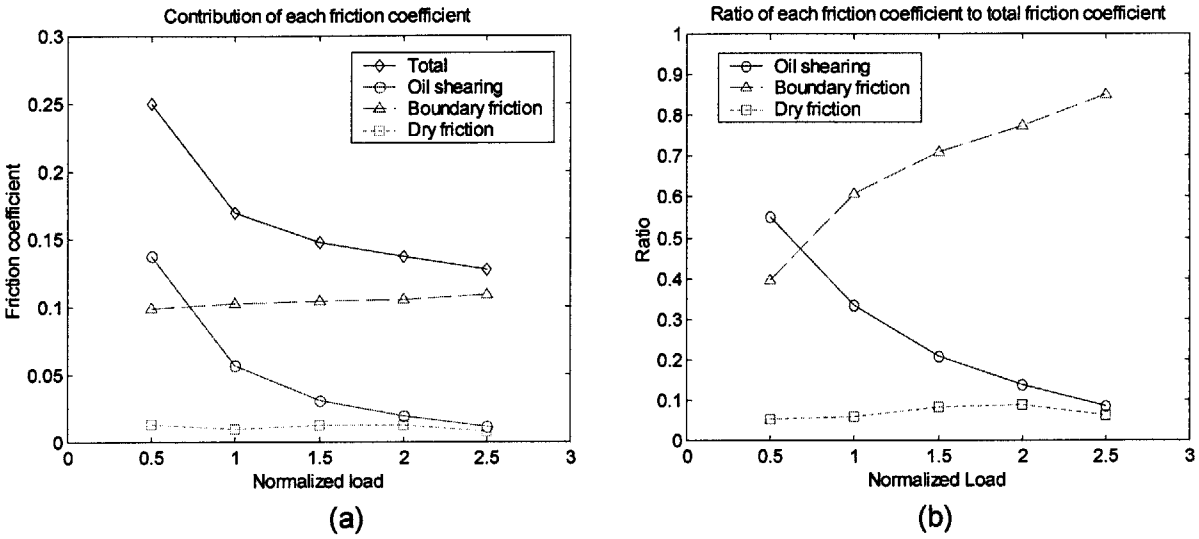

Figure 3.21 (a) Friction coefficient of each friction source (b) Ratio of contribution of each friction source to the total friction coefficient

To confirm the assumption of boundary lubrication, hydrodynamic lift forces with corresponding axial loads are shown in Figure 3.22. Figure 3.22 shows that hydrodynamic lift forces are negligible compared to total axial loads over a whole range of axial loads. Typical normalized axial loads range from 1.0 to 1.5, thus hydrodynamic lift forces are negligible under typical loading conditions.

It is also shown that hydrodynamic effects decrease with increasing loads. Reduced viscosity of the lubricant due to high temperatures under high loading conditions can explain this. When the axial load increases, total friction and temperatures increase. Reduced viscosity due to high temperature leads to a reduction in the magnitudes of hydrodynamic pressures. Figure 3.23 (a) and (b) show the pressure distribution of the lubricant at the sealing band under the normalized axial loads of 0.5 and 2.5, respectively. Thus, the assumption of the boundary lubrication would fit better for high loading conditions. Such trends are also shown in Figure 3.20, in which friction coefficients from simulations approach closer to the means of measured friction coefficients with increases of axial loads.

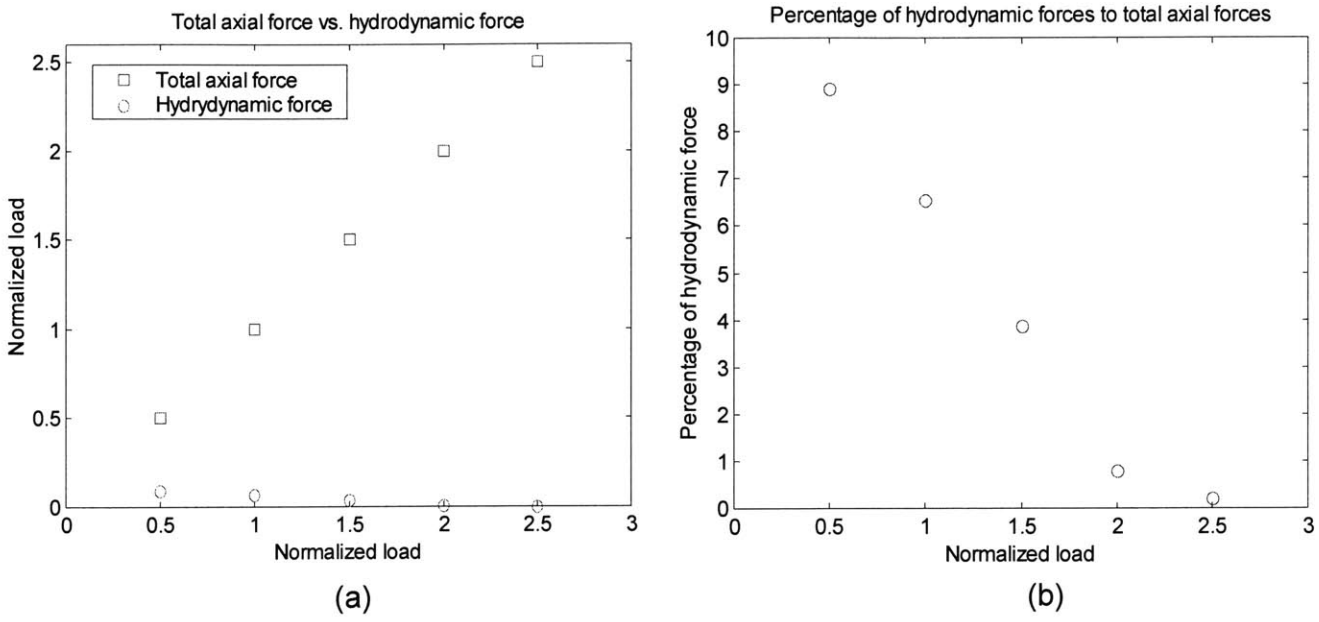

Figure 3.22 Comparisons of hydrodynamic force with total axial force

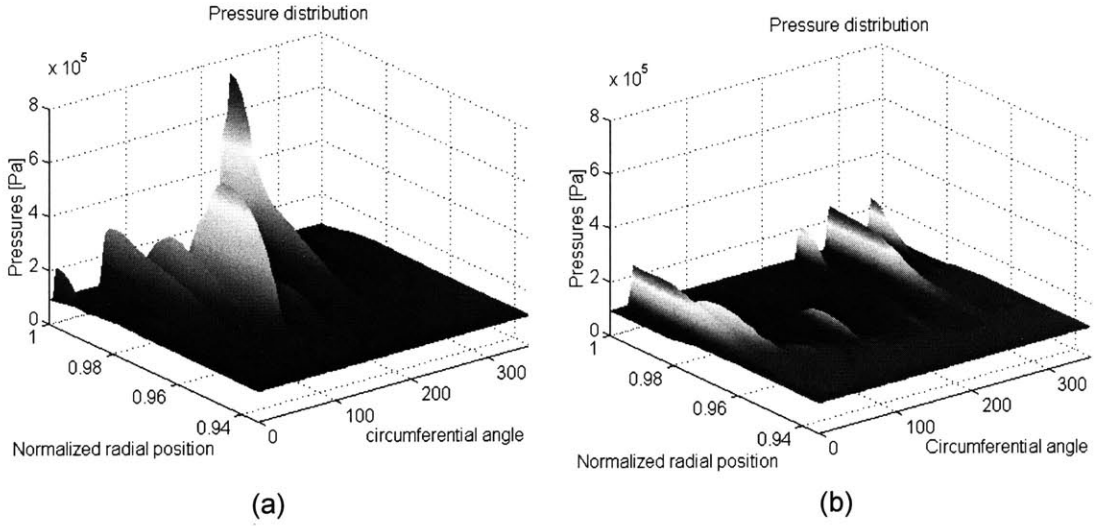

Figure 3.23 Pressure distribution of the lubricant at the sealing band under the normalized load of (a) 0.5 and (b) 2.5

3.4.3 Effects of heat transfer coefficients

The effects of heat transfer coefficients on temperature changes of T1 are shown in Figure 3.24. With 200% of the calculated heat transfer coefficients, predictions of T1 underestimate temperatures for high loads. Even for lower loads, predictions are considered to be low because the thermal model calculates the upper bound temperature distribution. On the other hand, predictions with 50% of heat transfer coefficients show overestimations of T1 as well as faster increase rates. Comparisons show that predictions with original heat transfer coefficients give the best results. Also note that differences within 10% of heat transfer coefficients would not significantly affect temperature calculations. These results show not only that estimations of heat transfer coefficients are accurate enough, but also that current models can tolerate small errors in calculations of heat transfer coefficients.

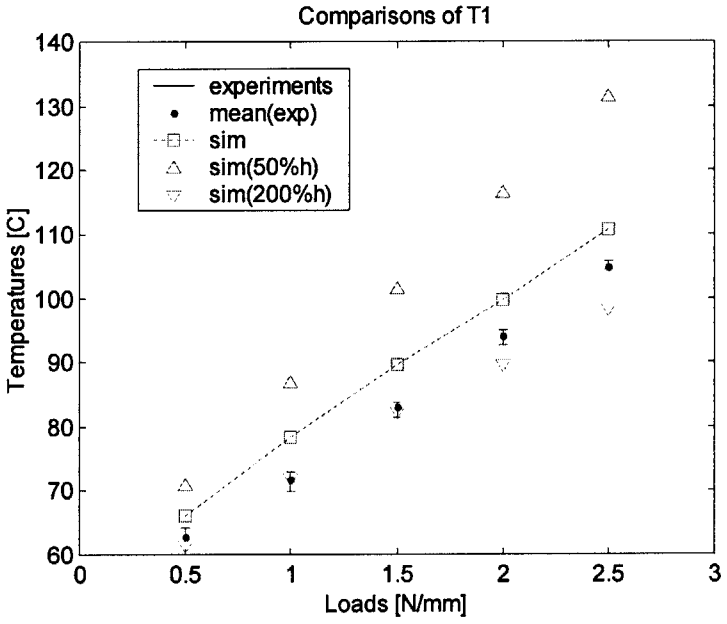

Figure 3.24 Effects of heat transfer coefficients on T1

4 Application to failure tests

Numerical models have been developed and validated by comparisons with experiments in previous chapters. In this chapter, numerical models were applied to scoring failure tests to find important factors affecting scoring failures. In addition, a new scoring failure criterion based on the distribution of nominal temperatures and frictional heat flux was proposed. Numerical results with new scoring failure criterion predict the likelihood of scoring failures under certain operating conditions. Physical explanations for different scoring failures are also investigated.

4.1 Scoring failure tests

Scoring failure tests for ten different seal pairs have been done at the laboratory of the project sponsor. The procedures of failure tests are as follows. First, the seal pair is inserted into the fixture. The gaps between the fixtures are held constant for all seal pairs. The initial axial load is recorded before starting rotation. The initial rotating speed is 50 rpm and continues for 4 minutes, then stops for 1 minute. Then, the rotor starts to rotate at 50 rpm in the reverse direction for another 4 minutes followed by 1 minute stop. These procedures are repeated with increase of 50 rpm until scoring failure occurs. When scoring failure occurs, the load and the speed at failure are recorded.

4.2 Simulation procedures

Ten different seal pairs with different scoring failure operating conditions have been selected (see Table 4-1). Table 4-1 shows wide distribution of failure speeds with the same normalized axial load, 1.46[4]. In reality, the axial load varies slightly and the failure speeds are recalculated for having the same failure power with the normalized axial loads of 1.46. The failure power values are calculated by multiplying the axial loads by the failure speed.

[4] In this chapter, the axial loads are normalized by 289 N.

Measured surface profiles are imported after the extrapolations to the numerical models as described in section 2.2. For simulations, three different speeds are selected while maintaining the same axial load: 1.8, 3.8 and 6.2 m/s. Note that each speed is close to the failure speed of the following seal pairs, 1, 4 and 6, respectively. For the speed of 1.8 m/s, all seal pairs are simulated with the axial load of 1.46. On the other hand, only seal pairs with the same as or higher failure speeds than 3.8 m/s, the seal pairs from 4 to 10, are simulated with the same speed of 3.8 m/s and the axial load of 1.46. Similarly, only the seal pairs from 6 to 10 are simulated for the speed of 6.20 m/s.

Number of seal pairs	Failure power [W]	Failure speeds [m/s]
1	158.5	1.81
2	187.2	2.14
3	254.5	2.91
4	334	3.81
5	350.3	4.00
6	544.9	6.22
7	555.5	6.34
8	572.8	6.54
9	602.2	6.87
10	614.4	7.01

Table 4-1 Selected seal pairs with scoring failures

4.3 Scoring failure criterion

Total surface temperatures are important parameters for scoring failures as discussed in section 1.2.2. Furthermore, the nominal temperature and the local temperature rise are comparable for the FMMFS. Thus, scoring failure criterion should include effects of both temperature rises.

From the numerical models, distributions of the nominal temperatures and the heat flux are calculated. If one seal pair has larger areas of high nominal surface temperatures than those of the other seal pair, scoring failure is more likely to occur for the seal pair with more high temperature regions. In other words, the percentage of high temperature

regions under similar operating conditions would be proportional to likelihood of scoring failures.

Using the temperature distribution on the stationary surface at the sealing band, the temperature above which the areas are upper x% of the total areas is defined as $T_{n,x}$, where n is the number of seal pair and x is the upper accumulated percentage of the areas (see Figure 4.1). $T_{n,x}$ for all seal pairs is calculated, then the maximum $T_{n,x}$ among all seal pairs is defined as the critical temperature, $T_{crit,x}$.

High temperature regions (HTR) are defined as the regions whose nominal temperatures on the stationary surface at the sealing band are higher than the critical temperature. Finally, the percentage of high temperature regions of each seal pair is calculated for all seal pairs. The percentage of the HTR for each seal is the same as or smaller than x % because the critical temperature is the maximum $T_{n,x}$. Three different percentages of the HTR are used, 3%, 5% and 10%.

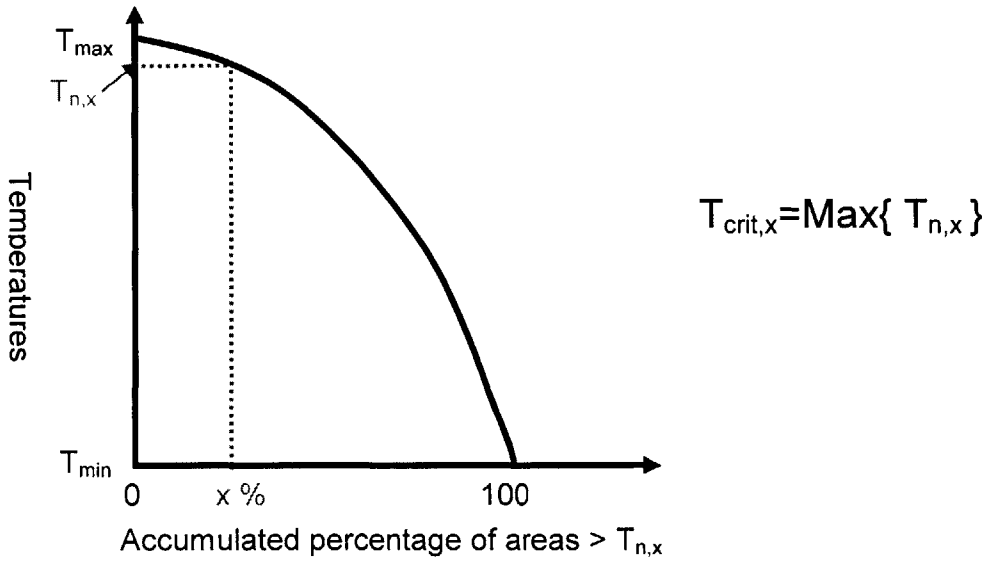

Figure 4.1 Definitions of $T_{n,x}$ and $T_{crit,x}$

The local temperature rise will be proportional to the magnitude of the local heat flux when the seal surfaces have similar roughness. The magnitude of the local heat flux is therefore the measure of the local temperature rise. The heat flux magnitude of the HTR for each seal pair are averaged and used as the measure of the local temperature rise over the HTR.

Considering the percentage and the averaged heat flux magnitude of the HTR, a scoring value for each seal pair is defined as,

Scoring Value = [% of the HTR] [average heat flux over the HTR] .

After calculations of scoring values of all seal pairs, a scoring probability is expressed as,

$$(Scoring\ probability)_i = \frac{(Scroing\ value)_i}{\sum_{i=1}^{n}(Scoring\ value)_i}$$

where n is the total number of seal pairs.

With simulation results, the scoring probabilities of all seal pairs at the given speed and axial load are compared in the next section.

4.4 Results

All ten seal pairs are simulated with the speed of 1.80 m/s and the axial load of 1.46. The scoring probabilities of all seal pairs are shown in Figure 4.2. The vertical axis represents the scoring failure probability of each seal pair while the horizontal axis represents corresponding seal pair. The scoring probability is the highest for the seal pair 1 whose failure speed is the closest to the simulated speed, 1.80 m/s (see Table 4-1). This result is same when the percentage of high temperature regions is changed as 10%, 5% and 3%.

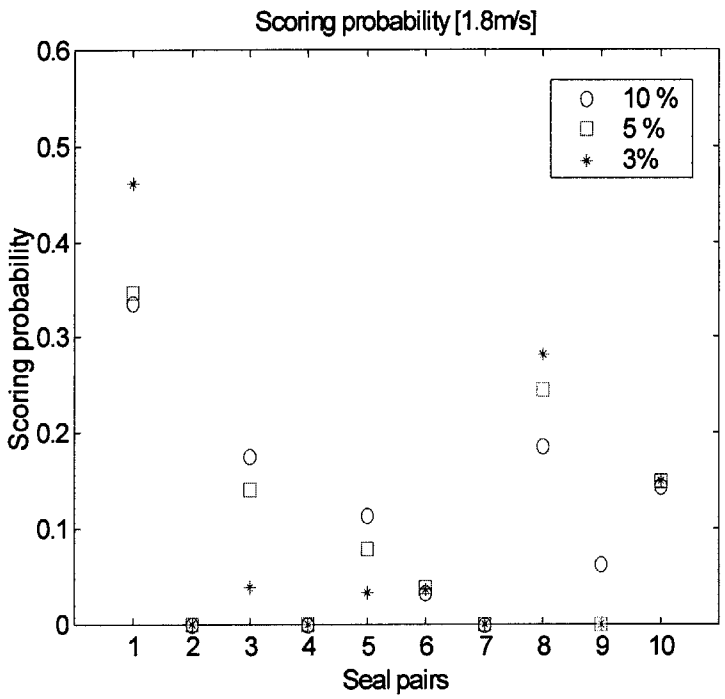

Figure 4.2 Scoring probability for 1.8 m/s

For the speed of 3.80 m/s, only seal pairs whose failure speeds are the same as or higher than 3.80 m/s are simulated. The seal pairs with lower failure speeds are assumed to have scoring failures already. As a result, the numerical models compute for only seven pairs except the seal pairs of 1, 2 and 3. Same procedures and assumptions are repeated for the speed of 6.20 m/s. The plots of scoring probability for 3.80 and 6.20 m/s are shown in Figure 4.3 and 4.4, respectively.

Figure 4.3 and 4.4 show that scoring probabilities are maximum for the seal pairs whose failure speeds correspond to the simulated speeds (see Table 4-1). In other words, the scoring failure is most likely to occur for the seal pair with the same scoring failure speed as the simulated speed. From these results, it is clear that the current numerical model and the scoring failure criterion capture the fundamental physics underlying scoring failures. The next step is to investigate the results from the numerical model and explain the important features which lead to different scoring failure speeds.

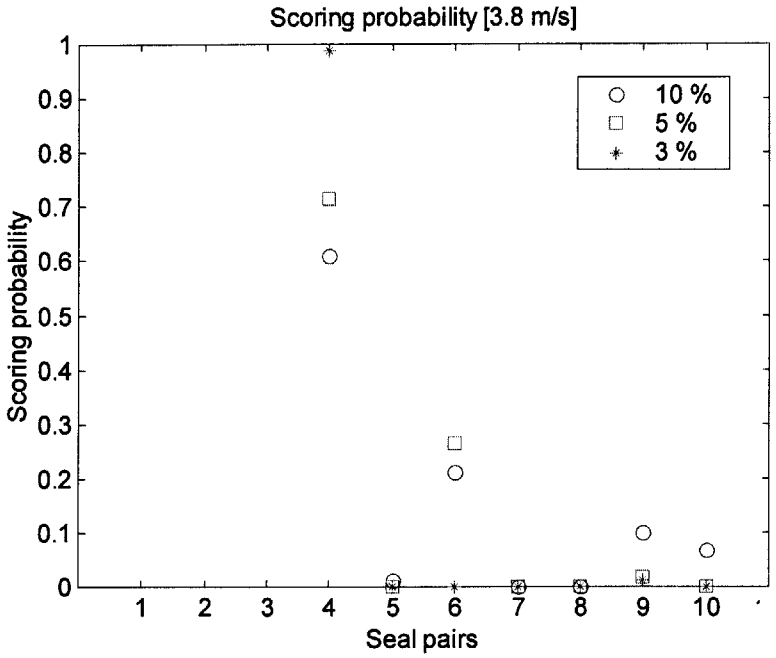

Figure 4.3 Scoring probability for 3.8 m/s

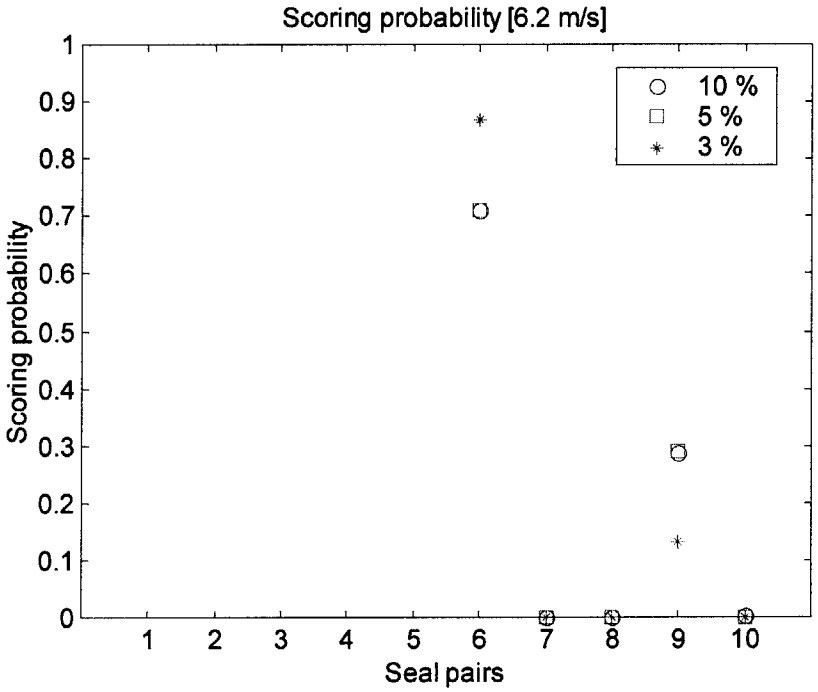

Figure 4.4 Scoring probability for 6.2 m/s

4.5 Physical explanations for different scoring failures

4.5.1 Comparisons of two seal pairs for the low speed (1.8 m/s)

Two different seal pairs have been chosen from the numerical results at the speed of 1.8 m/s for more in depth analysis. The chosen pairs at 1.8 m/s are shown in Table 4-2. Note that failure speed is much higher for seal pair 1 than for seal pair 8. Calculated surface temperatures of the stationary seal of each seal pair is shown in Figure 4.5.

Seal pairs [failure speed]	1 [1.80m/s]	8 [6.54m/s]
Total frictional heat to stator [W]	23.7	26.8
% of area where T_{macro} > 120C	3.54	0.79

Table 4-2 Comparisons of two seal pairs at 1.80 m/s

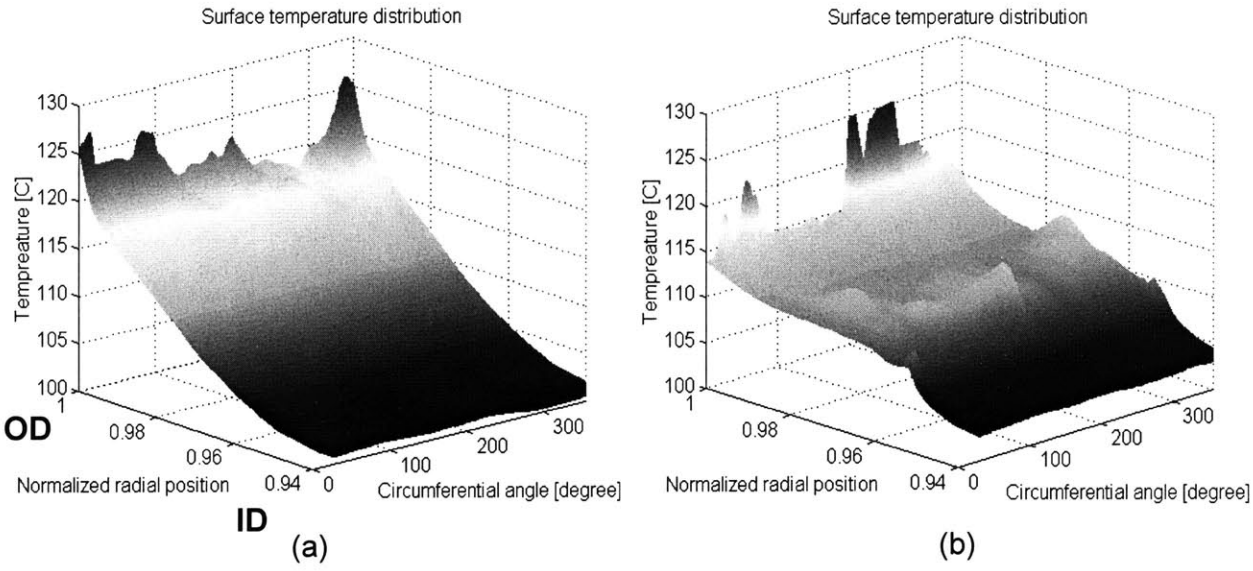

Figure 4.5 Stator surface temperature of the seal pair 1 (left) and 8 (right)

From Table 4-2, the areas whose stator surface temperatures are higher than 120C is larger in seal pair 1 than in seal pair 8, although the amount of total frictional heat into the stationary seal is larger in seal pair 8.

Distributions of heat flux into the stationary seal are investigated to explain this contradiction and shown in Figure 4.6. Note that frictional heat flux for seal pair 1 is concentrated around the outside diameter of the sealing band. On the other hand, heat flux for seal pair 8 are distributed near the inside diameter as well as the outside diameter. Distributions of heat flux are usually similar to those of contact areas because most of frictional heat flux comes from contact pressures. Thus contacts occur near the inside diameter and the outside diameter for the seal pair with higher scoring failure speed, while contact regions are concentrated near the outside diameter for the seal pair with lower scoring failure speed.

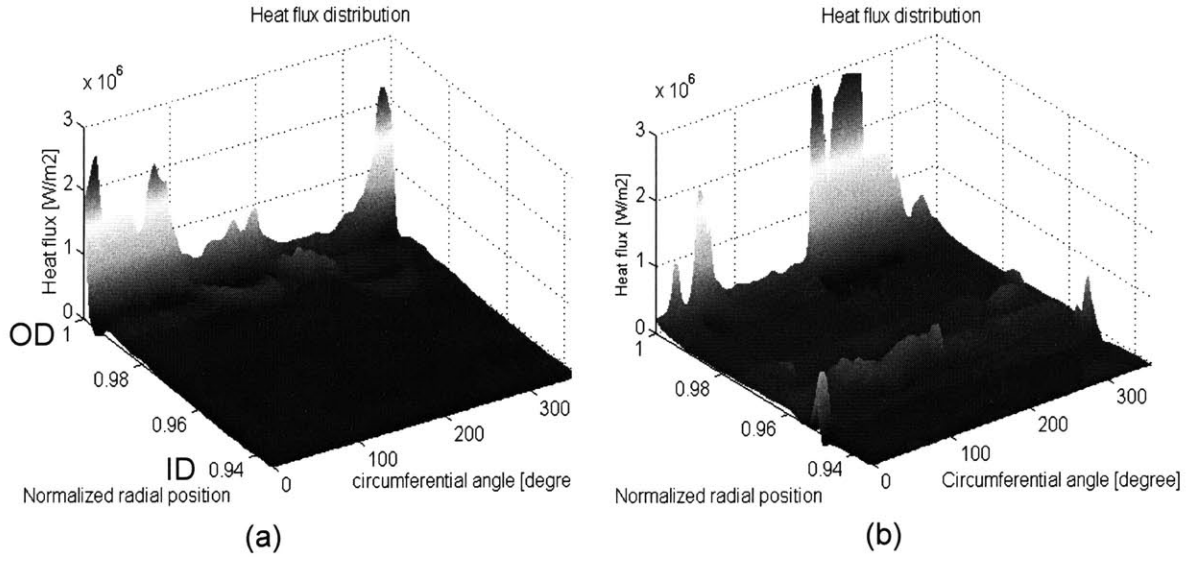

Figure 4.6 Distribution of heat flux into the stator of seal pair 1 (left) and 8 (right)

Surface profiles are investigated to understand different contact patterns under the same operating conditions. Radial surface heights of the rotating and the stationary seal of seal pair 1 and 8 along part of the circumference are shown in Figure 4.7 and Figure 4.8, respectively. Differences in radial profiles are clear. The radial surface heights of the rotating seal of pair 8 (see Figure 4.8 (a)) show significant variations in surface heights, especially near the starts of the curvature. These variations can lead to contacts near the inside diameter while contacts near the outside diameter occur in the other regions. On the contrary, radial surface heights of the stationary seal of seal pair 1 (see Figure 4.7 (b)) show small variations near the outside diameter without any significant variations near the starts of the curvatures. In this case, all contacts would occur near the outside diameter. In summary, different radial surface heights can create different contact patterns and frictional heat flux, and eventually lead to seemingly contradictory temperature distributions.

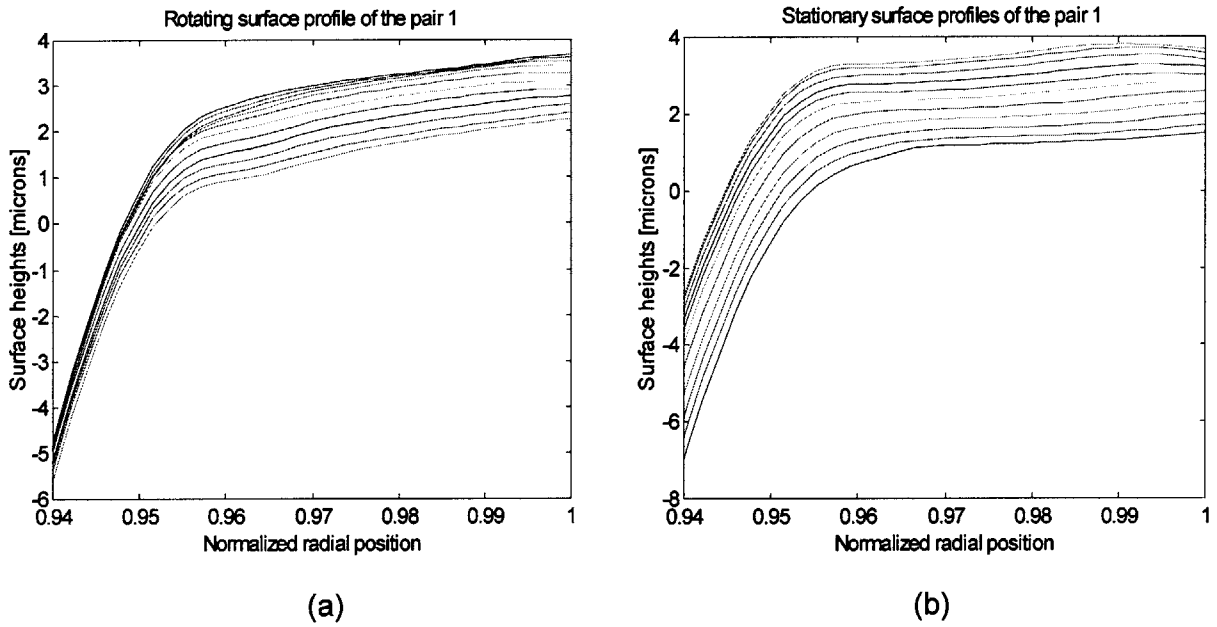

Figure 4.7 Radial surface profiles of (a) the rotating and (b) the stationary seal of pair 1

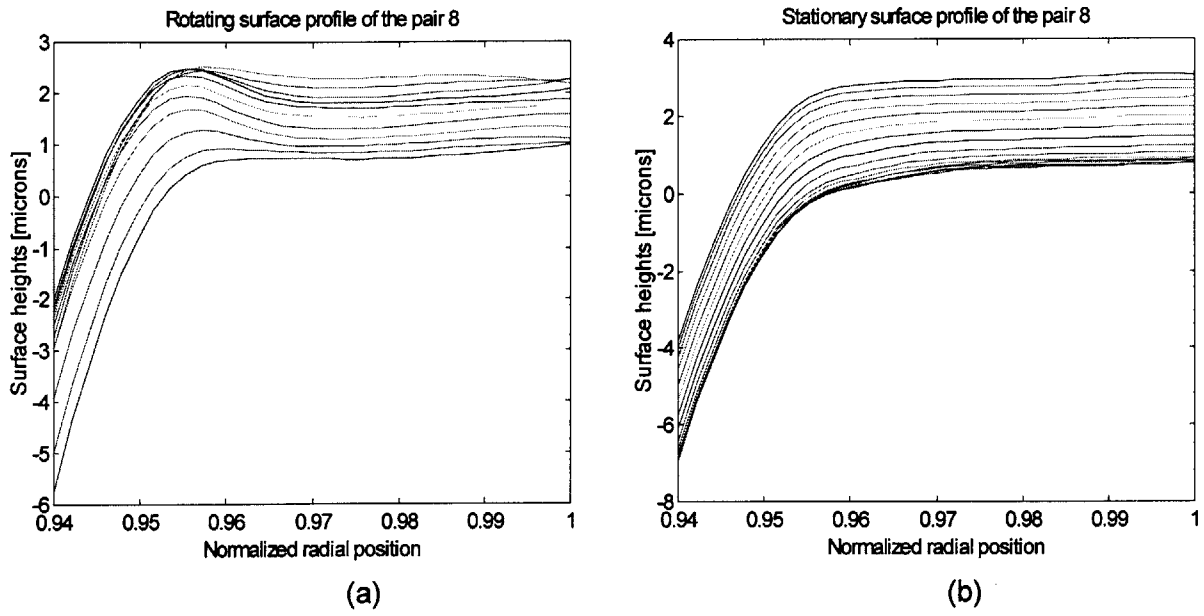

Figure 4.8 Radial surface profiles of (a) the rotating and (b) the stationary seal of pair 8

Effects of different heat flux distributions on temperature distributions are shown in Figure 4.9. Each solid curve represents the temperature distribution due to each unit of heat flux indicated by an arrow. These temperature distributions are superposed for calculations of total temperature distributions due to all heat fluxes. Total temperature distributions after superposition are shown in the below figure as dashed lines for the concentrated (see Figure 4.9 (a)) and the distributed heat flux distributions (see Figure 4.9 (b)). Due to the effects of superposition, more high temperature regions exist for more concentrated heat flux distributions. On the contrary, discontinuous contact patterns contribute to distributions of frictional heat flux and eventually lead to reductions in high temperature areas.

Moreover, discontinuous contact patterns reduce thermal paths to the inside oil flows. It is known that more than 60 % of the total frictional heat is transferred to the inside oil flows. For seal pairs 1 and 8, the contact positions are averaged along the circumference. These averaged contact positions, the radial distance from the inside seal surface to the averaged contact position at the sealing interface (L_{avg} in Figure 4.10), are 8.7 mm and 7.8 mm for seal pair 1 and 8, respectively. Thus, thermal paths for frictional

heat transfer to the inside oil flows are shorter for seal pair 8. Shorter thermal paths reduce the conduction thermal resistance so that temperatures on the sealing interface decrease.

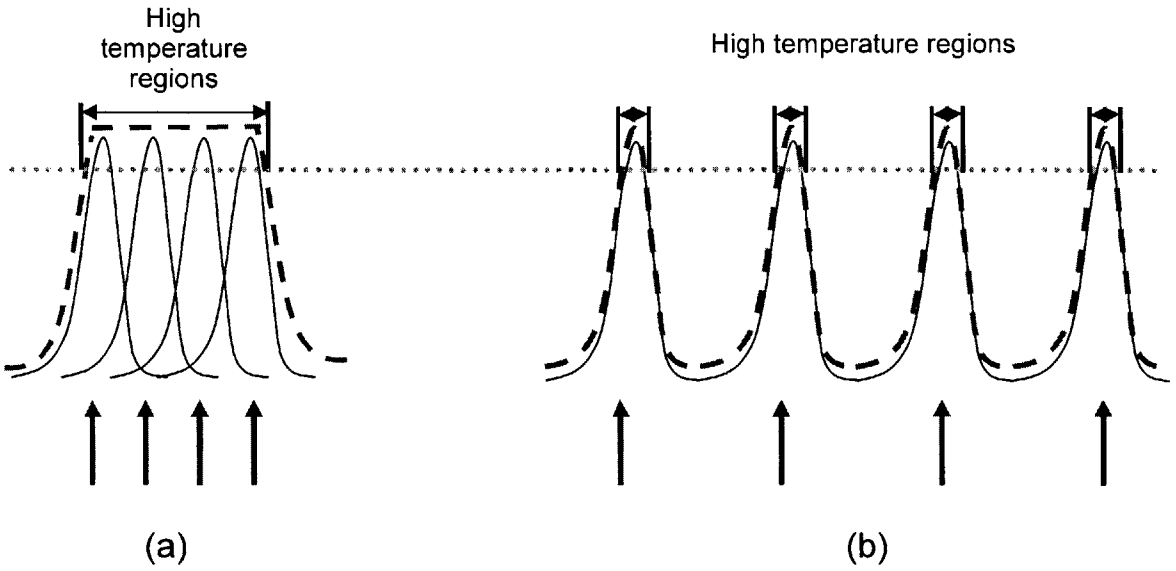

Figure 4.9 Effects of heat flux distributions on temperatures

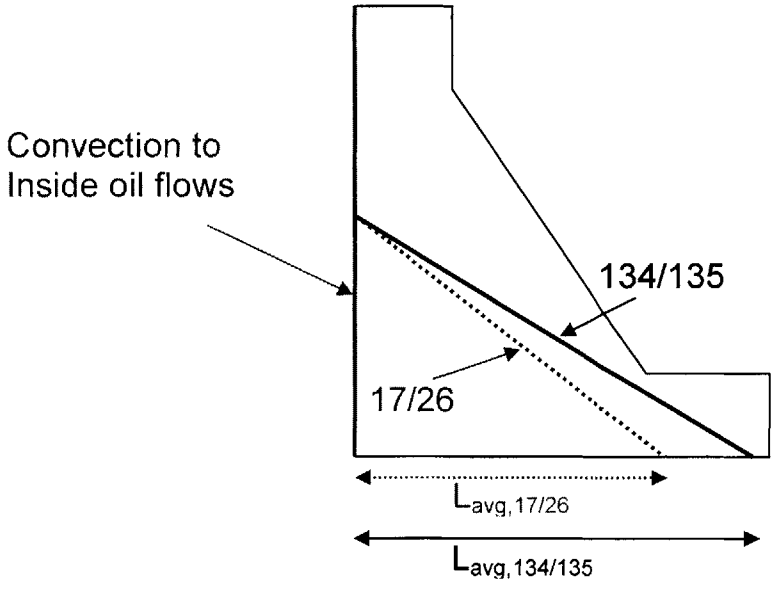

Figure 4.10 Comparisons of thermal paths for two seal pairs

4.5.2 Comparisons of two seal pairs for the high speed (6.2 m/s)

Two different seal pairs have been chosen from the numerical results at the speed of 6.2 m/s. Two chosen pairs simulated with this speed are shown in Table 4-3. The failure speed is higher for seal pair 10 than that for seal pair 6. Note that the magnitude of the total heat flux to the stator is similar for both seal pairs. However, surface temperatures on the stationary seal surface of each seal pair in Figure 4.11 show that high temperature regions are much larger for seal pair 6, whose failure speed corresponds to the simulated speed. On the other hand, discontinuity of temperature distributions is clearly noticeable for seal pair 10.

Seal pairs [failure speed]	6 [6.20 m/s]	10 [7.01m/s]
Total frictional heat to stator [W]	163.9	163.7
% of area where T_{macro} > 180C	11.9	0.30

Table 4-3 Comparisons of two seal pairs at 6.2m/s

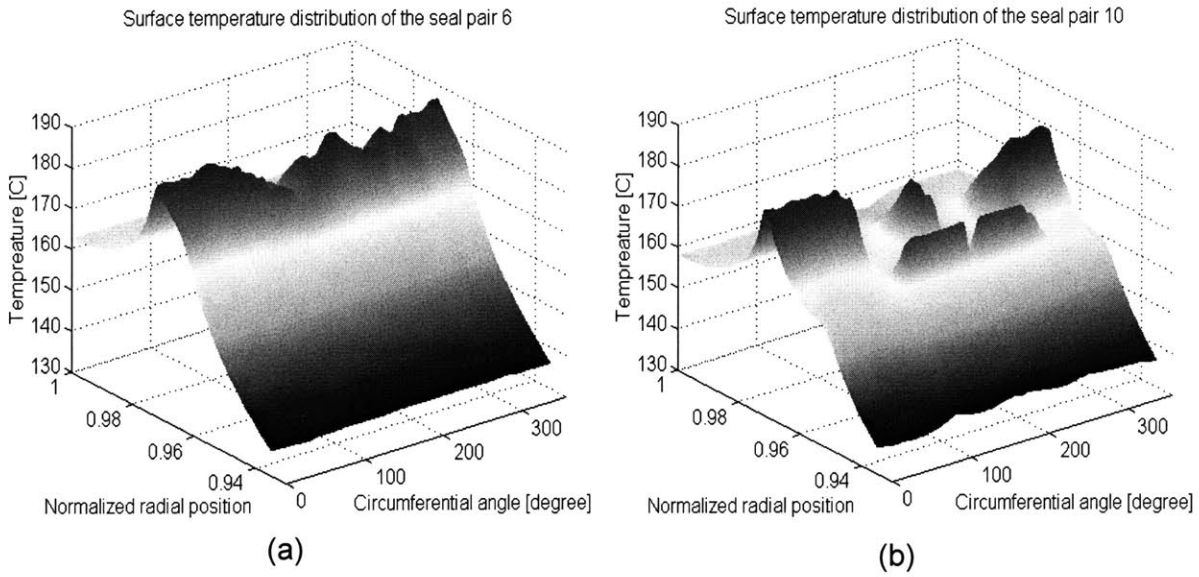

Figure 4.11 Stator surface temperatures of seal pair (a) 6 and (b) 10

Distributions of heat flux into the stator are investigated and shown Figure 4.12. It is clear that heat flux distributions of seal pair 6 are more concentrated and continuous (see Figure 4.12 (a)). On the contrary, discontinuities in temperature distributions of seal pair 10 come from discontinuities in heat flux distributions. These discontinuities can reduce high temperature regions for seal pair 10 as discussed in the previous section. Additionally, the averaged contact length of seal pair 10 is 0.3 mm shorter than for seal pair 6. Shorter thermal paths can also contribute to lower temperature distributions.

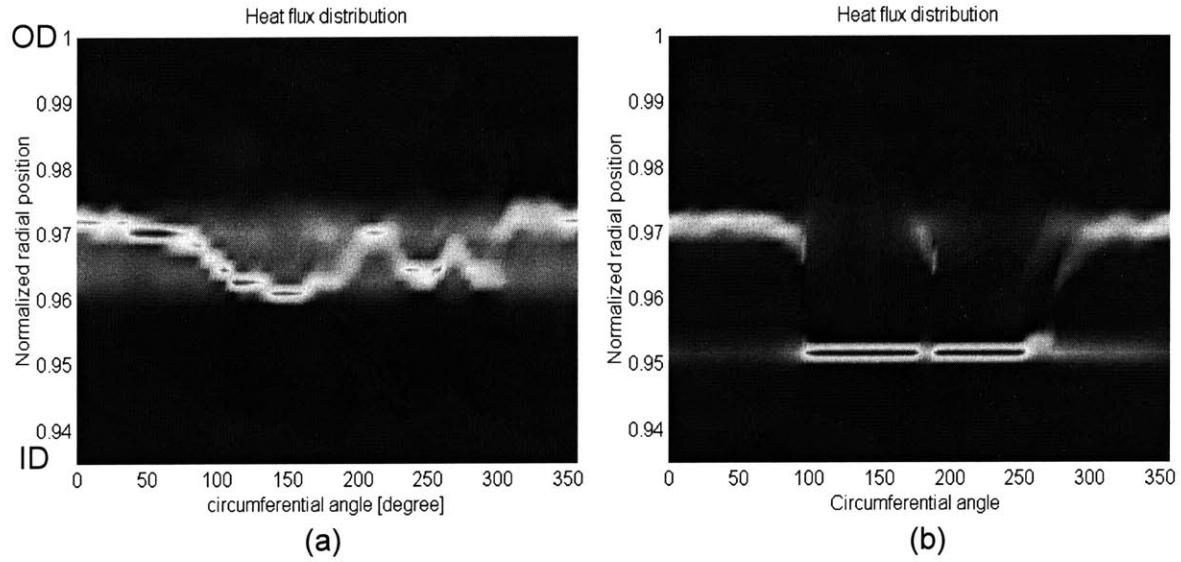

Figure 4.12 Distributions of heat flux into the stationary seal of seal pair (a) 6 and (b) 10

To understand different contact patterns, radial surface profiles of the stationary seal of each seal pair along the circumference are compared in Figure 4.13. Notice differences in the starts of the curvatures for both seals. Circumferential variations in the starts of the curvatures show wider distributions for the stationary seal of pair 10 (see Figure 4.13 (b)).

Under the high operating speed, thermal twist angles due to thermal gradients increase. With increases of twist angles, contact regions gradually move radially inward. Once contact regions reach to the starts of the curvatures, contact regions move inward at

a slower rate with same increases of twist angles due to increased gap heights between the surfaces. Finally, different starts of the curvatures can lead to discontinuous contact patterns with sufficiently high twist angles. Also note the surface heights in the transition regions rather than those in the flat band become important for high speed with high twist angles.

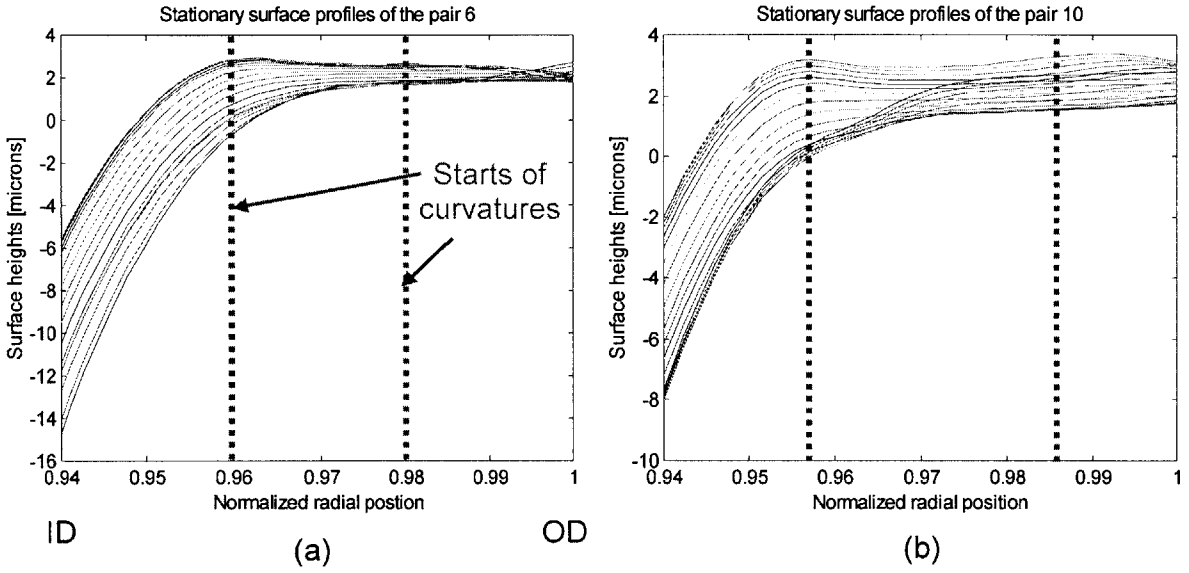

Figure 4.13 Radial surface heights of the stationary seal of pair (a) 6 and (b) 10

4.6 Summary of scoring failure tests

From comparisons of seal pairs with low and high scoring failure speed, it has been shown that discontinuous contact patterns play an important role in reducing surface temperatures. Discontinuous contact patterns distribute frictional heat flux as well as reduce the conduction thermal resistance due to shorter conduction thermal paths. Distributed heat flux can reduce surface temperatures from less superposition effects of temperatures.

Surface profiles are investigated to understand different contact patterns for low and high operating speeds. Two important geometric features, radial variations in surface heights and the starts of the curvatures, can explain different contact patterns under the same operating conditions for low and high speed, respectively.

5 Concluding remarks

5.1 Summary

Numerical models have been developed to explain the different scoring failure resistances of FMMFS. The seal which is investigated in this thesis has unique features, such as much more flexibility in the circumferential direction than in the radial direction, identical rotating and stationary seals, and a loading mechanism using elastomeric rings. Despite of its wide range of applications, this type of mechanical face seal has never been investigated before.

On the other hand, existing failure criteria for other type of mechanical face seals are inadequate for the FMMFS. Thus, a new scoring failure criterion is necessary. The new scoring failure criterion needs to consider both the nominal and the local temperatures because they are comparable during normal operating conditions.

The main difficulties for numerical models of the FMMFS result from expensive computation costs. For accurate temperature predictions, interactions among seal surface deflections, lubrication in the sealing band, and thermal effects need to be coupled. Furthermore, these interactions are inherently unsteady due to identical rotating and stationary seals. This thesis work is the first attempt to develop numerical models considering all these interactions and to predict scoring failures using numerical results for the FMMFS.

To manage computation costs and capture underlying physics, the following simplifications are made using special features of the FMMFS: circumferential rigidity in the contact model, hydrodynamic effects in the cavitation model, and circumferential temperature variations of the rotating seal surface in the thermal model are all assumed to be negligible. All of these simplifications are validated from scaling arguments and comparisons with experiments. Currently, the numerical models can generate useful information to evaluate the seal performance including temperatures, friction coefficients, contact pressures, final gap heights, and cavitation regions without empirical inputs. It should be also noted that real seal surfaces can be imported to the numerical models, and

heat transfer coefficients for convection to the surrounding oil flows can be calculated with a commercial finite element package.

Combined with the numerical results, the new scoring failure criterion has been suggested and applied to real scoring failure tests. This scoring failure criterion can predict likelihood of scoring failures for each seal pair at given load and speed successfully. From the scoring failure experiments, the scoring probability of the seal pair whose failure speed corresponds to the simulation speed is much higher than that of other seal pairs.

5.2 Conclusions

Currently, complete numerical models are available. Numerical models can import real seal surface profiles and calculate deformed gap heights, oil distributions, friction coefficients and temperatures without empirical inputs. Heat transfer coefficients as convection boundary conditions of the thermal model can be obtained from simulations. Comparisons with experimental measurements and scoring failure tests show that numerical models capture governing physics with simplifications from distinct features of the FMMFS.

From this thesis work, it also has been shown that the FMMFS operates in the boundary lubrication regime over a wide range of operating conditions including typical loading conditions. The hydrodynamic effects due to the circumferential waviness have been questionable, but here are proved to be negligible for current FMMFS.

Most importantly, the geometrical features which affect the scoring failures are found using the results from the numerical models. Radial variations in the seal surface heights and the different starts of the curvatures can reduce high temperature regions due to discontinuous contact patterns and shortened conduction thermal paths. It also has been shown that different regions of the seal surface are important according to operating conditions. For instance, the surface profiles near the curvature regions are important at high speeds at the same vertical loads, while those near the outside diameter become significant at low speeds.

Finally, new scoring failure criterion using numerical results predicts the likelihood of scoring probability successfully. One-value criteria, critical temperature and frictional power intensity, failed to predict scoring failures for the FMMFS. The new scoring failure criterion uses two values which are measures of nominal and local temperatures, thus considers both temperature effects. This new scoring failure criterion can be used in general applications, for instance, moderate or high frictions with finite dimensions of sliding bodies.

5.3 Suggestions for future works

Current numerical models include the quasi-steady lubrication model and assume that the lubricant spreading on the whole sealing band reaches the steady state. In reality, the lubricant penetrates from the inside to the outside diameter until it spreads onto whole sealing band. Even after that, the lubricant flows would be unsteady considering the squeezing effects due to changes of the gap heights during the rotation. The unsteady model of lubricant flows is important for both kinds of seal failure modes, leakage failures and scoring failures.

For the leakage failures, the unsteady flow model can show differences in oil leakage among different seal pairs. Thus, the unsteady flow model of the lubricant is necessary for finding the critical parameters of excessive leakage failure. The new failure criterion for leakage failure needs to be developed with the unsteady flow model.

The unsteady flow model can also contribute to further development of current numerical models for scoring failure predictions. First, the unsteady flow model may calculate cavitation regions more accurately than the quasi-steady cavitation model. By comparing results from the unsteady model, calculations of the cavitation regions from the current quasi-steady model can be justified or improved. Moreover, accurate calculations of the cavitation regions will lead to better estimations of the distribution of frictional heat flux and temperatures.

Secondly, better estimations of the distribution of frictional heat flux from the unsteady flow model can provide the numerical tools to reduce total friction at the sealing interface for seal designers. This thesis work focused on distributing the frictional heat flux rather than reducing total friction. If calculations of the frictional heat become more accurate, the surface profiles which reduce the total friction can be investigated with the numerical model and the surface generator. Reducing the total friction will require decreases of dry contact areas. Less cavitation can be beneficial to reducing the risk of the dry contacts. However, less cavitation also means ineffective oil transport into the sealing band because low pressure regions in the cavitation areas act as the sinks of the lubricant. Ineffective oil transport into the sealing areas leads to poor lubrication, high total friction and eventually early scoring failures. Such tradeoff of cavitation effects to

reduce the total friction generation requires further investigations with accurate estimations of the frictional heat flux. Once critical features that control the cavitation effects are found, the seal designer can delay scoring failures by reducing total friction as well as distributing frictional heat flux.

Finally, the unsteady flow model can consider the effects of other important parameters besides total surface temperatures on scoring failures. It is known that one of the scoring failure mechanisms, the catalytic decomposition of the lubricant, strongly depends on the supply of the fresh lubricant. If the degraded lubricant is replenished with the fresh lubricant, the lubricant will maintain its lubrication capacity. Thus, the replenishment rate of the fresh lubricant would be another important parameter of scoring failures. The unsteady flow model can provide realistic information about the replenishment rate of the fresh lubricant over the possible scoring failure regions.

Appendix

A. Estimations of the local temperature rise

As written in chapter 1, most of the thermal models that predict scoring failures only calculate of the local temperature rise. This assumption is valid when the nominal temperature rise is relatively low due to the large heat capacity of sliding bodies and relatively low total friction. However, this assumption is questionable in the case of FMMFS. Thus, it is necessary to check the assumption by estimating the local temperature rise for further investigations.

Two numerical models have been developed to estimate the local temperature distributions. The first model is an asperity contact model between two rough surfaces. This model calculates real contacts areas, contact pressures, and final gap heights. Using the results from the asperity contacts model, the distribution of local heat flux is calculated. The distribution of local heat flux changes with time when the one rough surface slides over the other rough surface. The second model calculates the local temperature distributions with time-varying local heat flux distribution.

a. Asperity contacts model

Extensive research has been conducted on the contact of real surfaces by tribology researchers. In early studies, stochastic models were developed based on the following assumptions [29, 30]: the summits of asperities which are approximated as quadratic curves, no interactions between asperities, elastic deformation of asperities, and some regular statistical distributions of asperities. These stochastic models provide important information for the relationships among load, mean separation gaps, and real contact areas. However, the above assumptions are questionable for dealing with real rough surfaces.

On the other hand, the development of numerical capacity and techniques makes the full numerical simulation of contacts between real rough surfaces possible. For our

purpose, the numerical scheme based on the work of Ju and Zheng [31] has been developed with a consideration of plasticity effects.

Figure A shows two contacting bodies before and after deformation. The w_i represents vertical elastic deformation of the body i. From the Boussinesq solution, the w_i due to applied pressure distribution can be expressed as,

$$w_i(x,y)=\frac{1-\mu_i^2}{\pi E_i}\iint_A \frac{p(\xi,\eta)\,d\xi\,d\eta}{\left[(x-\xi)^2+(y-\eta)^2\right]^{1/2}}\ .$$

In the contact regions, $w_1(x,y)+w_2(x,y)=\delta(x,y)$. Thus,

$$K\iint_{Ar} \frac{p(\xi,\eta)\,d\xi\,d\eta}{\left[(x-\xi)^2+(y-\eta)^2\right]^{1/2}}=\delta(x,y)\,,$$

where the parameter K is defined as

$$K=\frac{1-\mu_1^2}{\pi E_1}+\frac{1-\mu_2^2}{\pi E_2}\,.$$

If the real contact areas are discretized into M contacting elements, the previous equation can be written as,

$$K\sum_{j=1}^{M} p_j \iint_{Aj} \frac{d\xi\,d\eta}{[(x-\xi)^2+(y-\eta)^2]^{1/2}}=\delta_i \qquad \text{(i, j = 1, 2, ..., M).}$$

This equation can be rewritten as,

$$\sum_{j=1}^{M} B_{ij}\,P_j=\delta_i \ \text{ where } \ B_{ij}=K\iint_{Aj}\frac{d\xi\,d\eta}{[(x-\xi)^2+(y-\eta)^2]^{1/2}}\ .$$

The coefficient B_{ij} characterize the vertical displacement of the element i due to a unit pressure applied on the element j.

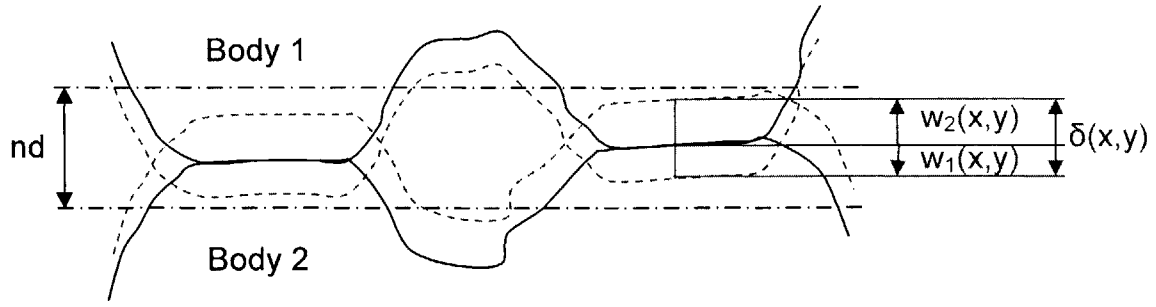

Figure A. Contacting rough surfaces before (dash) and after (solid) deformation

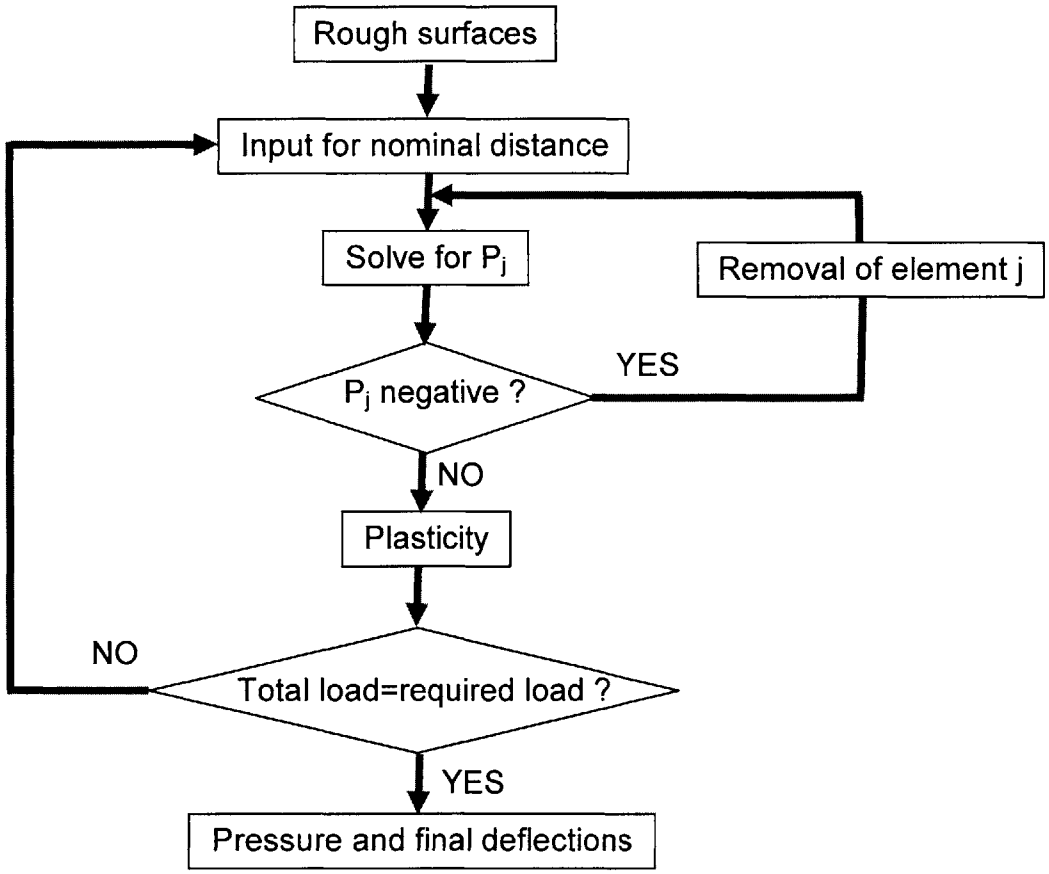

Figure B. The flow chart of the asperity contact model

The flow chart of the asperity contact model is shown in Figure B. Measured rough surfaces are imported with an initial guess of the nominal distance (nd in Figure A), which is the distance between the average surface heights of two bodies. At first, the interpenetration regions are selected as the initial guess of real contact regions. As these selected regions are larger than the real contact regions, the pressures at some elements become negative. If the calculated pressures at certain elements are negative, those elements are removed for the next iteration step. Thus, the selected areas are reduced with more iteration. These iterations are repeated until all contact pressures in the selected regions are positive.

After deformation, some asperities might deform plastically with high contact pressures. Considering plasticity effects, the contact pressures can not be larger than three times of the yield strength. Thus,

$$P_j = 3\sigma_Y \text{ when } P_j \geq 3\sigma_Y \qquad \text{where } \sigma_Y \text{ is the yield strength.}$$

Considering the plasticity effects contradicts with the original numerical scheme of Ju and Zheng which considers elastic deformation only. However, it is known that possible errors due to this contradiction are reasonably small [32].

After that, the total support load is computed from the real contact pressures and compared to the desired load. If the calculated load is not within the specified range, all of the procedures are repeated with adjustments of the nominal distance. After convergence, the model generates the following final outputs: the real contact regions, contact pressures and deflections of the asperities.

To validate the asperity contact model, its results are compared with those of the other asperity contact models. The plot of dimensionless pressure vs. the average gap between two rough surfaces is compared with that from Lee and Cheng's model [19] in Figure C. Two rough surfaces are generated numerically with the following parameters: rms (σ)=0.1μm, the correlation length in x (β_x)= 40σ, the correlation length in y (β_y)=5σ, Pe (β_x/β_y)=8 and Gaussian distribution.

Recall that Lee and Cheng's relation between the contact pressures and the average gap assumes 2D longitudinal rough surfaces (Pe=∞). Some deviations for the low contact pressures might come from the fact that generated rough surfaces are not complete 2D longitudinal surfaces. However, two plots in Figure C show reasonable agreement for wide range of the total loads, especially for high loads.

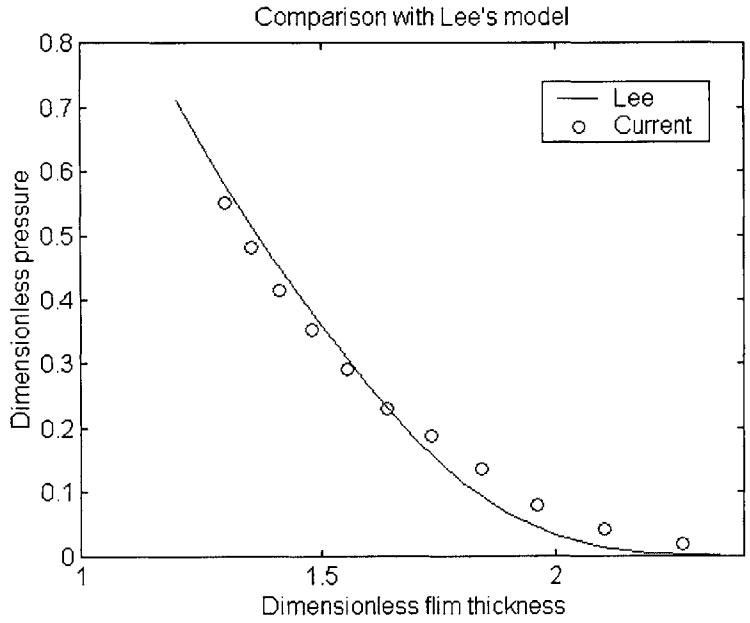

Figure C. Comparisons of the asperity contact model to Lee and Cheng's model

b. Local temperature rise model

With real contact regions, pressures and final gap heights, frictional heat flux can be calculated as follows:

$$q(x,y) = f_b P(x,y) V \qquad \text{in the real contact regions,}$$

$$q(x,y) = \mu \frac{V^2}{H(x,y)} \qquad \text{in the non-contact regions,}$$

where f_b : the boundary friction coefficient,

P(x,y) : the real contact pressure at (x,y),

V : the relative sliding velocity,

H(x,y) : the final gap heights at (x,y),

and μ : the viscosity of the lubricant .

Note that contact pressures and gap heights change during the sliding motion. Thus, the distribution of the frictional heat flux also changes with time.

The temperature increments on the stationary surface (x,y) at any time t due to an instantaneous heat source with the heat flux magnitude of q(x',y',t') and the heat partition to the stationary surface f(x',y',t') at x', y', and t' are calculated from Carslaw and Jaeger [33] as,

$$dT(x,y)=\frac{f(x',y',t')q(x',y',t')\,dx'dy'dt'}{4\rho c[\pi\alpha(t-t')]^{3/2}}\exp\left[-\frac{(x-x')^2+(y-y')^2}{4\alpha(t-t')}\right].$$

Define $\bar{x}=\frac{x}{l_x}$, $\bar{y}=\frac{y}{l_x}$, $\bar{t}=\frac{4\alpha t}{l_x^2}$, $\bar{q}=\frac{q}{P_{ref}V}$, and $\bar{T}=\frac{2\pi^{3/2}kT}{P_{ref}Vl_x}$ where P_{ref} is the reference pressure and V is the sliding velocity. Then, the above equation can be non-dimensionalized as,

$$d\bar{T}(\bar{x},\bar{y})=\frac{f(x',y',t')\bar{q}(\bar{x}',\bar{y}',\bar{t}')\,d\bar{x}'d\bar{y}'d\bar{t}'}{(\bar{t}-\bar{t}')^{3/2}}\exp\left[-\frac{(\bar{x}-\bar{x}')^2+(\bar{y}-\bar{y}')^2}{(\bar{t}-\bar{t}')}\right].$$

Temperature rise on the stationary surface from time 0 to time t due to all the frictional heat sources over the contact area A can be written as,

$$d\bar{T}(\bar{x},\bar{y},\bar{t})=\int_0^{\bar{t}}\iint_A d\bar{T}(\bar{x},\bar{y},\bar{t})\,d\bar{x}'d\bar{y}'d\bar{t}'.$$

When M by N calculating mesh is used for whole contact areas and L is the number of contact time intervals until time t, the above equation can be rewritten as,

$\Delta\bar{T}(i,j,l)=\sum_{k=1}^{L-1}\sum_{n=1}^{N}\sum_{m=1}^{M} f(i,j,l)\,\bar{q}(m,n,k)\,R(i-m,j-n,L-k-1)$ in the discretized form

where

$$R(i-m,j-n,L-k-1)=\int_{\bar{t}_k}^{\bar{t}_{k+1}}\int_{\bar{y}_n}^{\bar{y}_{n+1}}\int_{\bar{x}_m}^{\bar{x}_{m+1}}\frac{1}{(\bar{t}-\bar{t}')^{3/2}}\exp\left\{-\frac{(\bar{x}-\bar{x}')^2+(\bar{y}-\bar{y}')^2}{\bar{t}-\bar{t}'}\right\}d\bar{x}'d\bar{y}'d\bar{t}'$$

and f(i,j,l) is the heat partition to the stationary surface at the element (i,j) and the time l.

For details in calculations of R(i-m,j-n,L-k-1), refer to [15]. Finally, the local temperature rise on the stationary rough surface can be calculated once distributions of the frictional heat flux to the stationary rough surface are known.

To validate the local temperature rise model, the maximum temperature from Tian and Kennedy [13] with a moving square heat source (heat flux magnitude = 5e8*V [W/m^2]) is compared with that from the numerical model in Figure D. For a wide range of the sliding speed, the simulation results show good agreements.

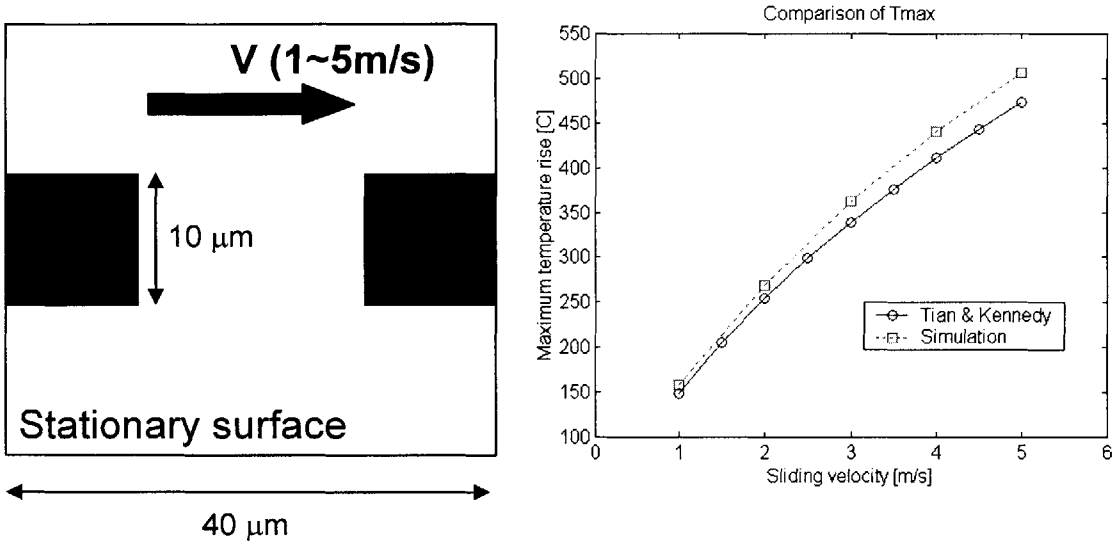

Figure D. Validations with a moving square heat source

After validations, measured rough surfaces are imported to the asperity contact model and the local temperature rise model. The size of the stationary rough surface is 178 μm parallel and 92.8 μm perpendicular to the sliding direction. Two rough surfaces are pressed against each other with the pressure of 14.6 MPa. This value of the contact

pressure lies between the maximum contact pressure under the normalized axial loads of 1.0 and 1.5. The sliding speed is 1.8 m/s. The asperity contact model calculates the unsteady distributions of frictional heat flux during the sliding of two rough surfaces.

To calculate the heat flux distribution into the stationary rough surface, the heat partition function to the stationary surface has to be known. The heat partition function is assumed to be constant and is obtained from the averaged heat partition of the 3D thermal model.

Figure E shows the average local temperature rise (left) and the maximum local temperature rise (right) on the stationary rough surface. Recall that the sliding motion of two rough surfaces is unsteady. If the sliding surface is smooth and the stationary surface is rough, the average local temperature rise would increase initially then reach steady state after sufficient time. When both surfaces are rough, the average local temperature would show similar behavior except that small variations exist even after sufficient time due to changes of contact regions. This behavior of the average local temperature rise is shown in Figure E (left).

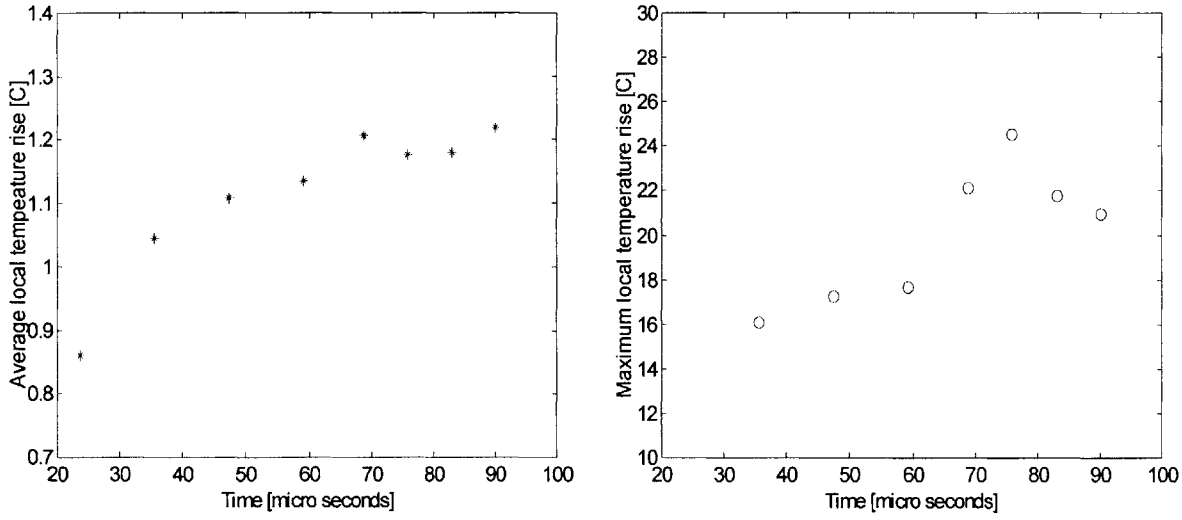

Figure E. The average (left) and maximum (right) local temperature rise on the stationary rough surface during sliding motion

After 60 micro seconds, the average local temperature rise shows small variations of around 1.2 C. Thus, after 60 micro sections, the effects of initial heating have gone away. The magnitudes of the maximum local temperature rise after 60 micro seconds are on the order of 20C. The maximum nominal temperature for the stationary surface from the 3D thermal model is approximately 90-105 C under the normalized axial load 1.0-1.5 and the speed 1.8 m/s. Thus, the maximum nominal temperature rise is comparable or one order of magnitude higher than the maximum local temperature rise. This means nominal temperature distribution can not be neglected for the current metal to metal face seals.

B. Surface generator

The seal surface generator has been developed to provide a complete tool with the numerical models for further investigations and improvements in the seal design. The general seal profile is shown in Figure F. Such a profile with two peaks and one valley (where the first derivatives of the profile are zero) in the flat band region is the most complicated possible found in the measurements.

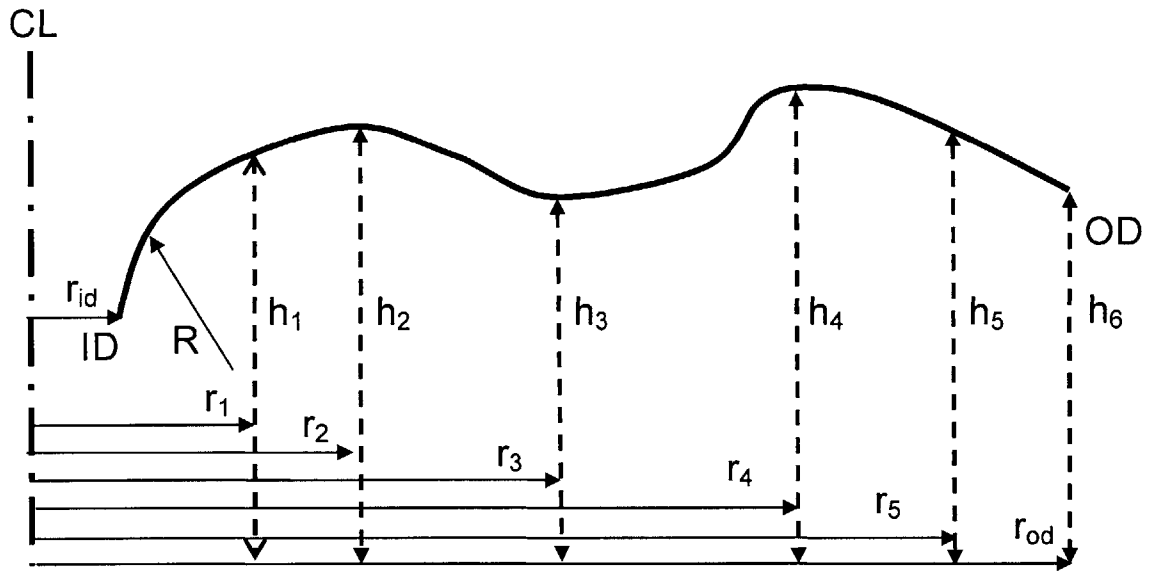

Figure F. Radial surface profiles with parameters of the surface generator

Each parameter show in Figure F is defined as:

r_{id}: the radial position at the inside diameter,

R: the radius of curvature,

r_1, h_1: the radial position and the surface height at the start of the curvature,

r_2, h_2: the radial position and the surface height at the first peak in the flat band,

r_3, h_3: the radial position and the surface height at the valley in the flat band,

r_4, h_4: the radial position and the surface height at the second peak in the flat band,

r_5, h_5: the radial position and the surface height near the outside diameter,

r_{od}, h_6: the radial position and the surface height at the outside diameter.

The continuity of all positions and slopes are ensured for each segment of the radial surface profile. In addition to the radial surface variations, the surface generator can generate the seal surfaces with circumferential variations such as the starts of the curvature, the radius of the curvature, and the amplitude of waviness of the surface heights.

In summary, the current surface generator can fabricate seal surfaces with radial and circumferential variations, which can be used for further investigations and design process. Figure G shows the one of the generated surface profile with the following parameters: two waves of amplitude of 1μm, 50 mm radius of the curvatures, and the circumferential variations in the starts of the curvature (0.2 mm).

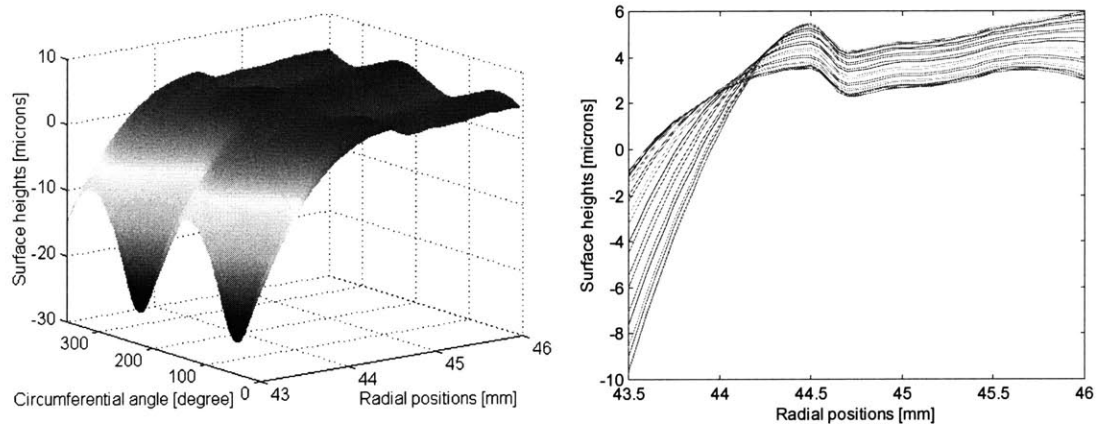

Figure G. One example of the generated surface

Bibliography

[1] Lebeck, A. O. (1991). *Principles and design of mechanical face seals*, New York: John Wiley & Sons, Inc.

[2] Dyson, A. (1975). "Scuffing – a review". *Tribology International*, 8, part I: 77-87, part II: 117-122.

[3] Batchelor, A. W. (1995). "Model of scuffing based on the vulnerability of an elastohydrodynamic oil film to chemical degradation catalyzed by the contacting surfaces". *Tribology Letters*, 1, 349-365.

[4] Bowman, W. F. and Stochowiak, G. W. (1996). "A review of scuffing models", *Tribology Letters*, 2, 113-131.

[5] Stochowiak, G. W. and Batchelor, A. W. (2000). *Engineering tribology*, Boston: Butterworth-Heineman.

[6] Tian, X. and Kennedy, F. E. (1993). "Contact surface temperature models for finite bodies in dry and boundary lubricated sliding", *Journal of tribology*, 115, 411-418.

[7] Knoll, G., Freeken, H. and Hoft, H. W. (1994). "Thermo-hydrodynamic calculation of end face seals", *14th international conference on fluid sealing*, 367-883.

[8] Person, V., Tournerie, B. and Frene, J. (1997). "THD analysis in misaligned and wavy face seals, *17th international conference on fluid sealing"*, 505-518.

[9] Tournerie, B., Danos, J. C. and Frene, J. (2001). "Three-dimensional modeling of THD lubrication in face seals", *Journal of tribology*, 123, 196-204.

[10] Blok, H. (1937). "Theoretical study of temperature rise at surfaces of actual contact under oiliness lubricating conditions", *Proceedings of general discussion on lubrication and lubricants*, Institution of mechanical engineers, 222-235.

[11] Jaeger, J. C. (1942). "Moving sources of heat and the temperature at sliding contacts", *Proceedings of the Royal Society*, N. S. W., 56, 203-224.

[12] Ling, F. F. and Pu, S. L. (1964). "Probable interface temperatures of solids in sliding contact", *Wear*, 7, 23-34.

[13] Tian, X. and Kennedy, F. E. (1994). "Maximum and average flash temperatures in sliding contacts", *Journal of tribology*, 116, 167-174.

[14] Lai, W. T. (1982). "Temperature analysis in lubricated simple sliding rough contacts". PhD thesis, Northwestern university, Department of mechanical engineering.

[15] Liangheng, Q. and Cheng, H. S. (1998). "Temperature rise simulation of three-dimensional rough surfaces in mixed lubricated contact", *Journal of tribology*, 120, 310-318.

[16] Leach, L. F. and Kelly, B. W. (1965). "Temperature, the key to lubricant capacity", *ASLE transactions*, 8(3), 271-285.

[17] Matveevsky, R. M. (1992), "Friction power as a criterion of seizure with sliding lubricated contact", *Wear*, 155(1), 1-5.

[18] Sussman, T. and Bathe, K. J. (1986). "Studies of finite element procedures-stress band plots and the evaluation of finite element meshes", *Eng. Comput.*, 3, 178-191.

[19] Lee, S. C. and Cheng, H. S. (1992). "On the relation of load to average gap in the contact between surfaces with longitudinal roughness", Tribology transactions, 35(3), 523-529.

[20] Dowson, D. and Taylor, C. M. (1979). "Cavitation in bearings", *Ann. Rev. Fluid Mech.*, 11, 35-66.

[21] Payvar, P. and Salant, R. F. (1992), "A computational method for cavitation in a wavy mechanical seal", *Journal of tribology*, 114, 199-204.

[22] Floberg, L. (1964). " Cavitation in lubricating oil films", *Cavtation in real liquids*, Amsterdam: Elsevier, 138-146.

[23] Johnson, K. L. (1985). Contact mechanics, New York: Cambridge university press.

[24] Etsion, I. and Pascovici, M. D. (1993). "A thermohydrodynamic analysis of a misaligned mechanical face seal", *Tribology transactions*, 36(4), 589-596.

[25] Ozisik, M. N. (1968). *Boundary value problems of heat conduction*, Scranton: International textbook company.

[26] Becker, K. M. (1963). "Measurement of convective heat transfer from a horizontal cylinder rotating in a tank of water", *International journal of heat and mass transfer*, 6, 1053-1062.

[27] Aoki, H., Nohira, H. and Aria, H.(1967). "Convective heat transfer in an annulus with an inner rotating cylinder", *Bulletin of JSME*, 10(39), 523-352.

[28] Taylor, R. I. (1998). "The inclusion of lubricant shear thinning in journal bearing models", *Proceedings of the 25th Leeds-Lyons Symposium on Tribology.*

[29] Greenwood, J. A. and Williamson, J. B. P. (1966). "Contact of nominally flat surfaces", *Proceedings of the Royal Society of London, Series A*, 295(1442), 300-139.

[30] Onions, R. A. and Archard, J. F. (1973). "The contact of surfaces having a random structure", *Journal of phaysics D: Applied physics*, 6, 289-304.

[31] Yongqing, J. and Linqing, Z. (1992). "A full numerical solution for the elastic contact of three-dimensional real rough surfaces", *Wear*, 157, 151-161.

[32] Varadi, K. Neder, Z. and Friedrich, K. (1996). "Evaluation of the real contact areas, pressure distributions and contact temperatures during sliding contact between real metal surfaces", *Wear*, 200, 55-62.

[33] Carslaw, H. S. and Jaeger, J. C. (1959). *Conduction of heat in solids*, 2nd ed., Oxford: Clarendon press.